# SPATIOTEMPORAL CONTROL OF ACTION POTENTIAL DURATION ALTERNANS IN VENTRICULAR TISSUE

A Dissertation

Presented to the Faculty of the Graduate School

of Cornell University

In Partial Fulfillment of the Requirements for the Degree of

Doctor of Philosophy

by

Uche Brian Kanu

August 2011

# SPATIOTEMPORAL CONTROL OF ACTION POTENTIAL DURATION ALTERNANS IN VENTRICULAR TISSUE

Uche Brian Kanu, Ph.D.

Cornell University 2011

Cardiac electrical alternans, sometimes referred to as action potential duration (APD) alternans, is a beat-to-beat alternation in action potential waveform, which naturally occurs at sufficiently fast pacing rates. Its presence has been putatively linked to the onset of cardiac reentry, which is a precursor to ventricular fibrillation (VF). Because of the established link between APD alternans and the onset of VF, it may be beneficial to develop means to terminate and/or prevent alternans in cardiac tissue. Closed-loop feedback mechanisms aimed at controlling a dynamically stable period-2 rhythm (alternans) to an unstable period-1 rhythm (no alternans) using single-site intervention from an external source may be one such option. Previous studies that have utilized this alternans control approach have shown that closed-loop alternans control techniques that apply a succession of externally-administered cycle perturbations at a single site provide limited spatially-extended alternans elimination in sufficiently large cardiac substrates. However, detailed investigations into the spatial dynamics of alternans control have been largely restricted to Purkinje fiber studies. A complete understanding of alternans control in the more clinically relevant ventricular tissue is needed if more advanced electrode-based intervention techniques are to be developed for cardiac alternans therapy.

In this work, both mathematical modeling of simulated cardiac tissue and fluorescence imaging of right ventricular cardiac preparations were used to better

understand the characteristics of alternans and alternans control in ventricular tissue.

In the first part of this work, alternans and alternans control was simulated in one-dimensional cables using the Shiferaw-Sato-Karma (SSK) computational model. The model parameters were varied in order to simulate alternans and alternans control under several different mechanistic manifestations of alternans. Furthermore, the spatial extent of alternans control was systematically probed under varying cable lengths and basic cycle lengths (BCLs) in an attempt to quantify spatial alternans dynamics.

In the second part of the study, alternans and alternans control experiments were performed using a custom-designed optical mapping system capable of high-resolution imaging. In this way, the spatial efficacy of alternans control was quantified in an experimental setting, and furthermore, the observation and analysis of APD and repolarization dynamics were made possible.

In the third part of the study, the effects of noise on alternans control were investigated using SSK implemented simulations of single cell and 1-D arrangements of ventricular tissue. The results of this study will aid in future alternans control experiments, which can occur in the presence of varying amounts of noise.

This work represents the first attempts to directly investigate alternans and alternans control in ventricular tissue. Clinical realization of advanced electrode-based therapies for alternans and other related cardiac electrical abnormalities will benefit from the insights gained from this and future related studies.

# BIOGRAPHICAL SKETCH

Uche Kanu graduated from Columbia University in 2005 with a bachelor of science degree in biomedical engineering. He received a master of science degree in biomedical engineering from Cornell University in 2008. He enrolled in the department of biomedical engineering MS/PhD program at Cornell University in 2005.

# ACKNOWLEDGMENTS

I would first and foremost like to acknowledge and thank my advisor, David Christini, whose constant support and guidance this degree owes itself to. At every stage of the way, he acted as a reassuring presence and his counsel provided me with unfailing encouragement and wisdom. His kind mentorship, relating to academic and non-academic affairs both, will never be forgotten.

I would also like to thank all of the past and present members of the Cardiac Electrodynamics Laboratory – Shahriar, Pete, Trine, Yunfan, Anat, Rebecca, Steve, Byron, Jonathan B., Jonathan M., Francis, Armen, Corina, and Willemijn – for their meaningful and impactful contributions to my research and learning experience.

I would also like to thank the other members of my dissertation committee – Robert Gilmour and Jonathan Victor – for their immeasurable advice and assistance during my graduate school tenure.

I am also indebted to various members of the Gilmour Laboratory in Ithaca – Flavio, Mike, and Fred – for their wonderful technical assistance and generous hospitality during my many visits to the Veterinary Tower.

Finally, I would like to acknowledge the love and support of my family, without which none of this would have been possible. To my father and mother: your unwavering support is the simple and sole reason I have achieved all that I have.

TABLE OF CONTENTS

LIST OF FIGURES

LIST OF TABLES

LIST OF ABBREVIATIONS

| | |
|---|---|
| **AP** | Action potential |
| **APD** | Action potential duration |
| **AV** | Atrioventricular |
| **BCL** | Basic cycle length |
| **BPM** | Beats per minute |
| **$Ca^{2+}$** | Calcium |
| **CICR** | Calcium induced calcium release |
| **$Cl^-$** | Chloride |
| **CV** | Conduction velocity |
| **DI** | Diastolic interval |
| **ECG** | Electrocardiogram |
| **ICD** | Implantable cardioverter defibrillator |
| **JSR** | Junctional sarcoplasmic reticulum |
| **$K^+$** | Potassium |
| **LTCC** | L-type calcium channel |
| **$Na^+$** | Sodium |
| **NCX** | Sodium-calcium exchanger |
| **RTXI** | Real-Time eXperimental Interface |
| **RyR** | Ryanodine receptor |
| **SA** | Sinoatrial |
| **SCD** | Sudden cardiac death |
| **SERCA** | Sarcoplasmic reticulum calcium ATPase |
| **SR** | Sarcoplasmic reticulum |
| **SSK** | Shiferaw-Sato-Karma |
| **VF** | Ventricular fibrillation |
| **$V_m$** | Membrane voltage |
| **VT** | Ventricular tachycardia |

LIST OF SYMBOLS

| | |
|---|---|
| $\mathbf{A_D}$ | Phase-specific alternans magnitude |
| $\mathbf{A_M}$ | Alternans magnitude |
| $\mathbf{A_{M,S}}$ | Spatially averaged alternans magnitude |
| $\mathbf{APD_n}$ | APD of beat n |
| $\mathbf{APD_{n+1}}$ | APD of beat n+1 |
| **g** | Alternans control gain |
| **n** | Beat number |
| **T** | Pacing cycle length |
| **T*** | Target pacing cycle length |
| **u** | Slope of the dependence of SR $Ca^{2+}$ release on SR $Ca^{2+}$ load |
| $\gamma$ | $Ca^{2+}$-induced inactivation of L-type $Ca^{2+}$ channel factor |
| $\lambda$ | Alternans control feedback value |
| $\sigma^2$ | Repolarization/APD Dispersion |
| $\tau_f$ | Recovery of inactivation time constant of L-type $Ca^{2+}$ channels |

CHAPTER 1

# BACKGROUND

## 1.1 Introduction

Sudden cardiac death (SCD) is responsible for 50% of all cardiovascular related deaths and ≈300,000 deaths per year in the United States alone [1]. The vast majority of all SCD related deaths are caused by episodes of cardiac electrical disturbances most commonly attributed to ventricular tachycardia (VT) and ventricular fibrillation (VF) [1]. As such, concerted efforts have been made over the years to develop therapies that can prevent and/or terminate episodes of VT/VF and to develop prediction criteria capable of identifying patients at high risk for SCD. These attempts have led to widely used technologies such as the implantable cardioverter defibrillator (ICD) [2, 3] and a host of risk assessment methodologies.

One such SCD predictor, *T-wave alternans*, has attracted particular attention in recent years due to the close association between microvolt T-wave alternans and instances of VF/SCD in clinical [4-8] and experimental studies [9-11]. T-wave alternans is defined as a beat-to-beat change in electrocardiogram (ECG) wave morphology (Fig. 1.1) and is typically induced at elevated pacing cycle frequencies [12]. T-wave alternans is a manifestation of underlying action potential duration (APD) alternans, which refers to beat-to-beat alternations in action potential morphology expressed at the cellular level (Fig. 1.1) [13]. APD alternans has been mechanistically linked to the pathogenesis of reentrant electrical wave activity [13-15], and thus, attempts to develop means to prevent and/or control cardiac alternans have garnered considerable attention within the scientific community.

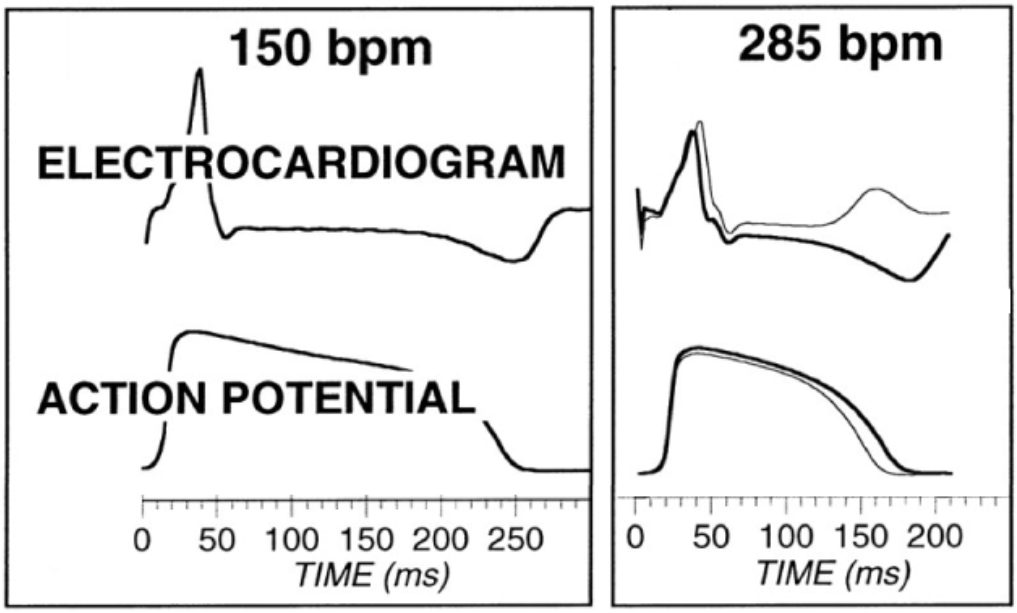


**Figure 1.1 ECG T-wave and transmembrane APD alternans.** ECG lead (top) and representative action potential (bottom) recorded simultaneously from mapping site of Langendorff-perfused guinea pig heart during fixed-rate pacing at 150 and 285 beats per minute (bpm). Tracings recorded from two consecutive beats are superimposed to illustrate electrical alternans. At a pacing rate of 150 bpm, no alternans was observed. At a pacing rate of 285 bpm, alternans in both T-wave and action potential morphology were observed.

*Reproduced from *J. Pastore, S. Girouard, K. Laurita et al., "Mechanism linking T-wave alternans to the genesis of cardiac fibrillation," Circulation, vol. 99, no. 10, pp. 1385, 1999.*

The field of nonlinear dynamics provides a useful framework in which to better understand alternans behavior. Well-established techniques originally developed for the study of chaos and period-doubling bifurcations have been exploited to both probe alternans dynamics and to provide potential mechanisms of alternans elimination. Out of these efforts have emerged closed-loop feedback algorithms capable of controlling a dynamically stable period-2 rhythm (alternans) to an unstable period-1 rhythm (no alternans) using externally applied perturbations to easily accessible system parameters.

The advent of a dynamical systems theory approach to studying cardiac electrical disturbances has attracted interest from clinicians and research scientists alike. Numerous clinical studies, experimental tests, theoretical analyses, and computational modeling efforts have been produced, all attempting to better elucidate the characteristics and behavior of cardiac tissue function within the context of nonlinear dynamics [16].

Specific to alternans and alternans control, significant progress has been made in understanding the associated dynamics in the context of single mycocytes. However, a comprehensive understanding of alternans and alternans control dynamics in spatially-extended systems (i.e., cardiac tissue) is still needed if genuine clinical solutions to alternans are to be developed.

The work discussed in this dissertation describes the first comprehensive attempts at understanding alternans control in ventricular tissue. The rest of the document is structured as follows: The remainder of the background section introduces the architecture of the cardiac electrical system and contains relevant

information about the mechanisms and dynamics of alternans (both in the context of single-cells and tissue) and the single-site alternans control framework. In Chapter 2, computational simulations of ventricular tissue are used to probe the characteristics of alternans and single-site alternans control under a range of alternans behavior types. In Chapter 3, optical mapping experiments are used to elucidate the dynamics of alternans and alternans control in canine cardiac ventricular preparations. In Chapter 4, the effects of noise on alternans control are studied using single-cell and 1-D simulations of ventricular tissue.

## 1.2 Cardiac Electrophysiology

### *1.2.1 Whole organ electrical conduction*

The main function of the heart is to pump blood throughout the rest of the body via repeated and rhythmic contractions. This functionality results from well-timed mechanical forces that are generated at the sub-cellular space-scale, which in turn are the direct result of immediately preceding transmembrane electrical activity. Rapid electrical propagation throughout cardiac tissue gives rise to whole-heart contraction, and as such, electrical wave conduction is carefully regulated to ensure proper cardiac function.

The general nature of cardiac electrical propagation is illustrated in Fig. 1.2. Electrical activity spontaneously initiates in a region of the heart known as the sinoatrial (SA) node. The electrical wave propagates first throughout the right and left atria, giving rise to the mechanical forces that direct blood from both atria into their respective ventricular chambers. Immediately following, activation of the

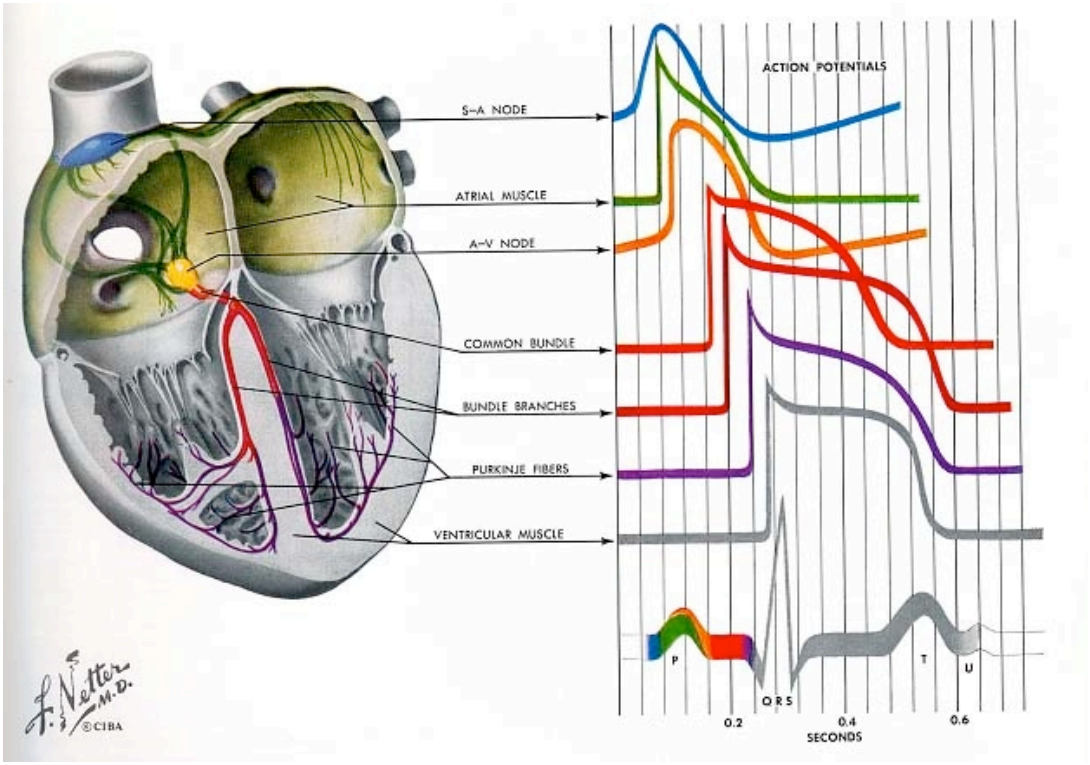


**Figure 1.2 The cardiac conduction system.** Electrical activity generated at the SA node propagates in a carefully controlled manner throughout the heart. The general nature of conduction is illustrated by displaying electrical behavior as a function of space (color coded) and time (see x-axis on right-hand side).

*Reproduced from *Hansen, T. John, Koeppen, M. Bruce, Netter's Atlas of Human Physiology. 2002, pp 70.*

atrioventricular (AV) node – the primary electrical conduit between the atria and the ventricles – occurs, and after a brief delay (allowing for complete atria and ventricle emptying and filling, respectively), the electrical pulse is transmitted throughout the ventricles via the His bundles and Purkinje fiber network. The characteristics of the ECG, an electrical recording derived from strategically placed leads on the outside of the body, reflect the location-specific and temporal nature of whole-heart wave propagation (Fig. 1.2).

### *1.2.2 The action potential*

Whole-heart electrical activity is the spatially-extended manifestation of individual electrically-coupled myocytes undergoing time-dependent processes of transmembrane voltage activity. In normally functioning cardiac cells, this transmembrane voltage activity is known as the action potential (AP). The action potential (Fig. 1.3) is characterized by an increase and subsequent decrease in transmembrane potential in response to a brief stimulus current. (The wave "front" is merely the progression of action potential initiation as a function of space.) The action potential characteristics of a particular myocyte (e.g., shape and duration) are determined by sarcolemmal ion channel behavior and intracellular ion handling kinetics specific to each cell.

Before action potential initiation, the transmembrane voltage of a typical cardiac myocyte is at a hyperpolarized baseline value, the exact value of which is determined by the relative concentrations of charged ions (predominantly $Na^+$, $Ca^{2+}$, $K^+$, and $Cl^-$) inside and outside of the cell. The first phase of the action potential (phase 0) occurs as a result of the rapid influx of $Na^+$ ($I_{Na}$) through $Na^+$ specific channels. These channels are opened from their baseline closed states in response to

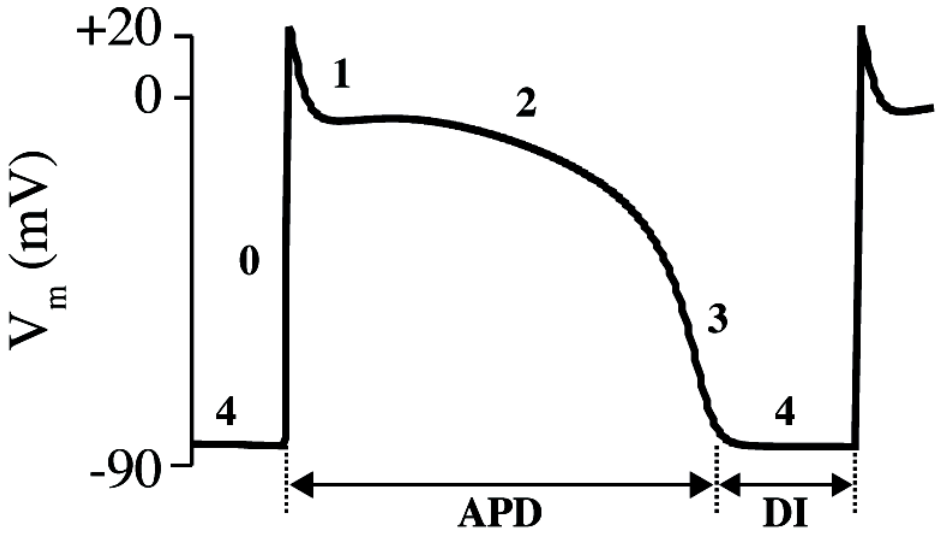


**Figure 1.3 Action potential schematic.** The action potential is comprised of 4 distinct phases of transmembrane voltage activity. During phase 0, in response to a stimulus current, the transmembrane potential of a myocyte rapidly depolarizes primarily due to increased $I_{Na}$ activity. Immediately following the depolarization phase is a slight decrease in transmembrane potential (phase 1; primarily due to $I_{Na}$ inactivation and $I_{to}$ initiation). This is followed by a plateau phase during which the potential remains fairly constant due to the balance between $I_{Ca}$ and $I_{Kr}/I_{Ks}$ (phase 2). During the repolarization phase (3) the transmembrane potential returns to baseline (primarily due to increased outward potassium current) at which value it will remain until initiation of the next AP (phase 4). The APD spans phase 0 to phase 3; the DI consists of phase 4.

the initial increase in voltage typically caused by passively conducted current from recently activated cells (providing the effective stimulus current).

Phase 1 of the action potential follows soon after, during which the $Na^+$ channels quickly inactivate, and transient outward $K^+$ channels begin to open. The decrease in $I_{Na}$ and the increase in potassium current ($I_{to}$) are responsible for the abrupt halt in depolarization and the gradual repolarization observed during phase 1.

The "plateau" phase of the action potential (phase 2) results from the delicate balance between inward $Ca^{2+}$ current ($I_{Ca}$), via L-type calcium channels, and outward $K^+$ currents [comprised of the rapid and slow components ($I_{Ks}$, $I_{Kr}$) of the delayed rectifier $K^+$ current]. The rapid repolarization of phase 3 is due primarily to the closing of the L-type calcium channels amidst continued $I_{Ks}$ activity. This initiates a cascade of events that leads to an increased repolarizing current (via $I_{Kr}$, $I_{Ks}$, and $I_{K1}$), and the eventual progression of the transmembrane voltage back to the baseline level. The action potential duration (APD) is determined by the length of time elapsed from the beginning of phase 0 to the end of phase 3 (Fig. 1.3).

The "rest" period between action potentials, during which the transmembrane potential remains at the baseline value (phase 4), is referred to as the diastolic interval (DI). The DI interval is important because it allows the many channel kinetics of the cell to fully recover. Below the full recovery time threshold, there is a range of DI values that will result in proportionally shorter APD values (specifics in *Section 1.3.2*). DI values below this range do not provide the cell with enough rest, however, and the cell will be unable to generate an action potential at all. The time during which a cell

is unable to generate an action potential due to insufficient channel recovery is referred to as the *refractory period*.

## 1.3 Cellular Alternans Dynamics

### *1.3.1 Stability diagram analysis*

At sufficiently long stimulation periods, the processes underlying an action potential occur in an identical manner on a beat-to-beat basis – the aggregate channel kinetics that determine the behavior of the aforementioned currents responsible for the morphology of the action potential follow the same time course for every beat. The resulting sequence of action potentials will exhibit a pattern of unchanging APD values. This behavior, referred to as a *period-1 rhythm* (Fig. 1.4), is classified as stable, meaning that small disturbances (owing to noise or any externally applied electrical activity) dissipate, allowing for a return to the period-1 rhythm pattern of action potentials. Furthermore, due to incomplete recovery, a monotonic decrease in APD is observed as a function of decreasing stimulation period within a certain range of stimulation periods.

Due to cellular properties inherent to all cardiac myocytes, there exists a stimulation period below which a fundamental change in the beat-to-beat AP morphology (and thus APD behavior) occurs. At this so called *bifurcation point* a reduction in the stimulation period causes the resulting sequence of APD values to alternate in a long-short-long-short pattern. Furthermore, this *period-2 rhythm*, also referred to as alternans, is stable, whereas the period-1 rhythm, while still dynamically viable, has been transformed into an unstable rhythm, sensitive to any and all

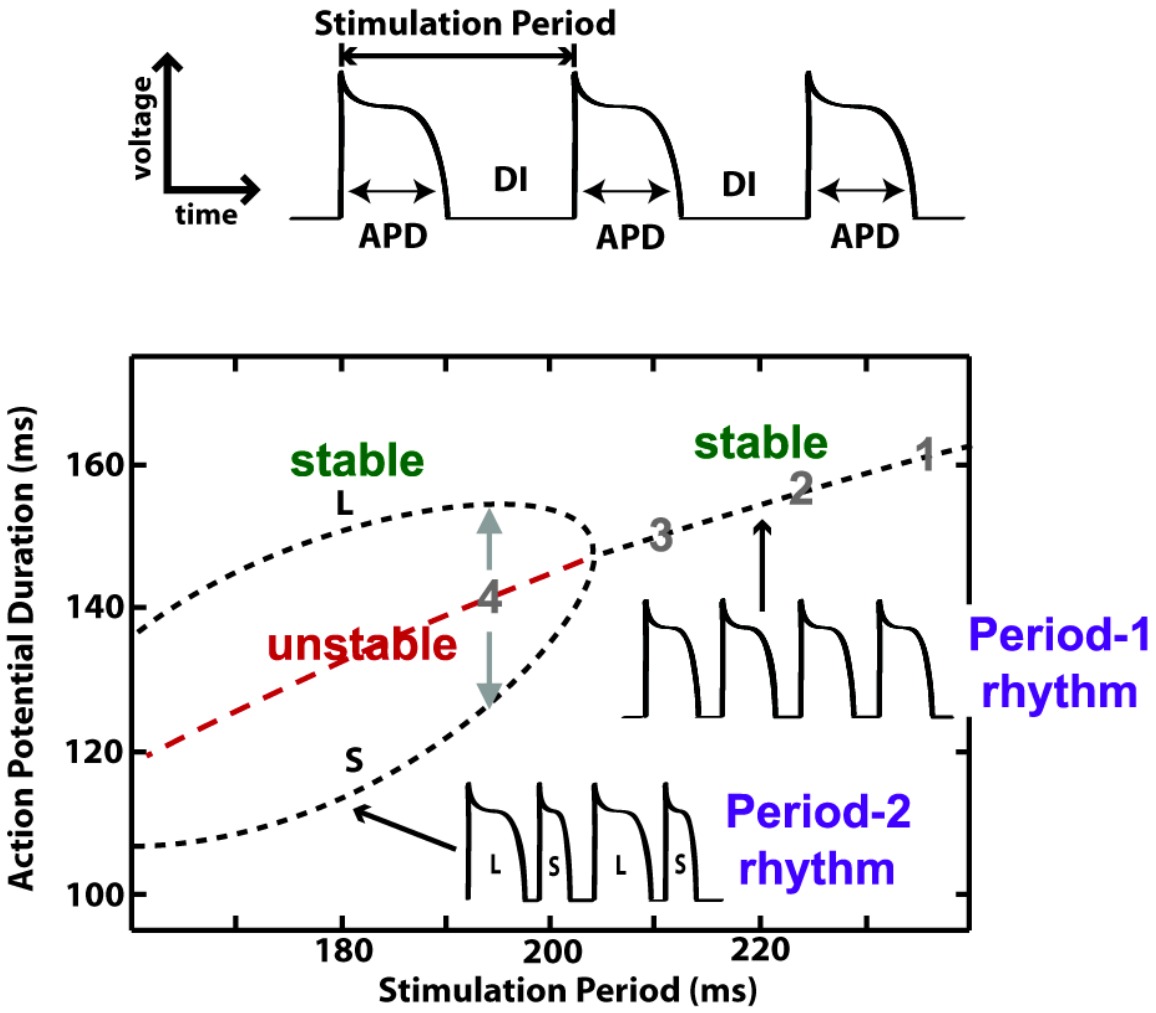


**Figure 1.4 APD stability diagram**. At sufficiently long stimulation periods action potentials elicited exhibit a dynamically stable pattern in which the corresponding APD values will all be the same from beat-to-beat (period-1 rhythm). Progressively shortened stimulation periods result in a monotonic decrease in APD until a bifurcation occurs after which the stable period-1 rhythm is replaced by a stable period-2 rhythm of alternating APD values (alternans).

*Reproduced from *Jordan, P.N., and D.J. Christini. 2005. "Therapies for ventricular cardiac arrhythmias," Critical Reviews in Biomedical Engingeering 33:557-604.*

perturbations. [It is the goal of alternans control (discussed in *Section 1.6*) to force the system from the stable period-2 rhythm (alternans) to the unstable period-1 rhythm (no alternans).]

### *1.3.2 Action potential duration restitution*

The dynamical relationship between stimulation period, APD, and alternans can also be understood, perhaps more comprehensively, using the APD restitution relationship [17] (Fig. 1.5). Derived from experimental protocols, the APD restitution relationship reflects the dependence between the APD of an action potential ($APD_n$) and the preceding diastolic interval ($DI_{n-1}$) [$APD_n = f(DI_{n-1})$]. As mentioned before, the diastolic interval provides the sarcolemmal channel kinetics responsible for the action potential with time to recover towards their baseline states. An arbitrarily long DI will allow for complete recovery (i.e., there exists a maximum APD value), however, at shorter DI values, which allow for only incomplete recovery, a reduction in DI will result in a shorter action potential.

(The shape of the APD restitution curve is dictated primarily by the kinetics of the L-type $Ca^{2+}$ channel. As mentioned in *Section 1.2.2*, the calcium current, $I_{Ca}$, plays a key role in the regulation of APD. At sufficiently short DI values, recovery from inactivation of the L-type $Ca^{2+}$ channels will be incomplete, which decreases subsequent $I_{Ca}$, which results in a shorter APD.)

Graphical representation of the stimulation period, a.k.a. basic cycle length (BCL), is possible by plotting a straight line with slope -1 where the x- and y-axis intercepts = BCL (i.e., $BCL = APD_n + DI_n$). The intersection of the constant-BCL line and the restitution curve represents the fixed point of the dynamical system. Constant

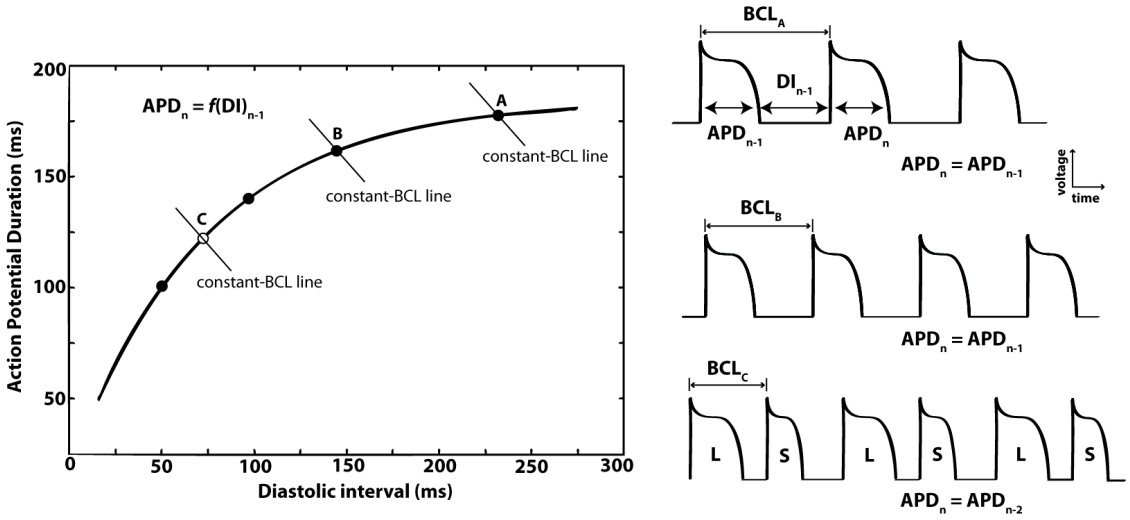


**Figure 1.5 APD restitution relationship**. An example APD restitution curve and the corresponding action potential traces reflecting the relationship between $APD_n$ and $DI_{n-1}$, via the restitution function *f*, at various stimulation periods. The intersection of the constant-BCL line (slope -1, with x- and y- axis intercepts equal to the BCL) and the restitution curve indicates the "fixed point" of the system for that particular BCL. The stability of the fixed point is denoted by the circle type (filled – stable; open – unstable).

pacing at a sufficiently long BCL will result in APD and DI values which represent a stable period-1 rhythm (point A). Decreasing the stimulation period ($BCL_A \rightarrow BCL_B$) simply shifts the constant-BCL line and moves the fixed point to the new intersection (point A → point B).

Further reduction of the stimulation period ($BCL_B \rightarrow BCL_C$) elicits the stable period-2 behavior of alternans. At this point the constant-BCL/restitution intersection, though still a fixed point of the dynamical system, becomes unstable (point C, open circle) and the two points on either side of the unstable fixed point represent the values of APD and DI between which the period-2 rhythm alternates.

### *1.3.3 Iterative map analysis*

Within the APD restitution dynamical framework, the slope of the restitution curve at the constant-BCL/restitution intersection determines the stability of the fixed point. Slope <1 results in a stable fixed point, whereas slope >1 results in an unstable fixed point (Fig. 1.6).

This stability (instability) behavior can be graphically demonstrated using an iterative map ("cobweb" diagram) approach. Shown in Fig. 1.7 is one such diagram illustrating the period-2 nature of alternans behavior. In this particular example, the fixed point is unstable (slope >1). Beginning at the intersection, a small negative perturbation in DI yields the initial point of the cobweb diagram (denoted by the star). The subsequent APD value is determined using the restitution relationship by drawing a straight line down to the new intersection point (labeled "a"). The subsequent DI is determined by moving horizontally to the constant-BCL line (to the point labeled "b"). This process is repeated until a steady-state is reached at which a stable period 2-

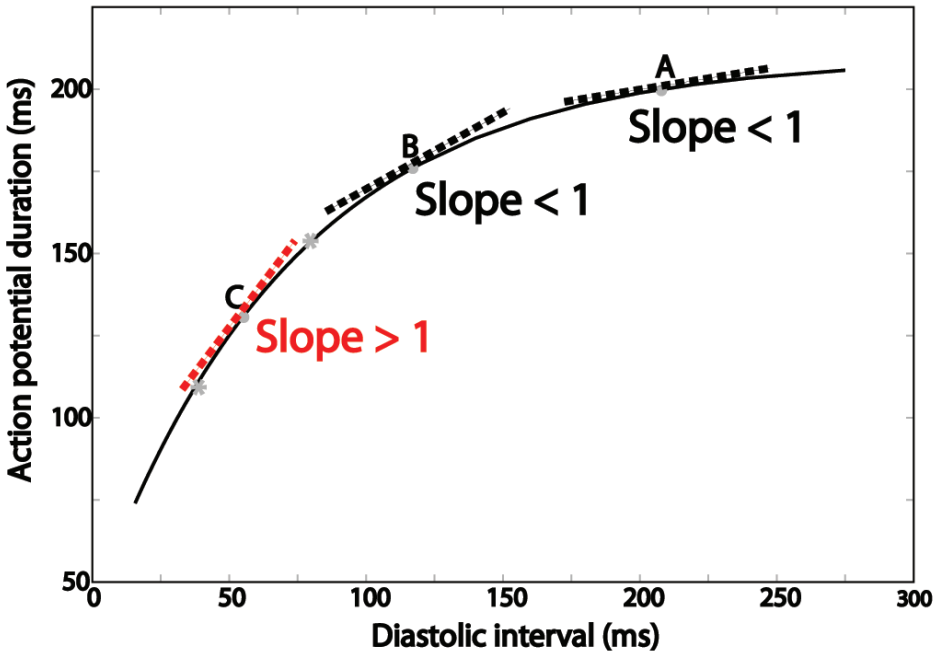


**Figure 1.6 APD restitution slope**. The slope of the constant-BCL/restitution intersection determines the stability of the fixed point. Slope <1 – stable; slope >1 – unstable.

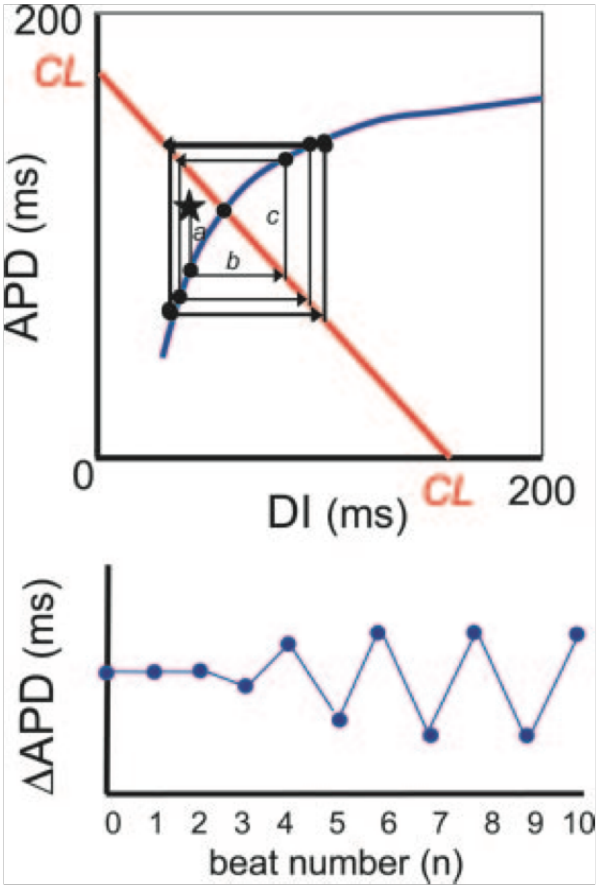


**Figure 1.7 APD cobweb diagram**. Top plot: cobweb diagram illustrating APD alternans. The restitution curve and the constant-BCL line are denoted by the blue and red lines, respectively. The arrowed lines depict the progression of successive APD and DI values in response to an initial perturbation in DI (denoted by the star) away from the unstable fixed point. Bottom plot: resulting ΔAPD values as a function of beat number following the initial perturbation in DI.

*Reproduced from *J. Weiss, A. Karma, Y. Shiferaw et al., "From pulsus to pulseless: the saga of cardiac alternans," Circulation Research, vol. 98, no. 10, pp. 1244, 2006.*

rhythm emerges. Using this graphical approach it can be shown that if the slope of the constant-BCL/restitution intersection is >1, small perturbations will grow over time and the system will tend towards the period-2 rhythm, whereas if the slope at the intersection is <1, small perturbations will dissipate over time and the system will tend towards a period-1 rhythm.

## 1.4 Cellular Alternans Mechanisms

### *1.4.1 Voltage-driven alternans*

The previously described mechanism of alternans (*Section 1.3*), which depends solely on the nature of the APD restitution curve, is known as "voltage-driven" alternans. Within this framework, for alternans to occur, the restitution curve must include a region of slope >1. Consequently, changes to the steepness of the APD restitution curve will affect the propensity of a given cardiac myocyte to bifurcate into alternans at fast pacing rates. One way to vary the steepness of the curve is by changing the kinetics of the calcium current ($I_{Ca}$), which, as explained in *Section 1.2.2*, is largely responsible for the duration of the plateau phase of the action potential. The L-type $Ca^{2+}$ current can be modeled mathematically as follows:

$$I_{Ca} = \bar{I}_{Ca} f d f_{Ca} \quad \textbf{(1)}$$

where $\bar{I}_{Ca}$ determines the maximum amount of current possible, and $f$, $d$, and $f_{Ca}$ describe the kinetics of the inactivation and activation gating processes. Changes to the time constant ($\tau_f$) of the inactivating $f$ gate (Eq. 2) have a direct effect on the steepness of the restitution curve. A large $\tau_f$ tends to increase the slope, whereas a small $\tau_f$ has the opposite effect.

$$\frac{df}{dt} = \frac{f^{\infty} - f}{\tau_f}\tau_f = 30 + \frac{200}{1 + e^{(V+20)/9.5}} \quad \textbf{(2)}$$

*Kinetics of the $Ca^{2+}$ current *f* gate according to the SSK model [18].

### *1.4.2 Calcium handling system*

The APD restitution-derived mechanism of alternans is likely too simplistic because it neglects the effects of calcium dynamics. Recently published experiments have demonstrated that alternans behavior can occur at BCL values at which the measured APD restitution slope was much less than one [19]. Furthermore, recent voltage clamp experiments have suggested that alternans of the intracellular calcium concentration ($[Ca]_i$) can give rise to secondary alternans of the APD [20]. Whatever the case, the role of the intracellular calcium handling system has emerged as an important player in alternans initiation and maintenance and therefore must be taken into account.

Fig. 1.8 highlights the important aspects of the calcium handling system. The inward calcium current through L-type calcium channels (LTCC) triggers additional calcium release from the sarcoplasmic reticulum (SR) via ryanodine receptor (RyR) interactions, in a process known as calcium-induced-calcium-release (CICR). Subsequent calcium removal from the intracellular space occurs by either a) $Ca^{2+}$ re-uptake into the SR via the SERCA pump, or b) extrusion out of the cell via the sodium-calcium exchanger (NCX). In this way, each action potential is accompanied by an increase and subsequent decrease in $[Ca]_i$.

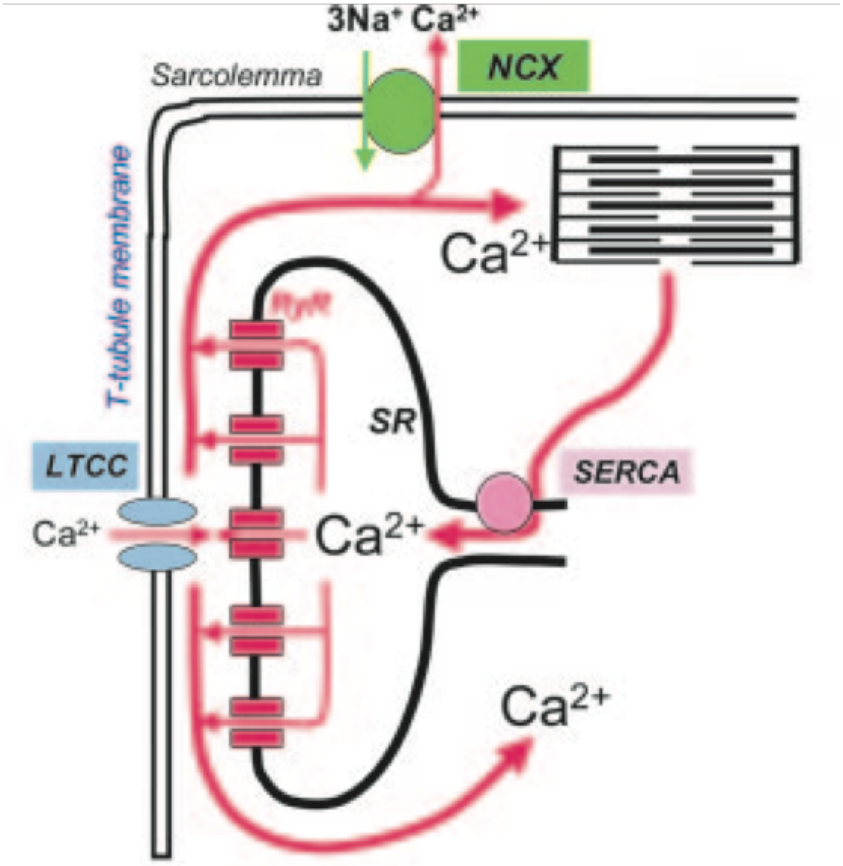


**Figure 1.8 Calcium cycling dynamics schematic.** Inward $Ca^{2+}$ ($I_{Ca}$) via L-type calcium channels (LTCC) triggers the release of additional $Ca^{2+}$ into the cell from the sarcoplasmic reticulum (SR) via ryanodine receptor (RyR) interactions. Subsequent SERCA pump and Na-Ca exchanger (NCX) function is responsible for removing $Ca^{2+}$ before the cycle repeats.

*Reproduced from *J. Weiss, A. Karma, Y. Shiferaw et al., "From pulsus to pulseless: the saga of cardiac alternans," Circulation Research, vol. 98, no. 10, pp. 1244, 2006.*

### *1.4.3 Calcium-driven alternans*

The calcium cycling system is prone to alternans behavior in much the same way that the voltage dynamics are. The morphology of the intracellular calcium concentration, (i.e., the calcium transient), is capable of period-2 rhythm behavior at fast cycling frequencies. This instability in calcium dynamics has been attributed to several factors. The prevailing theory, supported by experimental [21] and theoretical [22] studies, suggests that the steep dependence of SR $Ca^{2+}$ release on SR $Ca^{2+}$ load at high $Ca^{2+}$ concentration levels is the primary cause (Fig. 1.9). The dynamics of $Ca^{2+}$ re-uptake into the SR (via SERCA) and to a lesser extent $Ca^{2+}$ leakage from the SR likely play an important role as well [22].

Fig. 1.10 illustrates the relationship between SR release and SR load using the cobweb diagram approach [23]. If $\Delta r_n$ and $\Delta l_n$ denote the difference in SR load and the corresponding difference in SR release, respectively, of beat $n$ relative to beat $n-1$, the equation $\Delta r_n = m\Delta l_n$, relates the two by the factor $m$ – the slope of the release/load relationship. For the next beat $(n+1)$, the amount of SR load will depend on the amount of $Ca^{2+}$, which was not released, plus the amount of $Ca^{2+}$ pumped back by the SERCA pump. Setting $u$ as the "requestration" factor, which determines the amount of $Ca^{2+}$ re-uptake, and continuing with simple algebraic manipulation will lead to the following equation: $\Delta r_n = -m/(m-1)(1-u)\Delta l_{n+1}$. The two equations given above can be used to generate the iterative maps and cobweb diagram analysis of Fig. 1.10. In this analytical framework the parameters $u$ and $m$ determine whether the $Ca^{2+}$ handling system will tend towards alternans or a stable period-1 rhythm. For example, a large value of $m$, indicating a steeper load/release relationship, and a small value of $u$, indicating lessened SR re-uptake, will promote alternans behavior. It is important to note that these maps are only valid for $Ca^{2+}$ values very close to the equilibrium point.

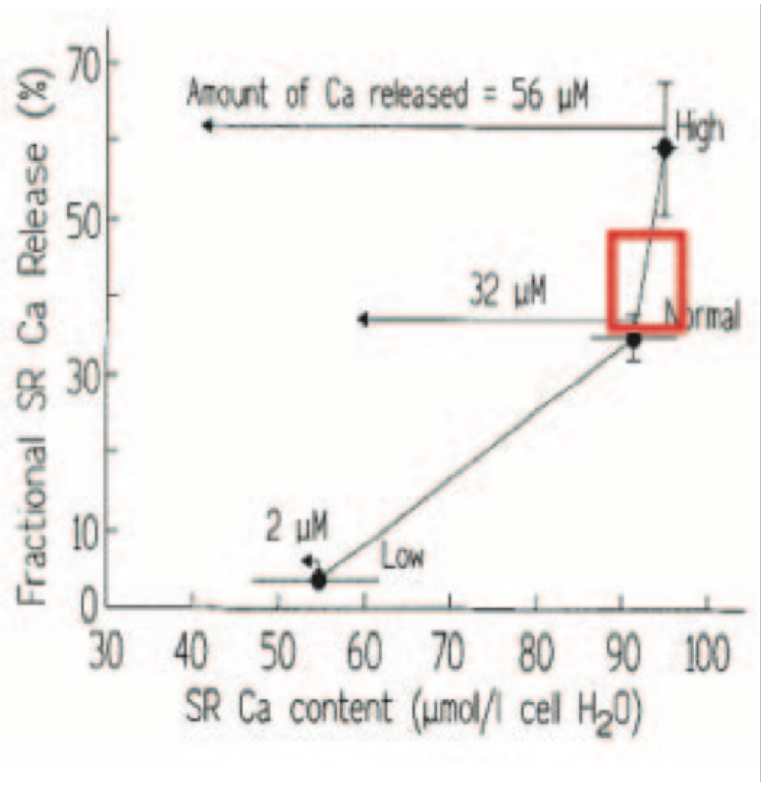


**Figure 1.9 Experimental measurements of SR $Ca^{2+}$ release** Experimental measurements of fractional SR $Ca^{2+}$ release as a function of SR $Ca^{2+}$ content. A steep relationship is observed at high SR $Ca^{2+}$ content levels.

*Reproduced from *J. Weiss, A. Karma, Y. Shiferaw et al., "From pulsus to pulseless: the saga of cardiac alternans," Circulation Research, vol. 98, no. 10, pp. 1244, 2006.*

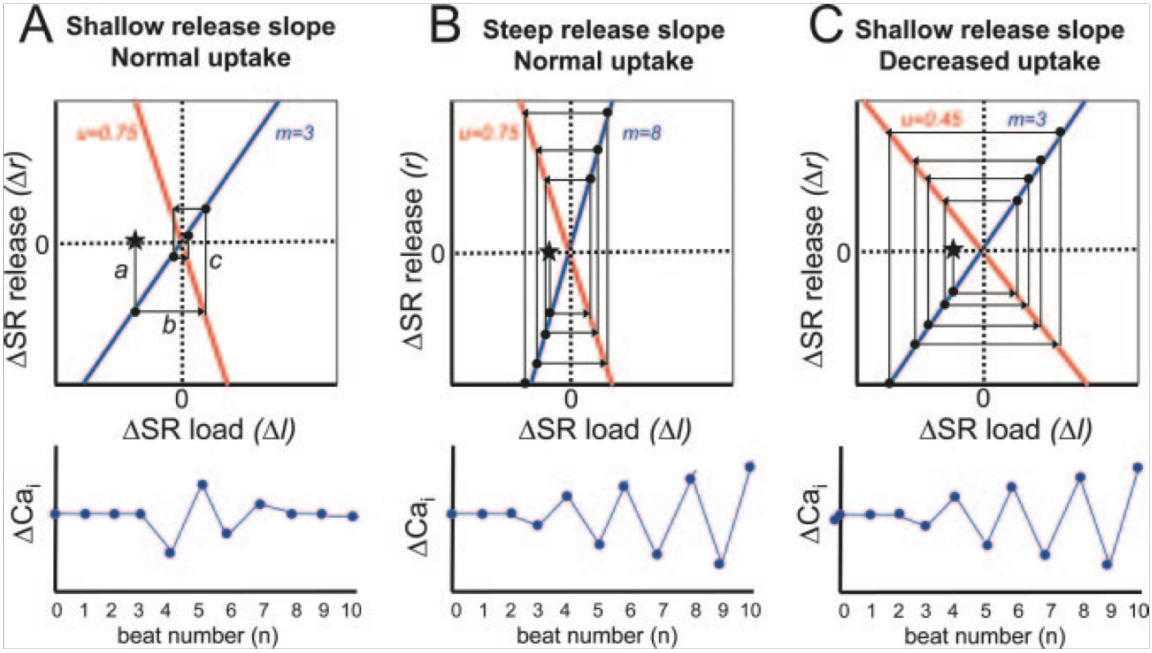


**Figure 1.10 $Ca^{2+}$ handling system iterative map**. Blue and red lines reflect the system of equations given by $\Delta r_n = m\Delta l_n$ and $\Delta r_n = -m/(m-1)(1-u)\Delta l_{n+1}$, respectively. Perturbations to equilibrium value (origin), will either dampen (A) or grow (B, C) in response to *u* and *m* parameters.

*Reproduced from *J. Weiss, A. Karma, Y. Shiferaw et al., "From pulsus to pulseless: the saga of cardiac alternans," Circulation Research, vol. 98, no. 10, pp. 1244, 2006.*

### *1.4.4 Bidirectional coupling of voltage and calcium*

As previously mentioned, transmembrane potential has a direct effect on calcium dynamics via the L-type calcium channel. In most cases, an increase in APD leads to an increased calcium transient – i.e., voltage → $Ca^{2+}$ coupling is positive. The effect of an increased calcium transient on voltage ($Ca^{2+}$ → voltage coupling), however, can be positive or negative. Calcium initially released from the SR serves to both inactivate $I_{Ca}$ (via the calcium-dependent $f_{Ca}$ gate), which acts to repolarize the cell, and it serves to increase NCX activity, which acts to depolarize the cell (via the $3Na^{+}$: $Ca^{2+}$ inward to outward ratio of ions which move across the cell). The relative contributions of both processes, determined by kinetics respective to each, will determine the ultimate direction of $Ca^{2+}$ → voltage coupling.

Regardless of the coupling, the end result is that APD alternans promotes $Ca^{2+}$ transient alternans, and vice versa. Whether alternans is the primary result of calcium instabilities or voltage instabilities is a widely discussed topic. Likely, no simple answer exists. Rather, voltage and $Ca^{2+}$ dynamics in real cell settings are probably always united in a context-specific yet inter-dependent relationship.

## 1.5 Spatially-extended Alternans Dynamics

### *1.5.1 Conduction velocity restitution*

Rapid pacing of cardiac tissue has interesting effects not only on single-cell APD dynamics but on wave-propagation as well. The relationship between wave-propagation speed (conduction velocity) and DI can be illustrated by the conduction velocity (CV) restitution relationship (Fig 1.11). Similar to the APD restitution

relationship, the CV restitution curve exhibits a flat response at sufficiently long DI values, but a steep dependence at shorter DI values. The shape of the CV restitution curve is dictated primarily by the kinetics of the sodium channels, whereby at sufficiently short DI values, sodium channel recovery from inactivation will be incomplete, resulting in less rapid depolarization during phase 0 of the action potential. The passive flux of current that is responsible for providing the stimulus to neighboring cells will therefore be lessened, resulting in slower wave propagation.

### *1.5.2 Concordant and discordant alternans*

In general, spatial manifestations of alternans can be either *concordant*, during which the beat-to-beat alternations in APD are in-phase at all points in space, or *discordant*, during which two distinct regions exhibiting relative out-of-phase behavior are present (Fig. 1.12). During spatially concordant alternans (Fig. 1.12, left-hand side), the APD values measured at each point alternate in unison, and as a result there exists no (or a relatively small) APD gradient on a beat-to-beat basis. During discordant alternans (Fig. 1.12, right-hand side), while the point in the top left (point a) exhibits a short-long pattern, the point in the bottom right (point b) exhibits a long-short pattern. In this case, on any given beat the action potential will either grow from short to long, as it does during the first action potential (propagation from top left to bottom right), or contract form long to short, as it does during the second action potential. Thus, for any given beat, the APD will vary as a function of space, yielding a positive APD gradient.

Due to the steep repolarization gradients associated, discordant alternans has been shown to be more arrhythmogenic than concordant alternans [13, 24], and as a result, there have been many attempts to understand and quantify discordant alternans

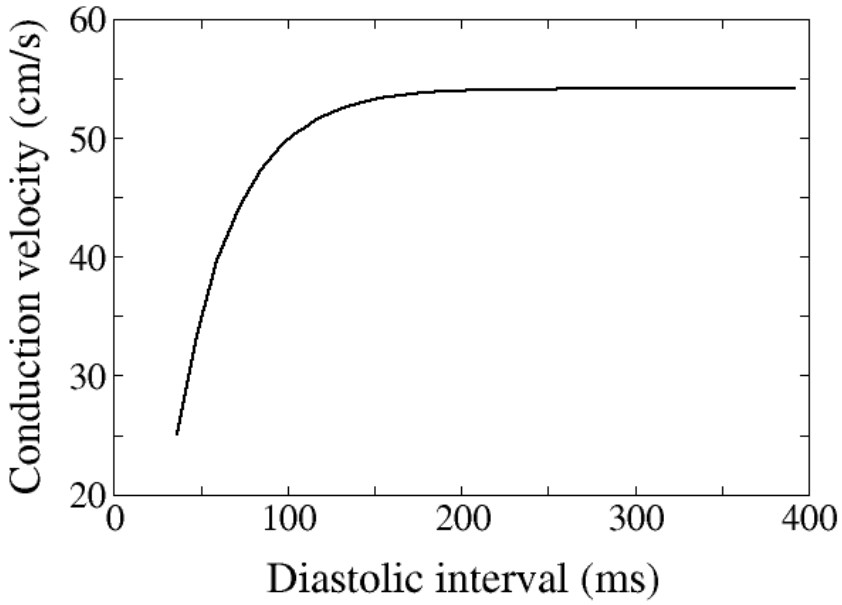


**Figure 1.11 Conduction velocity restitution**. At sufficiently long DI periods, action potential conduction velocity is at or close to the maximum value. Shorter DI intervals result in slower propagation due to incomplete recovery from inactivation of the sodium channels.

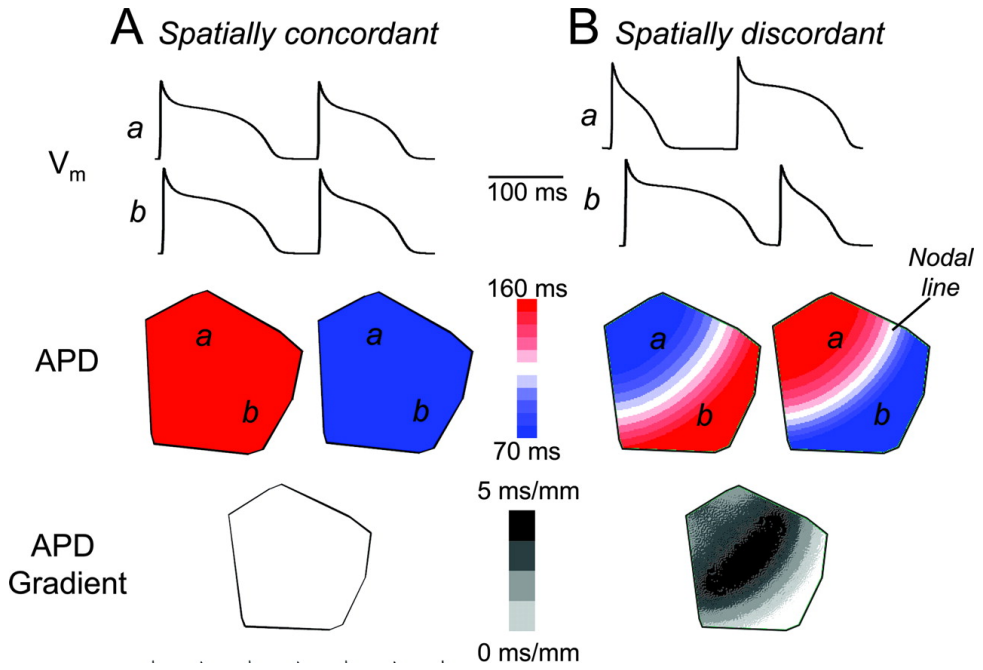


**Figure 1.12 Spatially concordant and discordant alternans.** Spatially concordant (A) and discordant (B) APD alternans in simulated 2-D cardiac tissue. A, Top traces show that simulated action potentials from sites *a* and *b* both alternate in a long-short pattern during pacing at 220 ms BCL. Second panel shows that the spatial APD distribution is either long (blue) or short (red for each beat). Third panel shows that the APD dispersion (gray scale) for either long or short beats is minimal. B, Top traces show that at a pacing BCL of 180 ms, simulated action potentials from site *a* now alternate short-long, whereas at the same time, action potentials from site *b* alternate long–short. Second panel shows the spatial APD distribution, with a nodal line (white) with no APD alternation separating the out-of-phase top and bottom regions. Third panel shows that the APD dispersion is markedly enhanced, with the steepest gradient (black) located at the nodal line.

*Reproduced from *J. Weiss, A. Karma, Y. Shiferaw et al., "From pulsus to pulseless: the saga of cardiac alternans," Circulation Research, vol. 98, no. 10, pp. 1244, 2006.*

behavior. Early analysis of discordant alternans formation suggested that tissue heterogeneities were the primary cause [13], however, more recent experimental, theoretical, and computational studies have provided evidence that suggest that such heterogeneities are not necessary [24]. It is now widely accepted that discordant alternans initiation can occur as a result of spatial and temporal interactions that arise between APD and CV restitution dynamics.

Fig. 1.13 illustrates an example of dynamically induced discordant alternans (from concordant alternans) in a computational simulation of a mathematically modeled 1-D cardiac cable. After a long action potential (A0) the cycle length is abruptly shortened and the resulting DI at the pacing site is small enough to engage CV restitution. The slowed conduction velocity results in an increasing DI gradient as a function of space, which leads to an increasing APD gradient (via APD restitution) during the propagation of the next action potential (A1). Propagation of the following wave (A2) encounters the opposite DI gradient resulting in a relatively long action potential at the top of the cable and a short action potential at the bottom of the cable. In this way repeated pacing at the same cycle length results in large-scale discordant alternans and the presence of large APD and repolarization gradients.

### *1.5.3 Conduction block and ventricular fibrillation initiation*

Steep repolarization gradients can lead to local *conduction block* when the wave front of an action potential collides with the wave back of a preceding action potential. In other words, the propagating wave encounters a region of refractoriness corresponding to an insufficient DI at which an action potential is unable to take-off. Conduction block that occurs as a result of steep repolarization gradients can lead to VF initiation. Pastore *et al*. [13] demonstrated this mechanistic link in their seminal

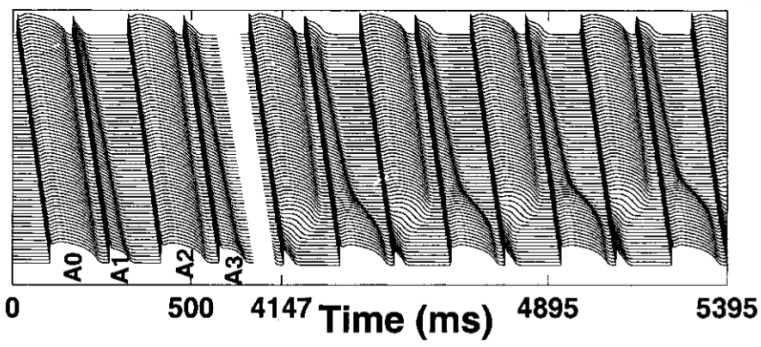


**Figure 1.13 Discordant alternans initiation example.** Top: The vertical axis denotes length of a cardiac cable (8 cm) and the horizontal axis denotes time. Action potential traces from 75 positions are shown. Sinus node scenario of discordant alternans initiation. All stimuli were applied at the top end of the cable at 310 ms intervals following a long quiescence. The second stimulus followed the maximum possible APD, and DI was short. The short DI produced slow conduction that gave rise to increasing DI as the wave front traveled down the cable, as seen in the mild increase in the DI preceding the excitation marked A1 and in the mild increase in APD (A1). The third stimulus followed a relatively long DI, producing maximum conduction velocity down the initial segments of the cable. Fast conduction coupled with APD increase down the cable on the previous beat produced decreasing DI and APD (A2) down the length of the cable. The reversal of DI spatial distribution (increasing down the cable for $S1_2$, decreasing for $S1_3$) was exaggerated as pacing continued, and gradually formed a node. The right part of the figure begins with the 13th excitation, and the top and bottom of the cable are clearly alternating out of phase.

*Reproduced from *M. A. Watanabe, F. H. Fenton, S. J. Evans et al., "Mechanisms for discordant alternans," J Cardiovascular Electrophysiology, vol. 12, no. 2, pp. 196, 2001.*

alternans study by mapping propagation and repolarization using optical mapping techniques. They were able to show how a slight reduction in pacing cycle length resulted in conduction block at the site of steepest repolarization gradient during steady-state discordant alternans (Fig. 1.14).

## 1.6 Alternans Control

### *1.6.1 Delayed feedback control*

Because of the putative link between APD alternans and the onset of ventricular fibrillation, concerted efforts have been made to develop means to terminate and/or prevent alternans in cardiac tissue. Derived from nonlinear dynamical systems analysis, closed-loop feedback mechanisms aimed at controlling alternans using single-site intervention from an external source has demonstrated promise as a therapeutic solution.

Most alternans control schemes trace their origins to the published study of Ott *et al*. in which the authors demonstrated a way to control a chaotic system to an underlying unstable periodic orbit using small time-dependent perturbations to an accessible system parameter [25]. Importantly, successful control was demonstrated possible without prior analytical knowledge of the system's dynamics.

In one of the first successful attempts at controlling an alternating cardiac rhythm, Christini *et al*. used a one-dimensional simplification of the aforementioned *Ott*-derived control scheme to suppress simulated AV nodal alternans [26]. (AV nodal alternans is characterized as a beat-to-beat alternation in AV-nodal conduction time,

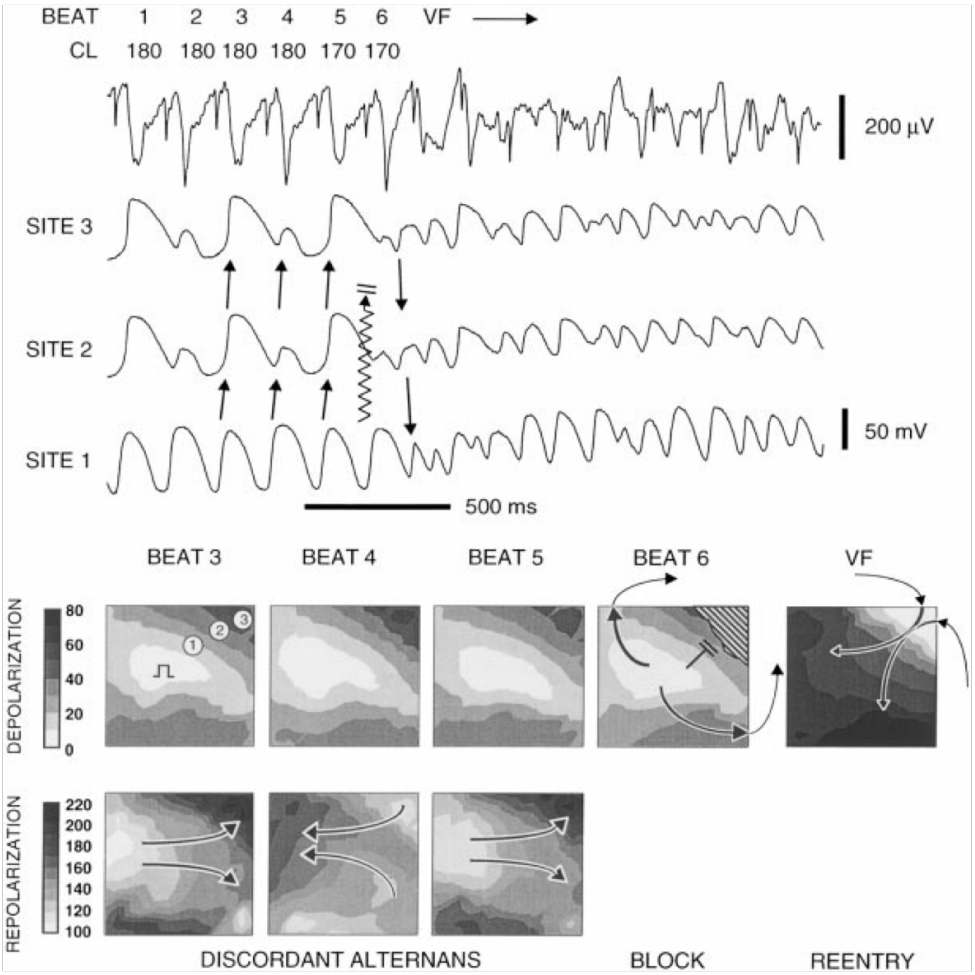


**Figure 1.14 VF initiation mechanism during discordant alternans.** Shown are 10-ms isochrone plots of depolarization and repolarization for beats that immediately preceded VF. Top, ECG and action potentials recorded from 3 ventricular sites marked on isochrone map (beat 3). Depolarization and repolarization times are referenced to stimulus artifact during pacing and to earliest activation time during first beat of VF. On beats 1 through 5, depolarizing wave front propagated uniformly from site of stimulation. However, patterns of repolarization differed substantially but reproducibly on alternating beats (compare beats 3 and 5). Pacing CL was decreased by 10 ms during beat 5. During beat 6, block occurred, as represented by hatched area in depolarization map. Block is shown in top panel by failure of propagation from site 1 to site 3. After block occurred, pattern of depolarization reversed from site 1→site 2→site 3 to site 3→site 2→site 1, indicating first reentrant beat that led to VF. First beat of VF occurred 120 ms after pacing artifact of beat 6.

*Reproduced from *J. Pastore, S. Girouard, K. Laurita et al., "Mechanism linking T-wave alternans to the genesis of cardiac fibrillation," Circulation, vol. 99, no. 10, pp. 1385, 1999.*

which occurs when the time between consecutive AV-nodal excitations becomes too short [26].) This work provided additional evidence suggesting that chaos control methods could be used to stabilize unstable periodic fixed points in non-chaotic systems. Subsequent experimental and clinical demonstrations of AV-nodal alternans control followed that utilized an improved control method capable of adapting to evolving system parameters (i.e., the implemented control algorithm could adaptively locate a varying fixed point on a beat-to-beat basis) [27-29]. Using this same control scheme, successful experimental control of APD alternans soon followed [30].

### *1.6.2 APD control algorithm*

The basic goal of the alternans control scheme implemented in this work is the same as that of the chaos control schemes of prior – to force the dynamical system to an underlying unstable fixed point. In this case, the underlying unstable fixed point is the period-1 rhythm, which was made unstable by the period-doubling bifurcation that normally occurs at fast stimulation periods [31]. By exploiting the APD restitution relationship [17], alternans control uses the APD information from consecutive action potentials to calculate the necessary adjustment to the cycle length in a manner that will decrease the alternans magnitude over time. The cycle length interval adjustment ($\Delta T$) and the resulting control-perturbed cycle length ($T_n$) are determined by the following equations:

$$T_n = \begin{cases} T^* + \Delta T_n & \text{if } \Delta T_n < 0, \\ T^* & \text{if } \Delta T_n \geq 0, \end{cases}$$

where **(3)**

$$\Delta T_n = (\lambda/2)(APD_n - APD_{n-1}), \quad \textbf{(4)}$$

$T^*$ is the target BCL (i.e., cycle length applied when control is turned off), $\lambda$ is the feedback gain, and $n$ is the beat number. In other words, given a sequence of alternating APDs (*L*-*S*-*L*-*S*), instances of $APD_{n-1}>APD_n$, which immediately follow relatively "short" (*S*) APDs and precede "long" (*L*) APDs, elicits a premature pulse ($T^*+\Delta T_n$) that effectively reduces the diastolic interval (DI) of the would-be "long" APD. This reduction in DI temporarily disrupts the steady-state alternating pattern by shortening the "long" APD and lengthening the subsequent "short" APD according to electrophysiological properties reflected in the APD restitution relationship. Included in Eq. 3 is a condition that allows for only premature stimulation. Allowing only cycle length shortening more accurately reflects what would happen in a clinical setting during which the native excitation of the heart, corresponding to cycle length = $T^*$, cannot be delayed. Interestingly, algorithms using only negative perturbations have been shown analytically to have a larger successful control regime than those that apply both positive and negative perturbations [32].

Fig. 1.15 is a simple graphical illustration of how alternans control works using the cobweb diagram framework. As shown previously, sufficiently fast static pacing yields a steady-state period-2 rhythm (Fig. 1.15A). During the application of control (Fig. 1.15B) the cycle length is reduced according to Eq. 3 after completion of the short action potential, leading to a shortened DI and as a consequence, the APD of the following action potential is closer to the location of the unstable fixed point. (The feedback gain, $\lambda$, determines how close the resulting APD will be to the fixed point.) Repeated applications of control (i.e., cycle length perturbations) are required in order to maintain a relatively constant beat-to-beat pattern because of the system's dynamically-induced tendency towards an alternans rhythm.

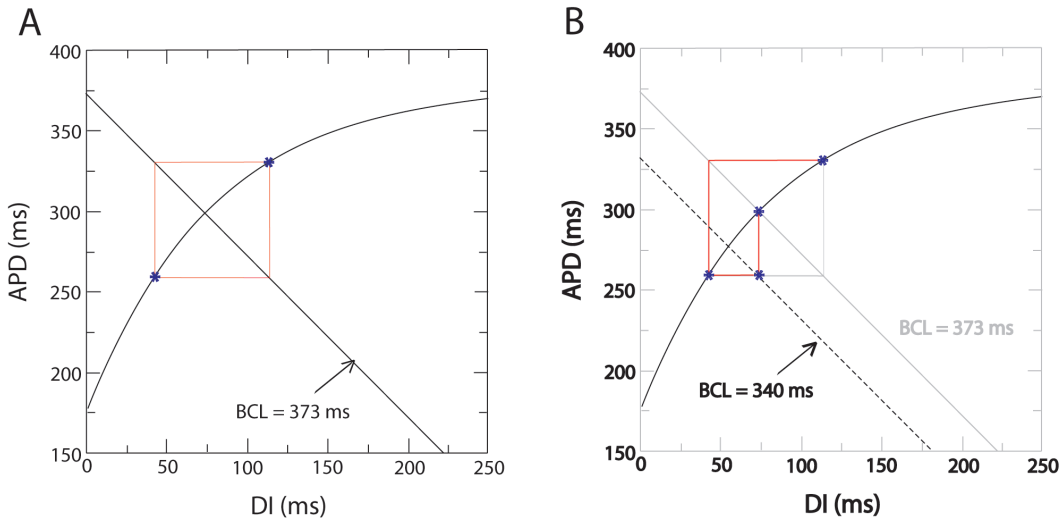


**Figure 1.15 Graphical illustration of alternans control.** A) steady-state alternans due to steep APD restitution. B) Alternans control application results in cycle length shortening, which subsequently shortens what would have been a "long" action potential. Feedback value, $\lambda$, in conjunction with APD restitution morphology determines how close the resulting APD is to the fixed point. Repeated applications of control stimulus are needed to maintain a constant beat-to-beat pattern.

### *1.6.3 Spatially-extended single-site control*

Reports of successful control in experimental settings include the suppression of APD alternans in small isolated frog heart preparations [30] and in single myocytes [33]. Despite these successes, however, complete alternans control has so far been limited to these small-scale systems (i.e., single-cell or sufficiently small tissue preparations) that do not allow for spatiotemporal variations in wave-propagation or repolarization dynamics – single-site control of physically larger systems has proven to be more difficult.

Echebarria and Karma set out to quantify the spatial extent to which alternans can be suppressed by a single electrode as a function of stimulation period [34]. The authors simulated cases of APD-restitution derived alternans (a.k.a., voltage-driven alternans) in spatially homogeneous 1-D cardiac tissue models of Purkinje cells (Noble cell model [35]) in which alternans and alternans control was applied at a single proximal site. Alternans control was achieved using an algorithm capable of positive and negative perturbations (i.e., the *if* condition of Eq. 3 was ignored). Alternans and alternans control was studied in 1-D cables ranging in length from 0.5 cm to 5 cm and 200 stimuli were given at the proximal site at a range of pacing cycle lengths for both static and control scenarios. The stability diagrams summarizing the computational results of the study are reproduced in Fig. 1.16.

The main result was that control was effective up to some maximum cable length, $L_{max} \approx 1$ cm for pacing cycle lengths that were slightly beyond the bifurcation point. This observation was supported by their theoretical analysis, which recast spatiotemporal alternans behavior as an amplitude equation amenable to linear stability techniques. The mathematical analysis produced an equation for $L_{max}$:

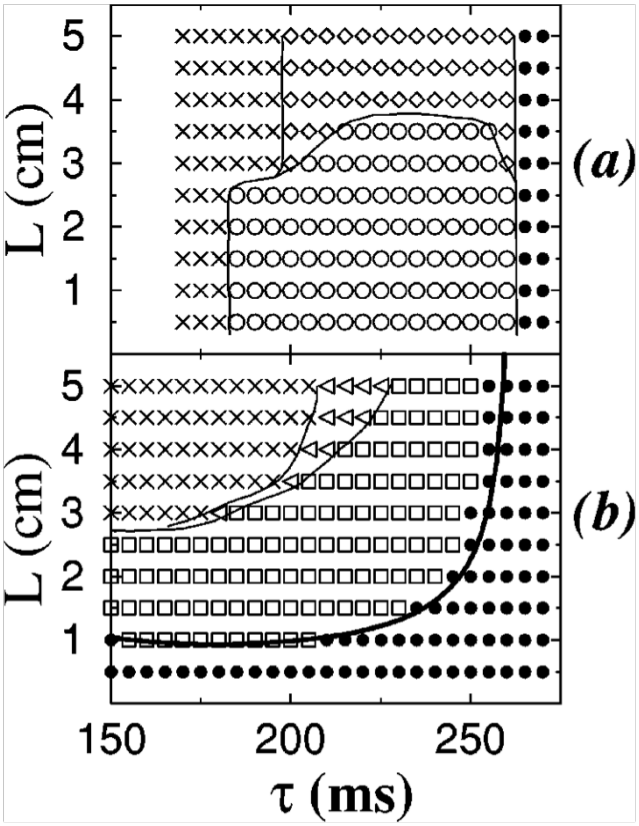


**Figure 1.16 Stability diagram of alternans control – Purkinje fiber computational study.** Stability diagrams showing the regions of existence of different patterns of alternans in the place of pacing period τ and cable length L for (a) γ=0 (without control) and (b) γ=1/2 (with control). The symbols in (a) and (b) correspond to no alternans (solid circles), concordant alternans with a nearly constant amplitude (open circles), first harmonic standing waves (open squares) that are only present when control suppresses the open circle concordant alternans, discordant stationary alternans (diamonds), traveling discordant alternans (triangles), and conduction block (crosses). The thin solid lines are guides to the eye. The thick solid line in (b) is the theoretical prediction for the onset of alternans with control.

*Reproduced from *B. Echebarria, and A. Karma, "Spatiotemporal control of cardiac alternans," Chaos: An Interdisciplinary Journal of Nonlinear Science, vol. 12, pp. 923, 2002.*

$$L_{\max} \approx \xi \frac{2^{1/2}\pi}{[f_c^{"}(\tau - \tau_c)]^{1/2}} \approx \xi \frac{\pi}{[\ln(f')]^{1/2}} \quad \textbf{(5)}$$

which suggested that the spatial extent of alternans control is dependent on conduction velocity (via the $\xi$ term).

Purkinje fiber alternans control experiments that followed confirmed the results of Echebarria and Karma [36]. Cardiac Purkinje fibers obtained from adult mongrel dogs were subjected to similar pacing protocols and the qualitative results matched well (Fig. 1.17). Spatially-extended control of alternans was possible only if the alternans magnitude was small, and spatial attenuation of control was observed at pacing rates that elicited large-scale alternans. The controllable unit for single-site control was shown to be ≈1 cm.

Still missing, however, is a better understanding of alternans and alternans control dynamics in the more clinically relevant ventricular tissue. In particular, the spatial extent of alternans control in ventricular tissue is needed if more complex methods of alternans suppression (e.g., multisite control) are to be developed for clinical use. Given the results yielded by the linear stability analysis of general alternans behavior, which suggests that spatial controllability of alternans is dependent on CV, one would expect that alternans control would behave differently in ventricular tissue (CV < 100 cm/s [37-39]) as compared with Purkinje fibers (CV ≈ 200 cm/s [40]).

Aiming to fill this knowledge void, in this study we investigated alternans and alternans control dynamics both computationally and experimentally. 1-D simulations of modeled ventricular tissue were performed under various alternans dynamics

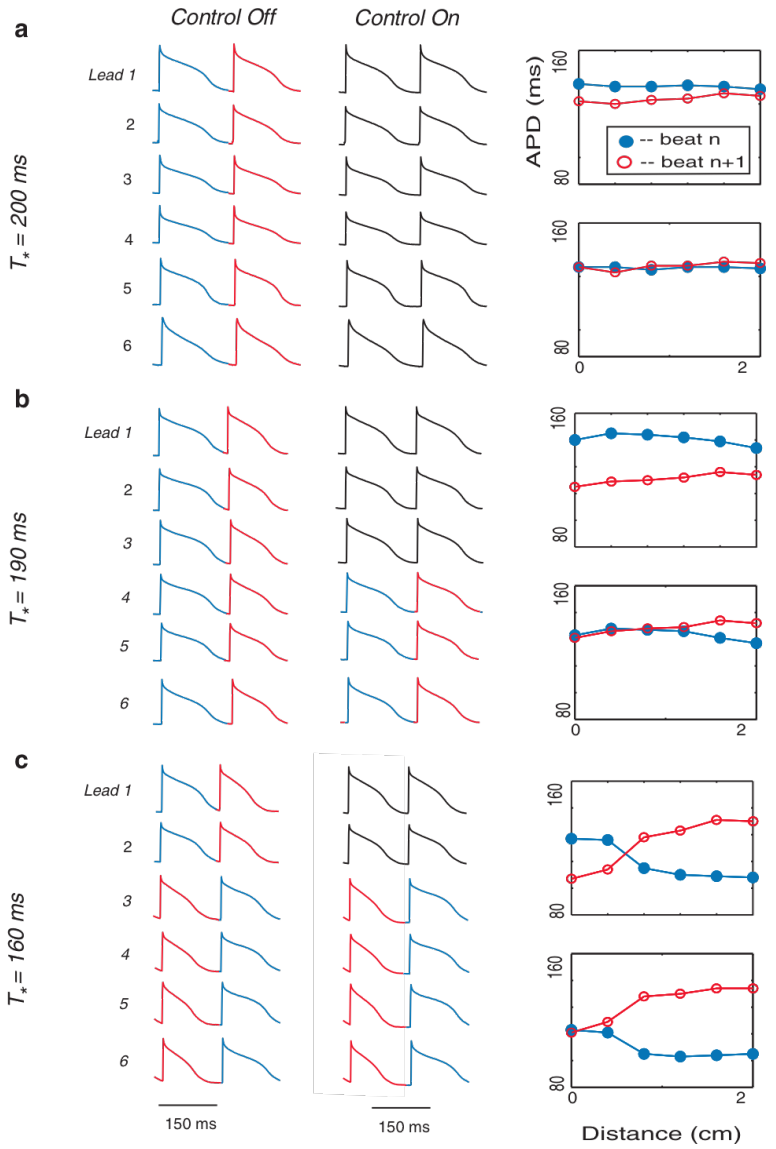


**Figure 1.17 Alternans control example in Purkinje fiber experimental study**. Data from two consecutive action potentials recorded from 6 microelectrodes spaced along the length of a Purkinje fiber (Lead 1 is proximal; Lead 6 is distal) in one representative control experiment. Stimulation was applied to the proximal end of the fiber near microelectrode 1 (x = 0 cm). For each of the three rows [(a), (b), and (c)]: (1) $T^*$ is shown on the left, (2) membrane potential vs. time for microelectrodes 1 though 6 (which correspond to x =0 and 2 cm, respectively) are shown in the left column (before control) and middle column (during control), and (3) the right column shows APD values computed from the six microelectrodes for the same alternate beats before (top panels) and during (bottom panels) control. During control, stimulation was adapted according to Eq. (1). In the middle column, action potentials for which control failed to eliminate alternans are shown in red and blue, while those in which alternans was suppressed are shown in black.

*Reproduced from *P. Jordan, and D. Christini, "Characterizing the contribution of voltage-and calcium-dependent coupling to action potential stability: implications for repolarization alternans," American Journal of Physiology- Heart and Circulatory Physiology, vol. 293, no. 4, pp. H2109, 2007.*

settings (Chapter 2). Global control results and the spatial extent of control were obtained and analyzed. The experiments were conducted on arterially perfused canine right ventricular preparations (Chapter 3). High-resolution transmembrane voltage data were obtained from the cardiac tissue surface using a previously developed optical mapping system capable of real-time control application [41]. In addition to these studies, a further investigation into the nature of control in the presence of noise was done in an effort to better understand the limits and implications of alternans control in experimental settings (Chapter 4).

CHAPTER 2

# SPATIOTEMPORAL CONTROL OF ACTION POTENTIAL DURATION ALTERNANS IN SIMULATED VENTRICULAR TISSUE

## 2.1 Outline

The first published study on the spatiotemporal nature of alternans control studied the effect of single-site proximal control in 1-D cables using computational simulations and theoretical analysis. The data presented *therein* were that of simulations that implemented the Noble cell model of the Purkinje fiber cell type. Global stability diagrams were constructed by simulating alternans behavior over a range of cable lengths and pacing frequencies with and without the application of alternans control. The simulation results, corroborated by theoretical analysis, suggested that single-site alternans control was able to shift the onset of alternans in sufficiently long cables by only a small amount and that this was due to the fact that control became spatially attenuated at pacing rates slightly beyond the bifurcation cycle length – i.e., control was successful only at points very close to the control point.

Clinical realization of electrode-based control schemes requires a comprehensive understanding of alternans control dynamics in ventricular tissue. The study presented *herein* provides the first step towards that end. In this chapter, alternans control is investigated using computational simulations of the Shiferaw-Sato-Karma (SSK) cell model of the ventricular cell type. Control was studied under three different parameter regimes in an effort to probe the full terrain of dynamical possibilities. Global stability diagrams were constructed in the same manner as the previously published Purkinje fiber study – data was generated for a range of cable

lengths and pacing frequencies. The final result was that in all three parameter regimes, control dissipated sharply as a function of distance at pacing cycle lengths slightly beyond the onset of alternans (for cable lengths >2 cm), lending further support for the contention that alternative methods, e.g., multisite control, will be necessary for clinical application of electrode-based alternans control.

## 2.2 Introduction

Numerous studies have shown that it is possible to suppress temporal alternans by using closed-loop feedback control of the pacing interval [26-30, 33]. Examples include the control of alternations in AV nodal conduction time (AV-nodal alternans) *in situ* [26], *in vitro* [28], and in humans [29], the control of APD alternans in small isolated frog heart preparations [30], and APD alternans control in single myocytes [33]. These successes have given reason to believe that control of APD alternans in ventricular tissue using properly timed electrode interventions may be possible. In order to do so clinically, however, requires that adequate control occur both temporally and spatially.

The first attempt to tackle this issue was a computational and theoretical study published by Echebarria and Karma in which they applied control perturbations to the proximal end of a simulated 1-D cable and analyzed the alternans dynamics across a range of cable lengths and cycle frequencies [34]. The results suggested that spatiotemporal control of alternans is severely limited – successful control along an entire cable of sufficient length (>1 cm) was possible only at pacing rates very close to the bifurcation period. The dynamics were such that during failed control, the

alternans magnitude was suppressed only at points very close (≈1 cm) to the site of control intervention.

The results presented in the Echebarria and Karma study were derived from the Noble cell model of the Purkinje fiber. The theoretical analysis that accompanied the simulations showed how the maximum control length ($L_{max}$) depends on, amongst other things, the action potential conduction velocity characteristics. Studying alternans and alternans control dynamics in ventricular tissue, which has different conduction properties as compared with the Purkinje fiber, is therefore a necessary step towards the clinical realization of alternans control.

### *2.2.1 Shiferaw-Sato-Karma cardiac cell model*

Ventricular myocytes were simulated using the Shiferaw-Sato-Karma (SSK) cell model [18]. The SSK model is an amalgamation of the sarcolemmal ionic currents of the Fox model [42], which was derived from experimental alternans data obtained from canine ventricular tissue, and it includes an advanced intracellular calcium system [22], which incorporates $Ca^{2+}$ handling dynamics derived from rabbit experiments [20]. Thus, the SSK model is not representative of any one animal species. The SSK model is, however, capable of producing a wide range of alternans dynamical behavior.

By varying specific parameters, the SSK model can be made to exhibit alternans primarily driven by voltage dynamics, calcium dynamics, or as a combination of both. Specifically, different pairings of the parameters $u$ (the SR release slope) and $t_f$ (the time constant of voltage dependent inactivation of the L-type calcium channel) will produce the different alternans types [18, 43].

Relating to voltage-driven alternans: steep APD restitution via slow calcium channel inactivation kinetics can induce alternans at fast pacing cycle lengths (See *Section 1.4.1* for details). In the SSK model the L-type calcium current is modeled as follows:

$$I_{Ca} = \bar{I}_{Ca} f d f_{Ca} \quad \textbf{(1)}$$

where $\bar{I}_{Ca}$ determines the maximum amount of current possible, and $f$, $d$, and $f_{Ca}$ describe the kinetics of the inactivation and activation gating processes. Increasing the time constant $\tau_f$ of the inactivating $f$ gate steepens the APD restitution curve and promotes voltage alternans [18].

Similarly, a steep dependence of SR $Ca^{2+}$ release on SR $Ca^{2+}$ load can induce alternans at fast pacing cycle lengths (See *Section 1.4.3* for details). In the SSK model, the SR release to SR load relationship is determined by the function $Q(c'_j)$, where $c'_j$ is the average junctional SR (JSR) concentration of calcium (JSR is the compartment of the SR immediately adjacent to the ryanodine receptors) . The slope, $u$, of the function $Q(c'_j)$ determines the SR release sensitivity to calcium load: $u = \partial Q / dc'_j$. Increasing $u$ steepens the sensitivity and promotes $Ca^{2+}$ alternans [18].

Using a novel eigenvalue based methodology, the stability characteristics of the SSK model were studied by Jordan *et al*. [43]. By selectively clamping the cell to either a fixed APD or a $Ca^{2+}$ transient waveform, the authors were able to determine the relative (in)stability of the voltage and calcium system for a given parameter set. Fig. 2.1 shows the results of the eigenvalue analysis on the SSK model with varied combinations of $u$ and $\tau_f$.

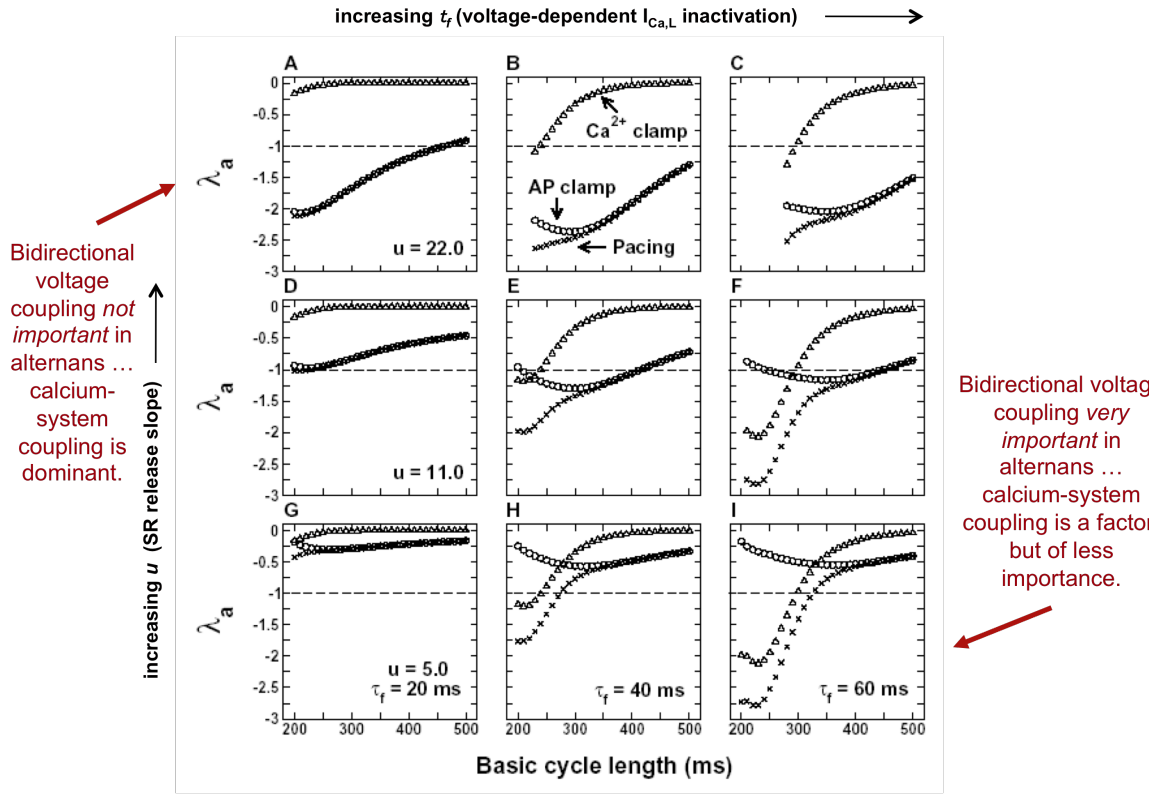


**Figure 2.1 SSK cell model parameter-regime eigenvalue stability results**. $\lambda$ as a function of cycle length for the SSK model during pacing (x), AP clamping (o), and calcium-transient clamping (Δ). Different combination of values for parameters $u$ and $\tau_f$ as indicated. Differences in the stability between pacing/AP clamp and between pacing/$Ca^{2+}$ clamp reveal stability characteristics for the voltage and calcium system, respectively.

*Reproduced from *P. Jordan, and D. Christini, "Characterizing the contribution of voltage-and calcium-dependent coupling to action potential stability: implications for repolarization alternans," American Journal of Physiology- Heart and Circulatory Physiology, vol. 293, no. 4, pp. H2109, 2007.*

The top left of the figure (panel A) shows the eigenvalue analysis results of the SSK model with $u$ = 22.0 $s^{-1}$ and $\tau_f$ = 20.0 ms. The parameters chosen correspond to a steep dependence of SR release on SR load (i.e., large $u$) and a fast voltage-dependent inactivation of $I_{Ca}$ (i.e., small $\tau_f$). The stability results confirm that the instability of alternans under these parameters is primarily driven by $Ca^{2+}$. In the same way, the results of the bottom right panel (I) show that alternans is predominantly driven by the dynamics of the voltage system when $u$ = 5.0 $s^{-1}$ and $\tau_f$ = 60.0 ms.

Informed by these results, $u/\tau_f$ parameter combinations of 5.0/60.0 and 22.0/20.0 were chosen in this study to represent voltage and $Ca^{2+}$-driven alternans respectively, whereas 9.0/30.0 was used to simulate the "default" parameter regime representing roughly equal amounts of voltage and calcium instability.

Other pertinent parameter settings include: $G_{Ks}$:$G_{Kr}$ ratio ≈ 11 (so as to reflect endocardial tissue) [44, 45]; temperature = 310°K.

### *2.2.2 Simulation protocol*

A one-dimensional cable representation of a ventricular fiber was simulated in custom C code using the following equation:

$$\frac{\partial V(x,t)}{\partial t} = D\frac{\partial^2 V(x,t)}{\partial x^2} - \frac{I_{ion} + I_{stim}}{C_m} \qquad \textbf{(2)}$$

where $V$ is the membrane potential, $t$ is the time, $D$ is the tissue diffusion coefficient, $I_{ion}$ is the sum of the transmembrane ionic currents (Hodgkin and Huxley formulations, Ref. [46]), $I_{stim}$ is the externally applied stimulus current (for this model we used 150 μA/$cm^2$ square-wave pulses, 1 ms duration), and $C_m$ is the membrane capacitance (1 μF/$cm^2$ for this model). Numerical integration was done using the forward-Euler

scheme, utilizing operator splitting and adaptive time stepping [47] (0.001 ms ≤ dt ≤ 0.025) techniques to minimize computational time. A diffusion constant of 0.001 $cm^2$/ms (integrated with a spatial step size of 0.01 cm) was used. The $\gamma$ term in the model was set at 0.2, which promoted positive $Ca^{2+}$ → voltage coupling [18] (see *Section 1.4.4* for details).

1-D cables of lengths varying from 0.5–5.0 cm in 0.5 cm increments were simulated. For each cable length, BCL ($\tau$) pacing began at a value sufficiently large enough so as to elicit non-alternating APDs. Progressively shortening $\tau$ values (in 5 ms increments) resulted in alternans behavior of increasing magnitude and ultimately 2:1 conduction block (data not shown). 1200 stimuli were applied to the proximal end of the cable (600 no-control; 600 control) for each value of $\tau$. APD values were calculated at each spatial point using V = -60 ms as the threshold.

The alternans control algorithm was as follows:

$$T_n = \begin{cases} T^* + \Delta T_n & \text{if } \Delta T_n < 0, \\ T^* & \text{if } \Delta T_n \geq 0, \end{cases}$$

where **(3)**

$$\Delta T_n = (\lambda/2)(APD_n - APD_{n-1}), \quad \textbf{(4)}$$

($\Delta T$ – cycle length interval adjustment; $T_n$ – resulting control-perturbed cycle length), $T^*$ is the target BCL (i.e., cycle length applied when control is turned off), $\lambda$ is the feedback gain, and $n$ is the beat number. The feedback gain was 1.6.

### *2.2.3 Equations*

*Alternans Magnitude Calculation*

The APD alternans magnitude for a given series of action potentials was calculated according to the following:

Given a sequence of $n$ positive real APD values, $A$:
$A = (A_1, A_2, \ldots, A_n)$,
alternans magnitude, $A_M$, is defined as:

$$A_M = \left( \sum_{i=1}^{n-1} \left| A_{i+1} - A_i \right| \right) / (n-1) \quad \textbf{(5)}$$

### *2.2.4 Data selection*

For the global stability analysis, the alternans cutoff was set at 10 ms (i.e., $A_M <$ 10 ms was labeled as no alternans). In order to obtain results from steady-state behavior, $A_M$ and $A_{M,S}$ (spatially averaged alternans) were calculated from the last 50 action potentials during both control-off and control-on conditions.

## 2.3 Results

### *2.3.1 SSK restitution curve*

The APD restitution curves for each of the three parameter regimes (default, voltage-driven alternans, $Ca^{2+}$-driven alternans) are in shown in Fig. 2.2. The voltage-driven alternans parameter combination produced a restitution curve with a steep slope (>>1), whereas the $Ca^{2+}$-driven case produced a restitution curve with a shallow slope (<1). CV restitution showed that maximum conduction velocity was close to equal in all three cases (≈50 cm/s).

### *2.3.2 SSK spatial profile examples*

Fig. 2.3 includes example spatial profiles of the APD and alternans dynamics along a 3 cm 1-D cable observed during control-off and control-on conditions. A-C are derived from pacing at BCL = 275 ms, whereas D-F are derived from pacing at

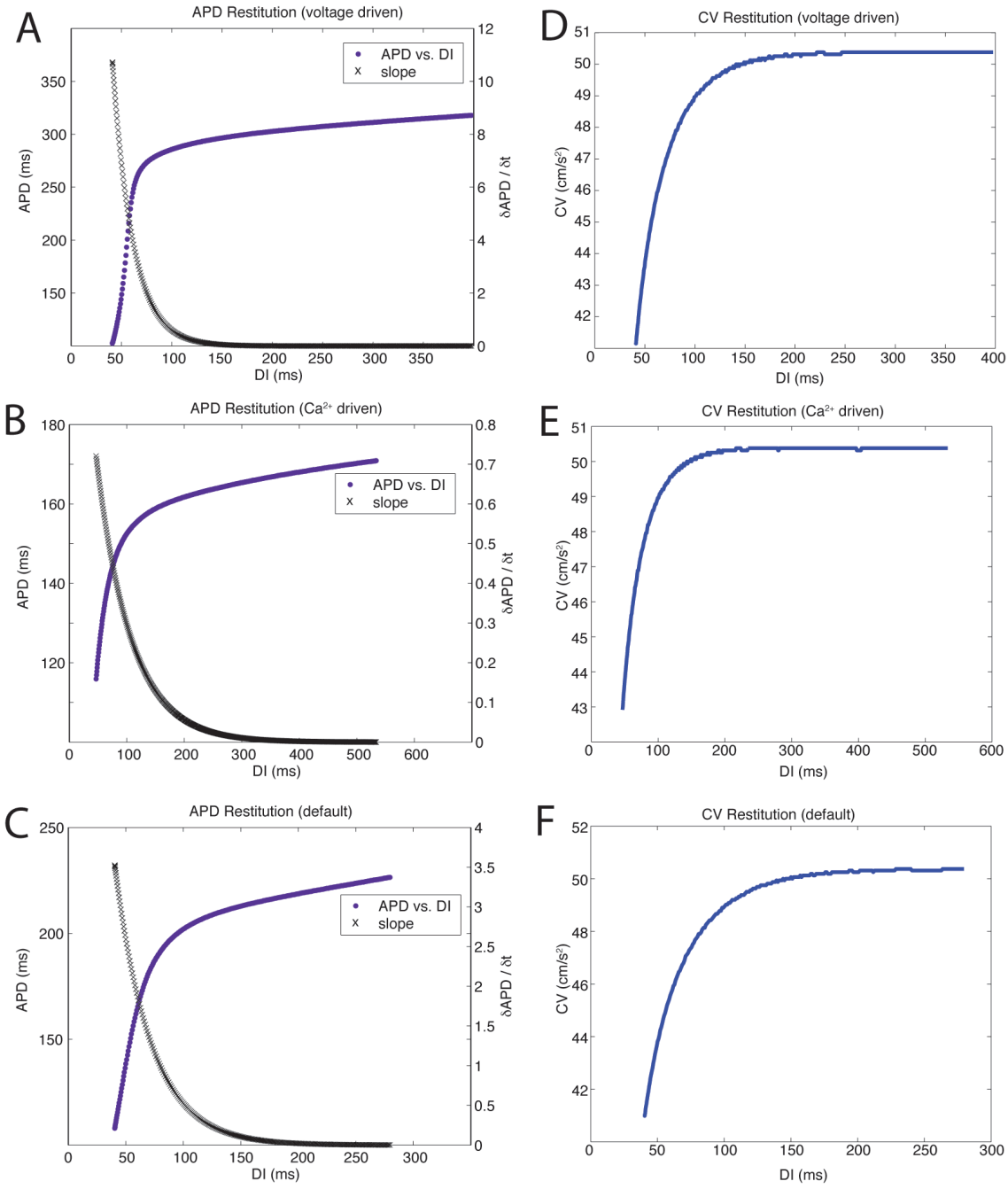


**Figure 2.2 SSK cell model restitution curves under different alternans parameter settings.** Left column; left axis – restitution curves for the SSK model under voltage-driven ($u$ = 9.0, $\tau_f$ = 30.0), $Ca^{2+}$-driven ($u$ = 22.0, $\tau_f$ = 20.0), and default settings ($u$ = 5.0, $\tau_f$ = 60.0). Left column; right axis – slope of the restitution curve (fitted to three term exponential). Right column – CV restitution curves. All curves derived from S1-S2 restitution protocol[1].

[1] *Y. Shiferaw, Z. Qu, A. Garfinkel et al., "Nonlinear dynamics of paced cardiac cells," annals-New York Academy of Sciences, vol. 1080, pp. 376, 2006.*

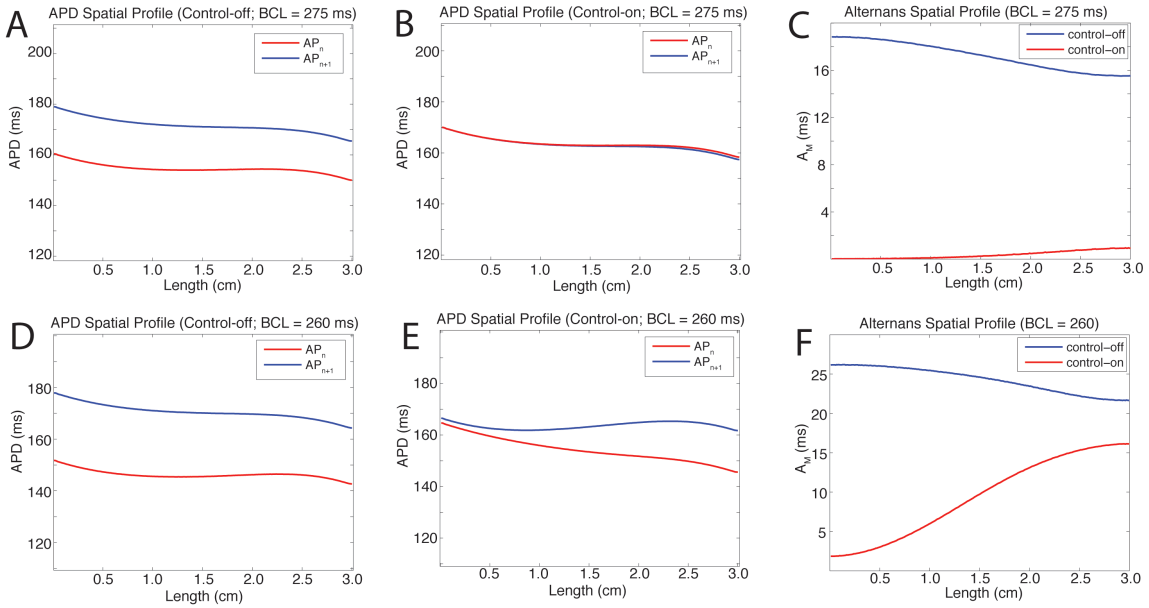


**Figure 2.3 Spatial profile of APD and alternans magnitude of successive action potentials along a 3 cm 1-D simulated cable.** (n-red, n+1-blue) Pacing administered at proximal (left) end only. Top – static pacing; bottom – control perturbed pacing. (A-C) BCL = 275 ms. (A) concordant alternans is observed during control-off and (B) eliminated during control-on. (C) Average alternans magnitude profile illustrates the decrease in alternans that accompanied the application of control. (D-F) BCL = 260 ms. (D) Concordant alternans is observed during control-off. (E) Control fails a short distance from pacing site during control-on. (F) Average alternans magnitude during control-on illustrates spatial alternans behavior. All data derived from SSK "default" parameter settings.

BCL = 260 ms. In A, B, D, and E, the APD values of two successive action potentials (*n*-red, *n+1*-blue) are plotted as a function of space. A and D are the APD spatial profiles during control-off, and in both, static pacing caused concordant alternans to form along the whole length of the cable. B and E are the APD spatial profiles obtained during the application of control. Pacing at a rate of BCL = 275 ms allowed for control to eliminate alternans along the entire length of the cable whereas pacing at a faster rate of BCL = 260 ms resulted in the suppression of alternans at points close to the pacing site only. C and F, reflect the control-off and control-on results by plotting the steady-state $A_M$ values as a function of space.

### *2.3.3 SSK global results*

Fig. 2.4 shows the global alternans results derived from cable lengths ranging from 0.5–5.0 cm, paced at a range of BCLs. The simulation results for both control-off and control-on scenarios are given for each of the three parameter regimes. For each simulation, the steady-state behavior of the 1-D cable dynamics was characterized as no-alternans or alternans.

Under the default parameter settings, alternans control was able to delay the onset of alternans considerably for shorter cable lengths (L < 2 cm). At longer cable lengths, however, only a small improvement in alternans onset was observed (0-10 ms for 2 cm < L ≤ 5 cm). The global stability results derived from the voltage-driven parameter settings suggest that control was relatively less successful at shorter cable lengths (L < 2 cm) and relatively more successful at longer cable lengths (L > 3 cm), compared with the default setting simulations, at delaying the onset of alternans. The results from the calcium-driven parameter setting suggests that alternans control was able to dramatically delay the onset of alternans in short cables (L < 2.5 cm), but the

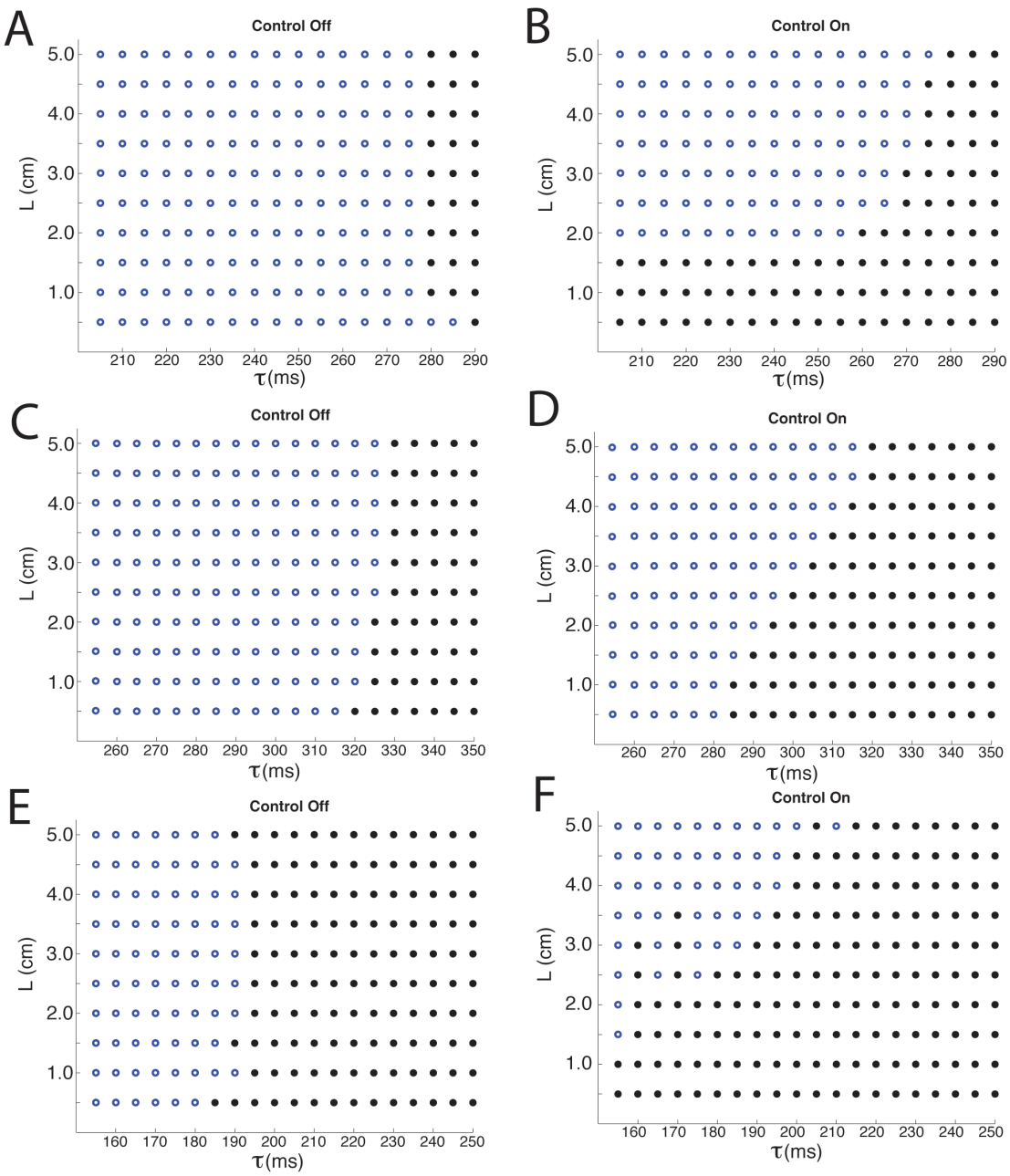


**Figure 2.4 SSK cell model stability diagram for 1-D cable under different alternans parameter settings**. Global results from control-off (A, C, E) and control-on (B, D, F) scenarios. The symbols correspond to no-alternans (solid circles) and alternans (open circles). (A-B) Default settings ($u$ = 5.0, $\tau_f$ = 60.0). Complete alternans control regardless of BCL at sufficiently short cable lengths (<2 cm). Proximal control delayed the onset of alternans by 0-10 ms for L ≥3 cm. (C-D) Voltage-driven settings ($u$ = 9.0, $\tau_f$ = 30.0). Proximal control delayed the onset of alternans by a decreasing amount with respect to an increasing cable length. Calcium-driven settings ($u$ = 22.0, $\tau_f$ = 20.0). Complete control at short cable lengths (L<2.5 cm). Alternans onset occurs sooner during alternans control in longer cables (L≥4 cm).

results in longer cables were ambiguous (the onset of alternans began slightly sooner as a result of control in some cases).

### *2.3.4 Spatial efficacy of alternans control*

In order to understand the simulation results better, the spatial efficacy of alternans control was quantified by averaging the $A_M$ values across regions of space, resulting in spatially averaged alternans magnitudes, $A_{M,S}$. Spatial dynamics were investigated in this way for three different cable lengths (L = 3, 4, and 5 cm) under each of the three parameter regimes. Regions of tissue corresponding to 1 cm were used for the $A_{M,S}$ calculations.

Table 2.1 shows the spatially averaged results for the subregions of tissue simulated using the default parameter setting. For L = 3 cm, during control-off conditions, large concordant alternans were produced for all BCL < 280 ms. The noted decrease in $A_{M,S}$ at regions distal to the site of stimulation is similar to the results shown in the Purkinje fiber simulation studies of Echebarria and Karma [34]. During the application of control, alternans is suppressed to magnitudes less than 10 ms within the proximal (0-1 cm) region for all BCL values >230 ms. In addition, spatial attenuation of alternans control is demonstrated clearly by an increase in $A_{M,S}$ as a function of space for BCL < 270 ms during control-on conditions.

The spatially averaged alternans results for L = 4 cm and 5 cm simulated under the default parameter regime are shown in Table 2.1 as well. The results from L = 4 cm are similar to that of L = 3 cm, however, the results from L = 5 cm are different because of the presence of discordant alternans (denoted by the yellow highlighted BCL cells) during control-off conditions. It should be noted that for L = 5 cm,

## Color Code

| Control Off | |
|---|---|
| (0-10) | |
| (10-20) | |
| (20-30) | |
| (30-40) | |
| (40-50) | |
| (50-60) | |
| (60-70) | |
| (70-80) | |
| (80+) | |

| Control On | |
|---|---|
| (0-10) | |
| (10-20) | |
| (20-30) | |
| (30-40) | |
| (40-50) | |
| (50-60) | |
| (60-70) | |
| (70-80) | |
| (80+) | |

| Control Diff | |
|---|---|
| (0-10) | |
| (10-20) | |
| (20-30) | |
| (30-40) | |
| (40-50) | |
| (50-60) | |
| (60-70) | |
| (70-80) | |
| (80+) | |

| Control Diff | (negative) |
|---|---|
| (0-10) | |
| (10-20) | |
| (20-30) | |
| (30-40) | |
| (40-50) | |
| (50-60) | |
| (60-70) | |
| (70-80) | |
| (80+) | |

**Spatially Averaged Alternans Results (Default Setting, 3 cm)**

**2.1.1**

| | Control-OFF | | |
|---|---|---|---|
| **BCL** | 0-1 cm | 1-2 cm | 2-3 cm |
| 280 | 3.0 | 2.1 | 2.0 |
| 275 | 18.6 | 17.3 | 16.0 |
| 270 | 20.8 | 19.6 | 18.2 |
| 265 | 23.0 | 22.0 | 20.3 |
| 260 | 26.0 | 24.5 | 22.4 |
| 255 | 29.7 | 27.9 | 25.0 |
| 250 | 34.5 | 32.1 | 28.4 |
| 245 | 40.7 | 37.6 | 33.0 |
| 240 | 49.0 | 44.8 | 38.6 |
| 235 | 58.5 | 53.3 | 45.5 |
| 230 | 69.2 | 62.7 | 53.2 |
| 225 | 80.0 | 72.3 | 61.2 |
| 220 | 90.6 | 81.6 | 69.0 |

**2.1.2**

| | Control-ON | | |
|---|---|---|---|
| **BCL** | 0-1 cm | 1-2 cm | 2-3 cm |
| 280 | 0.0 | 0.0 | 0.0 |
| 275 | 0.0 | 0.0 | 1.0 |
| 270 | 1.2 | 3.9 | 8.0 |
| 265 | 2.1 | 7.0 | 12.1 |
| 260 | 3.4 | 9.7 | 15.1 |
| 255 | 4.4 | 11.6 | 17.1 |
| 250 | 5.4 | 13.4 | 19.0 |
| 245 | 6.5 | 15.1 | 20.9 |
| 240 | 7.6 | 16.8 | 22.9 |
| 235 | 8.9 | 18.6 | 25.1 |
| 230 | 10.4 | 20.6 | 27.4 |
| 225 | 11.9 | 22.9 | 30.3 |
| 220 | 13.8 | 25.6 | 33.7 |

**2.1.3**

| | Difference | | |
|---|---|---|---|
| **BCL** | 0-1 cm | 1-2 cm | 2-3 cm |
| 280 | 3.0 | 2.1 | 2.0 |
| 275 | 18.6 | 17.3 | 15.0 |
| 270 | 19.6 | 15.7 | 10.2 |
| 265 | 20.9 | 14.9 | 8.1 |
| 260 | 22.6 | 14.8 | 7.3 |
| 255 | 25.2 | 16.2 | 7.9 |
| 250 | 29.1 | 18.6 | 9.4 |
| 245 | 34.3 | 22.5 | 12.1 |
| 240 | 41.4 | 28.0 | 15.7 |
| 235 | 49.6 | 34.7 | 20.4 |
| 230 | 58.8 | 42.1 | 25.7 |
| 225 | 68.1 | 49.3 | 31.0 |
| 220 | 76.9 | 56.0 | 35.3 |

**Spatially Averaged Alternans Results (Default Setting, 4 cm)**

**2.1.4**

| | Control-OFF | | | |
|---|---|---|---|---|
| **BCL** | 0-1 cm | 1-2 cm | 2-3 cm | 3-4 cm |
| 280 | 0.0 | 0.0 | 0.0 | 0.0 |
| 275 | 17.7 | 15.2 | 11.1 | 7.5 |
| 270 | 20.7 | 19.6 | 18.4 | 17.2 |
| 265 | 23.0 | 22.1 | 20.8 | 19.4 |
| 260 | 26.0 | 24.7 | 23.3 | 21.4 |
| 255 | 29.6 | 28.0 | 26.1 | 23.8 |
| 250 | 34.5 | 32.2 | 29.6 | 26.7 |
| 245 | 40.7 | 37.8 | 34.2 | 30.3 |
| 240 | 48.7 | 44.9 | 40.0 | 34.8 |
| 235 | 58.4 | 53.3 | 46.9 | 40.2 |
| 230 | 69.1 | 62.7 | 54.6 | 46.4 |
| 225 | 79.9 | 72.2 | 62.7 | 52.9 |
| 220 | 90.5 | 81.3 | 70.4 | 59.3 |

**2.1.5**

| | Control-ON | | | |
|---|---|---|---|---|
| **BCL** | 0-1 cm | 1-2 cm | 2-3 cm | 3-4 cm |
| 280 | 0.0 | 0.0 | 0.0 | 0.0 |
| 275 | 0.0 | 1.2 | 3.0 | 5.8 |
| 270 | 1.3 | 4.1 | 8.8 | 12.4 |
| 265 | 2.3 | 7.7 | 13.8 | 16.6 |
| 260 | 3.5 | 10.4 | 16.7 | 18.9 |
| 255 | 4.6 | 12.3 | 18.8 | 20.9 |
| 250 | 5.7 | 14.2 | 21.0 | 23.0 |
| 245 | 6.8 | 16.0 | 23.3 | 25.0 |
| 240 | 8.1 | 17.9 | 25.7 | 27.6 |
| 235 | 9.4 | 20.0 | 28.5 | 30.6 |
| 230 | 10.9 | 22.4 | 32.0 | 34.0 |
| 225 | 12.8 | 25.2 | 36.1 | 38.8 |
| 220 | 15.1 | 28.6 | 40.9 | 44.0 |

**2.1.6**

| | Difference | | | |
|---|---|---|---|---|
| **BCL** | 0-1 cm | 1-2 cm | 2-3 cm | 3-4 cm |
| 280 | 0.0 | 0.0 | 0.0 | 0.0 |
| 275 | 17.7 | 14.0 | 8.1 | 1.7 |
| 270 | 19.5 | 15.5 | 9.6 | 4.7 |
| 265 | 20.7 | 14.4 | 7.0 | 2.8 |
| 260 | 22.5 | 14.3 | 6.6 | 2.5 |
| 255 | 25.1 | 15.7 | 7.3 | 2.8 |
| 250 | 28.8 | 18.1 | 8.6 | 3.7 |
| 245 | 33.9 | 21.8 | 10.9 | 5.3 |
| 240 | 40.7 | 27.0 | 14.3 | 7.2 |
| 235 | 49.1 | 33.4 | 18.4 | 9.6 |
| 230 | 58.2 | 40.3 | 22.7 | 12.4 |
| 225 | 67.1 | 46.9 | 26.6 | 14.1 |
| 220 | 75.4 | 52.7 | 29.5 | 15.3 |

**Spatially Averaged Alternans Results (Default Setting, 5 cm)**

**2.1.7**

| | Control-OFF | | | | |
|---|---|---|---|---|---|
| **BCL** | 0-1 cm | 1-2 cm | 2-3 cm | 3-4 cm | 4-5 cm |
| 280 | 0.0 | 0.0 | 0.0 | 0.0 | 0.0 |
| 275 | 17.5 | 14.8 | 10.1 | 3.4 | 3.5 |
| 270 | 20.6 | 19.1 | 15.8 | 8.7 | 2.2 |
| 265 | 23.0 | 22.1 | 21.0 | 19.9 | 18.6 |
| 260 | 26.0 | 24.6 | 23.4 | 22.4 | 20.7 |
| 255 | 29.6 | 28.0 | 26.3 | 24.8 | 22.9 |
| 250 | 34.5 | 32.2 | 29.8 | 27.8 | 25.4 |
| 245 | 40.5 | 37.2 | 31.9 | 21.5 | 5.4 |
| 240 | 47.6 | 41.6 | 28.2 | 7.5 | 18.9 |
| 235 | 56.7 | 48.1 | 28.9 | 8.6 | 26.9 |
| 230 | 66.6 | 55.2 | 29.2 | 12.3 | 36.4 |
| 225 | 76.9 | 62.1 | 28.3 | 19.1 | 48.1 |
| 220 | 86.7 | 68.1 | 25.6 | 29.5 | 61.4 |

**2.1.8**

| | Control-ON | | | | |
|---|---|---|---|---|---|
| **BCL** | 0-1 cm | 1-2 cm | 2-3 cm | 3-4 cm | 4-5 cm |
| 280 | 0.0 | 0.0 | 0.0 | 0.0 | 0.0 |
| 275 | 0.0 | 3.8 | 5.2 | 7.5 | 10.1 |
| 270 | 1.3 | 4.3 | 9.2 | 13.4 | 15.0 |
| 265 | 2.3 | 7.8 | 14.1 | 17.5 | 18.0 |
| 260 | 3.5 | 10.4 | 17.0 | 19.8 | 19.7 |
| 255 | 7.7 | 15.1 | 21.8 | 24.6 | 24.1 |
| 250 | 8.5 | 16.9 | 23.9 | 26.7 | 26.0 |
| 245 | 6.8 | 16.0 | 23.7 | 26.7 | 25.7 |
| 240 | 8.1 | 17.9 | 26.2 | 29.5 | 28.5 |
| 235 | 9.4 | 20.1 | 29.3 | 32.9 | 31.7 |
| 230 | 13.9 | 25.3 | 35.4 | 39.7 | 38.0 |
| 225 | 13.4 | 25.6 | 35.9 | 40.4 | 38.7 |
| 220 | 15.3 | 29.4 | 40.2 | 45.4 | 43.2 |

**2.1.9**

| | Difference | | | | |
|---|---|---|---|---|---|
| **BCL** | 0-1 cm | 1-2 cm | 2-3 cm | 3-4 cm | 4-5 cm |
| 280 | 0.0 | 0.0 | 0.0 | 0.0 | -0.0 |
| 275 | 17.4 | 11.1 | 4.9 | -4.1 | -6.6 |
| 270 | 19.3 | 14.8 | 6.6 | -4.7 | -12.8 |
| 265 | 20.7 | 14.3 | 7.0 | 2.4 | 0.6 |
| 260 | 22.4 | 14.2 | 6.4 | 2.6 | 1.0 |
| 255 | 22.0 | 12.9 | 4.6 | 0.2 | -1.2 |
| 250 | 26.0 | 15.3 | 6.0 | 1.2 | -0.5 |
| 245 | 33.8 | 21.2 | 8.2 | -5.2 | 20.3 |
| 240 | 39.5 | 23.7 | 2.0 | -22.1 | -9.6 |
| 235 | 47.3 | 28.0 | -0.4 | -24.3 | -4.9 |
| 230 | 52.7 | 29.9 | -6.1 | -27.4 | -1.6 |
| 225 | 63.5 | 36.5 | -7.6 | -21.4 | 9.4 |
| 220 | 71.4 | 38.7 | -14.7 | -15.9 | 18.2 |

**Table 2.1 Spatially averaged alternans magnitude ($A_{M,S}$) results under default parameter settings for different 1-D cable lengths paced at varying BCLs.** 2.1.1-2.1.3 $A_{M,S}$ values derived from subregions of L = 3 cm cable simulations (in increments of 1.0 cm) during control-off (2.1.1) and control-on (2.1.2) over a range of BCLs (220-280 ms). 2.1.3 is table result of control-off minus control-on results. 2.1.4-2.1.6 – L = 4 cm. 2.1.7-2.1.9 – L = 5 cm. Highlighted arrays indicate instances of discordant alternans. BCL and $A_{M,S}$ values in ms.

concordant alternans was observed during control-on conditions regardless of the control-off spatial dynamics.

The spatially averaged alternans results for the voltage-driven parameter regime are shown in Table 2.2. For each of the three cable lengths tested the onset of large-scale alternans was abrupt during static pacing. In each case, during control-off conditions no alternans were observed at BCL = 330 ms, but a slightly reduced BCL (= 325 ms) yielded $A_{M,S} > 20$ ms at one or more regions along the cable. At each successive pacing cycle length reduction, the magnitude of alternans grows dramatically – when BCL = 310 ms, $A_{M,S} > 80$ ms along the entire length of the cable in each case. The alternans control-on results demonstrate the same abrupt alternans onset characteristics. These observations are likely a result of the increased APD restitution slope that characterizes the voltage-driven parameter regime. In these simulations, only a slight decrease in BCL was needed in order to push the system from stability to instability. Furthermore, the relative degree of APD instability at BCL values beyond the bifurcation point was probably increased (quantifiable using eigenvalue analysis [43]). In terms of spatial alternans control success, the onset of alternans is delayed with control by decreasing amounts as the cable length increases.

The spatially averaged alternans results for the calcium-driven parameter regime are shown in Table 2.3. The effect of alternans control on the spatial dynamics varied from that of the default and voltage-driven parameter regimes. There was an overall higher prevalence of discordant alternans observed during both control-off and control-on conditions, but its occurrence was without any discernable pattern. Control was relatively good at reducing $A_{M,S}$ in the proximal tissue region (0-1 cm) (except for its complete failure at BCL = 155 ms). In general, the effect of control was minimal

## Color Code

| Control Off | |
|---|---|
| (0-10) | |
| (10-20) | |
| (20-30) | |
| (30-40) | |
| (40-50) | |
| (50-60) | |
| (60-70) | |
| (70-80) | |
| (80+) | |

| Control On | |
|---|---|
| (0-10) | |
| (10-20) | |
| (20-30) | |
| (30-40) | |
| (40-50) | |
| (50-60) | |
| (60-70) | |
| (70-80) | |
| (80+) | |

| Control Diff | |
|---|---|
| (0-10) | |
| (10-20) | |
| (20-30) | |
| (30-40) | |
| (40-50) | |
| (50-60) | |
| (60-70) | |
| (70-80) | |
| (80+) | |

| Control Diff | (negative) |
|---|---|
| (0-10) | |
| (10-20) | |
| (20-30) | |
| (30-40) | |
| (40-50) | |
| (50-60) | |
| (60-70) | |
| (70-80) | |
| (80+) | |

**Spatially Averaged Alternans Results (Voltage Driven Setting, 3 cm)**

**2.2.1**

| | Control-OFF | | |
|---|---|---|---|
| BCL | 0-1 cm | 1-2 cm | 2-3 cm |
| 330 | 0.0 | 0.0 | 0.0 |
| 325 | 24.3 | 19.2 | 12.8 |
| 320 | 48.8 | 41.1 | 30.1 |
| 315 | 76.1 | 66.7 | 51.5 |
| 310 | 97.0 | 88.7 | 72.9 |
| 305 | 113.5 | 106.2 | 91.5 |
| 300 | 126.9 | 120.3 | 106.9 |
| 295 | 138.0 | 131.8 | 119.5 |
| 290 | 147.5 | 141.4 | 129.9 |
| 285 | 156.1 | 149.8 | 138.6 |
| 280 | 163.8 | 157.1 | 146.0 |
| 275 | 170.9 | 163.6 | 152.4 |
| 270 | 177.6 | 169.4 | 157.9 |

**2.2.2**

| | Control-ON | | |
|---|---|---|---|
| BCL | 0-1 cm | 1-2 cm | 2-3 cm |
| 330 | 0.0 | 0.0 | 0.0 |
| 325 | 0.0 | 0.0 | 0.0 |
| 320 | 0.0 | 0.0 | 0.0 |
| 315 | 0.0 | 0.0 | 0.0 |
| 310 | 0.0 | 0.0 | 0.0 |
| 305 | 0.0 | 0.4 | 1.0 |
| 300 | 74.1 | 87.1 | 99.6 |
| 295 | 92.2 | 103.4 | 125.6 |
| 290 | 96.0 | 108.4 | 115.3 |
| 285 | 105.3 | 123.9 | 128.3 |
| 280 | 105.0 | 126.4 | 167.8 |
| 275 | 112.4 | 127.3 | 113.5 |
| 270 | 123.9 | 124.7 | 121.9 |

**2.2.3**

| | Difference | | |
|---|---|---|---|
| BCL | 0-1 cm | 1-2 cm | 2-3 cm |
| 330 | 0.0 | 0.0 | 0.0 |
| 325 | 24.3 | 19.2 | 12.8 |
| 320 | 48.8 | 41.1 | 30.1 |
| 315 | 76.1 | 66.7 | 51.5 |
| 310 | 97.0 | 88.7 | 72.9 |
| 305 | 113.5 | 105.9 | 90.5 |
| 300 | 52.8 | 33.1 | 7.3 |
| 295 | 45.9 | 28.3 | 6.1 |
| 290 | 51.5 | 33.0 | 14.5 |
| 285 | 50.7 | 25.8 | 10.3 |
| 280 | 58.9 | 30.7 | 21.7 |
| 275 | 58.5 | 36.3 | 38.9 |
| 270 | 53.7 | 44.7 | 35.9 |

**Spatially Averaged Alternans Results (Voltage Driven Setting, 4 cm)**

**2.2.4**

| | Control-OFF | | | |
|---|---|---|---|---|
| BCL | 0-1 cm | 1-2 cm | 2-3 cm | 3-4 cm |
| 330 | 0.0 | 0.0 | 0.0 | 0.0 |
| 325 | 23.4 | 19.3 | 13.3 | 7.6 |
| 320 | 52.0 | 46.0 | 36.8 | 26.6 |
| 315 | 76.7 | 70.0 | 59.5 | 45.9 |
| 310 | 97.2 | 91.4 | 81.9 | 67.2 |
| 305 | 113.7 | 108.2 | 100.2 | 86.5 |
| 300 | 127.0 | 121.8 | 114.7 | 102.3 |
| 295 | 138.1 | 133.0 | 126.5 | 115.2 |
| 290 | 147.5 | 142.4 | 136.2 | 125.7 |
| 285 | 156.1 | 150.6 | 144.6 | 134.4 |
| 280 | 163.8 | 157.8 | 151.7 | 141.8 |
| 275 | 170.9 | 164.2 | 157.8 | 147.9 |
| 270 | 177.6 | 170.0 | 163.0 | 153.0 |

**2.2.5**

| | Control-ON | | | |
|---|---|---|---|---|
| BCL | 0-1 cm | 1-2 cm | 2-3 cm | 3-4 cm |
| 330 | 0.0 | 0.0 | 0.0 | 0.0 |
| 325 | 0.0 | 0.0 | 0.0 | 0.0 |
| 320 | 0.0 | 0.0 | 0.0 | 0.0 |
| 315 | 0.0 | 0.0 | 0.0 | 0.0 |
| 310 | 36.7 | 50.8 | 65.0 | 68.4 |
| 305 | 64.4 | 80.6 | 101.0 | 110.1 |
| 300 | 77.6 | 92.5 | 114.3 | 130.0 |
| 295 | 94.3 | 107.3 | 139.9 | 102.5 |
| 290 | 97.9 | 117.7 | 122.1 | 79.8 |
| 285 | 105.1 | 129.3 | 114.4 | 83.9 |
| 280 | 107.1 | 143.9 | 91.1 | 79.5 |
| 275 | 114.5 | 127.2 | 136.1 | 134.9 |
| 270 | 123.7 | 125.8 | 127.6 | 131.6 |

**2.2.6**

| | Difference | | | |
|---|---|---|---|---|
| BCL | 0-1 cm | 1-2 cm | 2-3 cm | 3-4 cm |
| 330 | 0.0 | 0.0 | 0.0 | 0.0 |
| 325 | 23.4 | 19.3 | 13.3 | 7.6 |
| 320 | 52.0 | 46.0 | 36.8 | 26.6 |
| 315 | 76.7 | 70.0 | 59.5 | 45.9 |
| 310 | 60.6 | 40.6 | 16.9 | 1.2 |
| 305 | 49.3 | 27.6 | 0.9 | 23.7 |
| 300 | 49.3 | 29.3 | 0.4 | 27.7 |
| 295 | 43.8 | 25.7 | 13.4 | 12.7 |
| 290 | 49.6 | 24.7 | 14.1 | 45.9 |
| 285 | 51.0 | 21.3 | 30.2 | 50.5 |
| 280 | 56.7 | 13.9 | 60.6 | 62.3 |
| 275 | 56.3 | 37.1 | 21.7 | 13.1 |
| 270 | 53.9 | 44.2 | 35.5 | 21.5 |

**Spatially Averaged Alternans Results (Voltage Driven Setting, 5 cm)**

**2.2.7**

| | Control-OFF | | | | |
|---|---|---|---|---|---|
| BCL | 0-1 cm | 1-2 cm | 2-3 cm | 3-4 cm | 4-5 cm |
| 330 | 0.0 | 0.0 | 0.0 | 0.0 | 0.0 |
| 325 | 28.8 | 23.5 | 15.9 | 7.9 | 2.1 |
| 320 | 51.9 | 46.2 | 39.3 | 31.0 | 21.6 |
| 315 | 76.8 | 70.6 | 62.9 | 53.7 | 41.5 |
| 310 | 97.2 | 91.6 | 84.9 | 76.4 | 62.5 |
| 305 | 113.7 | 108.4 | 102.4 | 95.4 | 82.0 |
| 300 | 127.0 | 121.9 | 116.4 | 110.5 | 98.1 |
| 295 | 138.1 | 133.0 | 127.9 | 122.5 | 111.3 |
| 290 | 147.5 | 142.5 | 137.4 | 132.4 | 121.9 |
| 285 | 156.1 | 150.6 | 145.5 | 140.7 | 130.7 |
| 280 | 163.8 | 157.8 | 152.5 | 147.6 | 137.9 |
| 275 | 170.9 | 164.2 | 158.6 | 153.5 | 143.9 |
| 270 | 177.6 | 170.0 | 163.7 | 158.4 | 148.8 |

**2.2.8**

| | Control-ON | | | | |
|---|---|---|---|---|---|
| BCL | 0-1 cm | 1-2 cm | 2-3 cm | 3-4 cm | 4-5 cm |
| 330 | 0.0 | 0.0 | 0.0 | 0.0 | 0.0 |
| 325 | 0.0 | 0.0 | 0.0 | 0.0 | 0.0 |
| 320 | 0.0 | 0.0 | 0.0 | 0.0 | 0.0 |
| 315 | 14.1 | 26.1 | 40.3 | 45.8 | 41.0 |
| 310 | 38.3 | 54.9 | 74.3 | 83.0 | 83.9 |
| 305 | 64.9 | 78.8 | 100.3 | 114.9 | 113.2 |
| 300 | 83.5 | 98.1 | 119.4 | 134.7 | 114.8 |
| 295 | 91.6 | 106.3 | 130.8 | 109.4 | 74.2 |
| 290 | 102.0 | 123.2 | 126.9 | 91.4 | 63.2 |
| 285 | 106.7 | 127.8 | 119.4 | 72.5 | 57.4 |
| 280 | 106.3 | 135.1 | 98.7 | 90.9 | 90.4 |
| 275 | 113.1 | 127.5 | 137.5 | 139.3 | 161.0 |
| 270 | 121.2 | 126.1 | 129.6 | 162.8 | 121.8 |

**2.2.9**

| | Difference | | | | |
|---|---|---|---|---|---|
| BCL | 0-1 cm | 1-2 cm | 2-3 cm | 3-4 cm | 4-5 cm |
| 330 | 0.0 | 0.0 | 0.0 | 0.0 | 0.0 |
| 325 | 28.8 | 23.5 | 15.9 | 7.9 | 2.1 |
| 320 | 51.9 | 46.2 | 39.3 | 31.0 | 21.6 |
| 315 | 62.7 | 44.5 | 22.7 | 7.9 | 0.5 |
| 310 | 59.0 | 36.8 | 10.5 | 6.5 | 21.4 |
| 305 | 48.8 | 29.6 | 2.1 | 19.5 | 31.2 |
| 300 | 43.4 | 23.8 | 3.0 | 24.3 | 16.7 |
| 295 | 46.5 | 26.8 | 3.0 | 13.1 | 37.1 |
| 290 | 45.5 | 19.3 | 10.5 | 41.0 | 58.7 |
| 285 | 49.4 | 22.9 | 26.1 | 68.2 | 73.3 |
| 280 | 57.5 | 22.7 | 53.9 | 56.7 | 47.6 |
| 275 | 57.8 | 36.8 | 21.0 | 14.2 | 17.1 |
| 270 | 56.4 | 44.0 | 34.1 | 4.3 | 26.9 |

**Table 2.2 Spatially averaged alternans magnitude ($A_{M,S}$) results under voltage driven parameter settings for different 1-D cable lengths paced at varying BCLs.** 2.1.1-2.1.3 $A_{M,S}$ values derived from subregions of L = 3 cm cable simulations (in increments of 1.0 cm) during control-off (2.1.1) and control-on (2.1.2) over a range of BCLs (220-280 ms). 2.1.3 is table result of control-off minus control-on results. 2.1.4-2.1.6 – L = 4 cm. 2.1.7-2.1.9 – L = 5 cm. BCL and $A_{M,S}$ values in ms.

## Color Code

| Control Off | |
|---|---|
| (0-10) | |
| (10-20) | |
| (20-30) | |
| (30-40) | |
| (40-50) | |
| (50-60) | |
| (60-70) | |
| (70-80) | |
| (80+) | |

| Control On | |
|---|---|
| (0-10) | |
| (10-20) | |
| (20-30) | |
| (30-40) | |
| (40-50) | |
| (50-60) | |
| (60-70) | |
| (70-80) | |
| (80+) | |

| Control Diff | |
|---|---|
| (0-10) | |
| (10-20) | |
| (20-30) | |
| (30-40) | |
| (40-50) | |
| (50-60) | |
| (60-70) | |
| (70-80) | |
| (80+) | |

| Control Diff | (negative) |
|---|---|
| (0-10) | |
| (10-20) | |
| (20-30) | |
| (30-40) | |
| (40-50) | |
| (50-60) | |
| (60-70) | |
| (70-80) | |
| (80+) | |

### Spatially Averaged Alternans Results (Calcium Driven Setting, 3 cm)

**2.3.1**

| | Control-OFF | | |
|---|---|---|---|
| BCL | 0-1 cm | 1-2 cm | 2-3 cm |
| 220 | 2.0 | 1.8 | 1.0 |
| 215 | 3.3 | 2.5 | 3.5 |
| 210 | 3.0 | 2.8 | 0.9 |
| 205 | 0.0 | 0.9 | 3.7 |
| 200 | 5.6 | 5.0 | 4.2 |
| 195 | 7.5 | 5.7 | 1.4 |
| 190 | 10.4 | 5.5 | 2.9 |
| 185 | 11.4 | 3.6 | 5.7 |
| 180 | 8.6 | 2.9 | 8.2 |
| 175 | 8.7 | 3.5 | 9.9 |
| 170 | 27.5 | 19.8 | 8.8 |
| 165 | 33.7 | 20.4 | 3.9 |
| 160 | 42.6 | 23.8 | 4.7 |
| 155 | 49.3 | 22.4 | 9.2 |

**2.3.2**

| | Control-ON | | |
|---|---|---|---|
| BCL | 0-1 cm | 1-2 cm | 2-3 cm |
| 220 | 1.0 | 1.6 | 1.2 |
| 215 | 2.3 | 1.5 | 3.0 |
| 210 | 2.0 | 1.8 | 1.2 |
| 205 | 0.0 | 0.9 | 3.7 |
| 200 | 3.4 | 3.0 | 2.4 |
| 195 | 3.8 | 2.6 | 1.6 |
| 190 | 4.7 | 1.9 | 6.5 |
| 185 | 4.0 | 3.7 | 11.0 |
| 180 | 1.9 | 6.5 | 12.4 |
| 175 | 1.8 | 8.6 | 14.0 |
| 170 | 5.7 | 4.3 | 1.8 |
| 165 | 1.8 | 7.4 | 13.9 |
| 160 | 0.5 | 0.1 | 4.1 |
| | 43.4 | 41.8 | 46.0 |

**2.3.3**

| | Difference | | |
|---|---|---|---|
| BCL | 0-1 cm | 1-2 cm | 2-3 cm |
| 220 | 1.0 | 0.2 | -0.2 |
| 215 | 1.0 | 1.0 | 0.5 |
| 210 | 1.0 | 1.0 | -0.3 |
| 205 | 0.0 | 0.0 | 0.0 |
| 200 | 2.2 | 2.0 | 1.9 |
| 195 | 3.7 | 3.1 | -0.2 |
| 190 | 5.7 | 3.5 | -3.7 |
| 185 | 7.4 | -0.1 | -5.3 |
| 180 | 6.7 | -3.6 | -4.2 |
| 175 | 6.9 | -5.1 | -4.0 |
| 170 | 21.8 | 15.5 | 7.0 |
| 165 | 31.9 | 13.0 | -10.0 |
| 160 | 42.1 | 23.7 | 0.6 |
| 155 | 5.9 | -19.4 | -36.7 |

### Spatially Averaged Alternans Results (Calcium Driven Setting, 4 cm)

**2.3.4**

| | Control-OFF | | | |
|---|---|---|---|---|
| BCL | 0-1 cm | 1-2 cm | 2-3 cm | 3-4 cm |
| 220 | 2.0 | 1.4 | 3.0 | 5.0 |
| 215 | 3.6 | 3.2 | 3.6 | 1.2 |
| 210 | 3.5 | 2.3 | 2.9 | 5.1 |
| 205 | 1.0 | 2.6 | 5.4 | 3.3 |
| 200 | 5.6 | 5.0 | 2.1 | 4.5 |
| 195 | 6.7 | 2.9 | 4.7 | 7.8 |
| 190 | 8.5 | 2.8 | 6.9 | 9.8 |
| 185 | 9.8 | 3.0 | 8.4 | 10.9 |
| 180 | 6.5 | 3.5 | 10.2 | 12.0 |
| 175 | 3.4 | 9.3 | 12.6 | 12.3 |
| 170 | 22.3 | 10.3 | 7.4 | 16.0 |
| 165 | 30.2 | 14.5 | 8.8 | 20.7 |
| 160 | 36.3 | 13.8 | 16.0 | 29.7 |
| 155 | 41.1 | 13.0 | 25.7 | 40.2 |

**2.3.5**

| | Control-ON | | | |
|---|---|---|---|---|
| BCL | 0-1 cm | 1-2 cm | 2-3 cm | 3-4 cm |
| 220 | 1.0 | 0.8 | 3.4 | 5.0 |
| 215 | 2.6 | 2.1 | 2.8 | 1.8 |
| 210 | 2.3 | 1.4 | 3.9 | 6.0 |
| 205 | 1.0 | 2.3 | 4.9 | 2.8 |
| 200 | 3.3 | 2.8 | 1.8 | 6.1 |
| 195 | 3.5 | 1.6 | 7.2 | 10.0 |
| 190 | 3.7 | 3.1 | 10.5 | 12.9 |
| 185 | 3.2 | 5.3 | 12.9 | 14.0 |
| 180 | 1.7 | 7.3 | 13.5 | 14.2 |
| 175 | 2.3 | 8.5 | 11.8 | 12.0 |
| 170 | 3.2 | 4.5 | 15.5 | 16.8 |
| 165 | 3.9 | 10.9 | 13.9 | 13.4 |
| 160 | 0.7 | 5.4 | 16.4 | 19.5 |
| | 43.2 | 41.1 | 47.0 | 47.8 |

**2.3.6**

| | Difference | | | |
|---|---|---|---|---|
| BCL | 0-1 cm | 1-2 cm | 2-3 cm | 3-4 cm |
| 220 | 1.0 | 0.6 | -0.4 | 0.0 |
| 215 | 1.0 | 1.1 | 0.7 | -0.6 |
| 210 | 1.1 | 0.9 | -1.0 | -0.9 |
| 205 | 0.0 | 0.4 | 0.5 | 0.5 |
| 200 | 2.3 | 2.1 | 0.3 | -1.6 |
| 195 | 3.2 | 1.4 | -2.6 | -2.2 |
| 190 | 4.8 | -0.3 | -3.6 | -3.2 |
| 185 | 6.5 | -2.3 | -4.5 | -3.1 |
| 180 | 4.8 | -3.9 | -3.3 | -2.2 |
| 175 | 1.2 | 0.8 | 0.8 | 0.3 |
| 170 | 19.2 | 5.8 | -8.1 | -0.8 |
| 165 | 26.3 | 3.6 | -5.1 | 7.4 |
| 160 | 35.6 | 8.5 | -0.4 | 10.3 |
| 155 | -2.1 | -28.1 | -21.3 | -7.6 |

### Spatially Averaged Alternans Results (Calcium Driven Setting, 5 cm)

**2.3.7**

| | Control-OFF | | | | |
|---|---|---|---|---|---|
| BCL | 0-1 cm | 1-2 cm | 2-3 cm | 3-4 cm | 4-5 cm |
| 220 | 2.0 | 1.3 | 3.5 | 5.6 | 3.0 |
| 215 | 3.6 | 3.3 | 2.7 | 3.3 | 5.0 |
| 210 | 3.4 | 1.9 | 3.7 | 6.2 | 4.3 |
| 205 | 1.3 | 2.5 | 4.3 | 2.2 | 5.7 |
| 200 | 5.6 | 4.7 | 2.1 | 6.5 | 8.0 |
| 195 | 6.7 | 3.0 | 4.9 | 8.7 | 8.1 |
| 190 | 7.7 | 2.6 | 6.7 | 7.8 | 5.1 |
| 185 | 10.6 | 3.1 | 5.1 | 1.8 | 2.5 |
| 180 | 8.7 | 1.8 | 2.1 | 8.1 | 10.0 |
| 175 | 12.9 | 9.3 | 10.0 | 11.0 | 10.1 |
| 170 | 20.8 | 8.0 | 9.6 | 18.6 | 19.1 |
| 165 | 29.5 | 13.4 | 10.3 | 24.6 | 26.1 |
| 160 | 35.5 | 13.1 | 17.4 | 33.7 | 33.6 |
| 155 | 40.5 | 12.6 | 26.6 | 43.4 | 40.4 |

**2.3.8**

| | Control-ON | | | | |
|---|---|---|---|---|---|
| BCL | 0-1 cm | 1-2 cm | 2-3 cm | 3-4 cm | 4-5 cm |
| 220 | 1.0 | 0.8 | 3.9 | 5.8 | 3.4 |
| 215 | 2.6 | 2.1 | 1.9 | 4.2 | 6.0 |
| 210 | 4.6 | 3.5 | 7.0 | 9.6 | 7.4 |
| 205 | 1.0 | 2.1 | 3.7 | 2.5 | 5.9 |
| 200 | 3.3 | 2.3 | 2.6 | 8.3 | 9.0 |
| 195 | 5.6 | 3.8 | 9.6 | 12.9 | 12.2 |
| 190 | 3.3 | 3.0 | 10.0 | 10.6 | 7.3 |
| 185 | 3.7 | 4.3 | 9.7 | 4.3 | 0.1 |
| 180 | 3.9 | 6.0 | 4.7 | 7.5 | 10.5 |
| 175 | 4.5 | 3.3 | 6.3 | 8.6 | 9.0 |
| 170 | 6.4 | 9.4 | 17.3 | 19.7 | 14.9 |
| 165 | 6.5 | 13.6 | 16.0 | 14.6 | 11.8 |
| 160 | 6.7 | 10.9 | 13.0 | 11.8 | 9.4 |
| | 39.3 | 35.4 | 40.2 | 42.6 | 41.2 |

**2.3.9**

| | Difference | | | | |
|---|---|---|---|---|---|
| BCL | 0-1 cm | 1-2 cm | 2-3 cm | 3-4 cm | 4-5 cm |
| 220 | 1.0 | 0.5 | -0.4 | -0.2 | -0.4 |
| 215 | 1.0 | 1.1 | 0.8 | -0.9 | -1.0 |
| 210 | -1.2 | -1.6 | -3.2 | -3.4 | -3.1 |
| 205 | 0.3 | 0.4 | 0.7 | -0.2 | -0.2 |
| 200 | 2.3 | 2.4 | -0.5 | -1.7 | -1.0 |
| 195 | 1.0 | -0.9 | -4.7 | -4.2 | -4.1 |
| 190 | 4.5 | -0.4 | -3.3 | -2.8 | -2.1 |
| 185 | 6.9 | -1.2 | -4.6 | -2.5 | 2.3 |
| 180 | 4.8 | -4.3 | -2.5 | 0.6 | -0.5 |
| 175 | 8.4 | 6.0 | 3.6 | 2.4 | 1.0 |
| 170 | 14.4 | -1.4 | -7.7 | -1.1 | 4.2 |
| 165 | 23.0 | -0.2 | -5.7 | 10.1 | 14.3 |
| 160 | 28.8 | 2.2 | 4.4 | 21.9 | 24.3 |
| 155 | 1.3 | -22.8 | -13.7 | 0.8 | -0.8 |

**Table 2.3 Spatially averaged alternans magnitude ($A_{M,S}$) results under calcium driven parameter settings for different 1-D cable lengths paced at varying BCLs.** 2.1.1-2.1.3 $A_{M,S}$ values derived from subregions of L = 3 cm cable simulations(in increments of 1.0 cm) during control-off (2.1.1) and control-on (2.1.2) over a range of BCLs (220-280 ms). 2.1.3 is table result of control-off minus control-on results. 2.1.4-2.1.6 – L = 4 cm. 2.1.7-2.1.9 – L = 5 cm. Highlighted arrays indicate instances of discordant alternans. BCL and $A_{M,S}$ values in ms.

on the overall alternans magnitude along the length of the cable (see "difference" Tables 2.3.3, 2.3.6, and 2.3.9). This can be attributed to the fact that during calcium-driven alternans cell coupling plays much less of a role in determining alternans dynamics. As a result, the spatial effect of single-site control is likely to be less than during default and voltage-driven parameter settings.

### *2.3.5 Spatial dispersion*

Cases of discordant alternans behavior are of particular importance given the recent attention within the cardiac electrodynamics community concerning the genesis, dynamics, and general characteristics of discordant alternans [13-15, 24, 48, 49]. Instances of discordant alternans are usually associated with an increase in repolarization and/or APD gradients (dispersion), which can be quantified by calculating the variance in APD values (or relative repolarization times) within a chosen region of space. The likely mechanism by which alternans promotes unidirectional block and subsequent VF formation involves the creation of steep gradients within the tissue, so a more comprehensive understanding of conduction block can result from a better understanding of discordant alternans.

For our purposes, dispersion was calculated as follows:

$$\sigma^2 = \left( \frac{1}{N} \sum_{i=1}^{N} \left( APD_i - \langle APD \rangle \right)^2 \right) / Length$$

where $N$ is the total number of simulated cable cells and $\langle APD \rangle$ is the spatially averaged value of APD. Variance in APD was normalized to the cable length ("Length," measured in cm) to yield dispersion values (i.e., $\sigma^2$ = variance/cable length in cm).

Fig. 2.5 shows the APD profiles for successive beat pairs, $AP_n$ (red) and $AP_{n+1}$ (blue) (representative $AP_n/AP_{n+1}$ pairs chosen from the set of steady-state action potentials) produced under default parameter settings (L = 5 cm, BCL = 240 ms). In the left plot, the results during static pacing illustrate discordant alternans and the variance in APD of both action potentials yield dispersion values for each ($\sigma^2$-blue ≈ 32 $ms^2/cm$, $\sigma^2$-red ≈ 33 $ms^2/cm$). In the right plot, the results during the application of control illustrate that in converting the spatial dynamics to concordant alternans, the resulting dispersion values are much less ($\sigma^2$-blue ≈ 1.5 $ms^2/cm$, $\sigma^2$-red ≈ 6.9 $ms^2/cm$).

The APD dispersion results derived from simulations under default parameter settings (L = 3, 4, and 5 cm; BCL = 240 and 260 ms) are shown in Fig. 2.6. Only in the case of discordant to concordant transition (L = 5 cm, BCL = 240 ms – see Table 2.1) did the application of control result in an overall smaller dispersion. In all of the other examples, the maximum dispersion value increased during control-on. This result is due to the spatially attenuated nature of control that is observed during most control-on cases.

## 2.4 Discussion

Previous studies of alternans control have been limited to Purkinje fibers, [34, 36], and though informative, a better understanding of alternans control dynamics in the more clinically relevant ventricular tissue is needed. In this study, we investigated the effect of static pacing and single-site control applied to the proximal end of simulated 1-D cables that implemented the SSK ventricular cell model. Control was studied under three different parameter regimes corresponding to voltage-driven

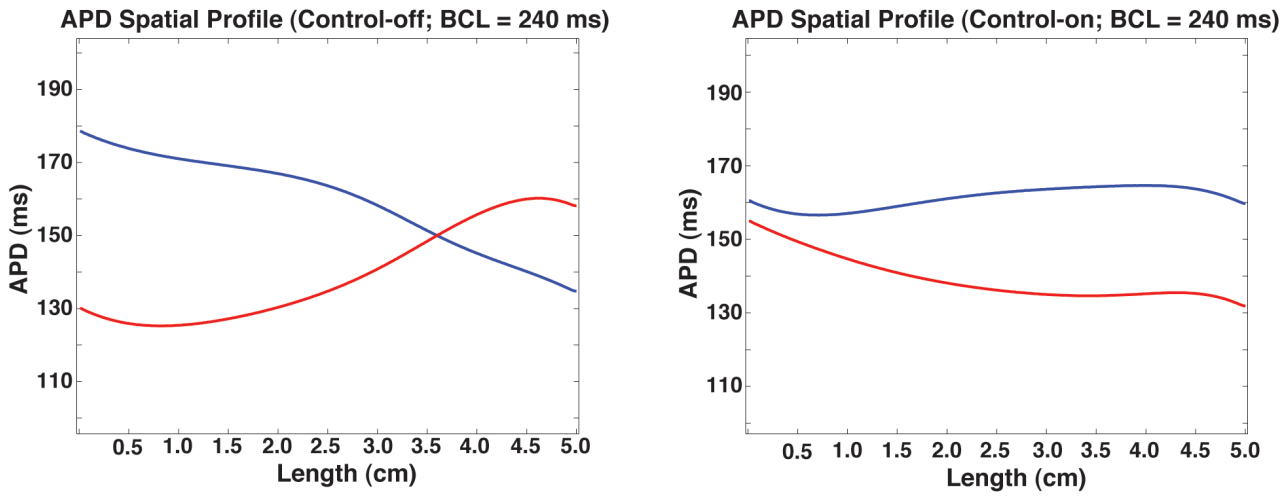


**Figure 2.5 Control-off:discordant → control-on:concordant APD spatial profile example.** APD profile for successive beats ($AP_n$-red, $AP_{n+1}$-blue) during control-off and control-on scenarios (default setting; L = 5 cm; BCL = 240 ms). Discordant alternans observed during control-off (left-hand side); concordant alternans observed during control-on (right-hand side). Resulting dispersions: control-off: $AP_1$ = 32 $ms^2$/cm, $AP_2$ = 33 $ms^2$/cm; control-on: $AP_1$ = 1.5 $ms^2$/cm, $AP_2$ = 6.9 $ms^2$/cm.

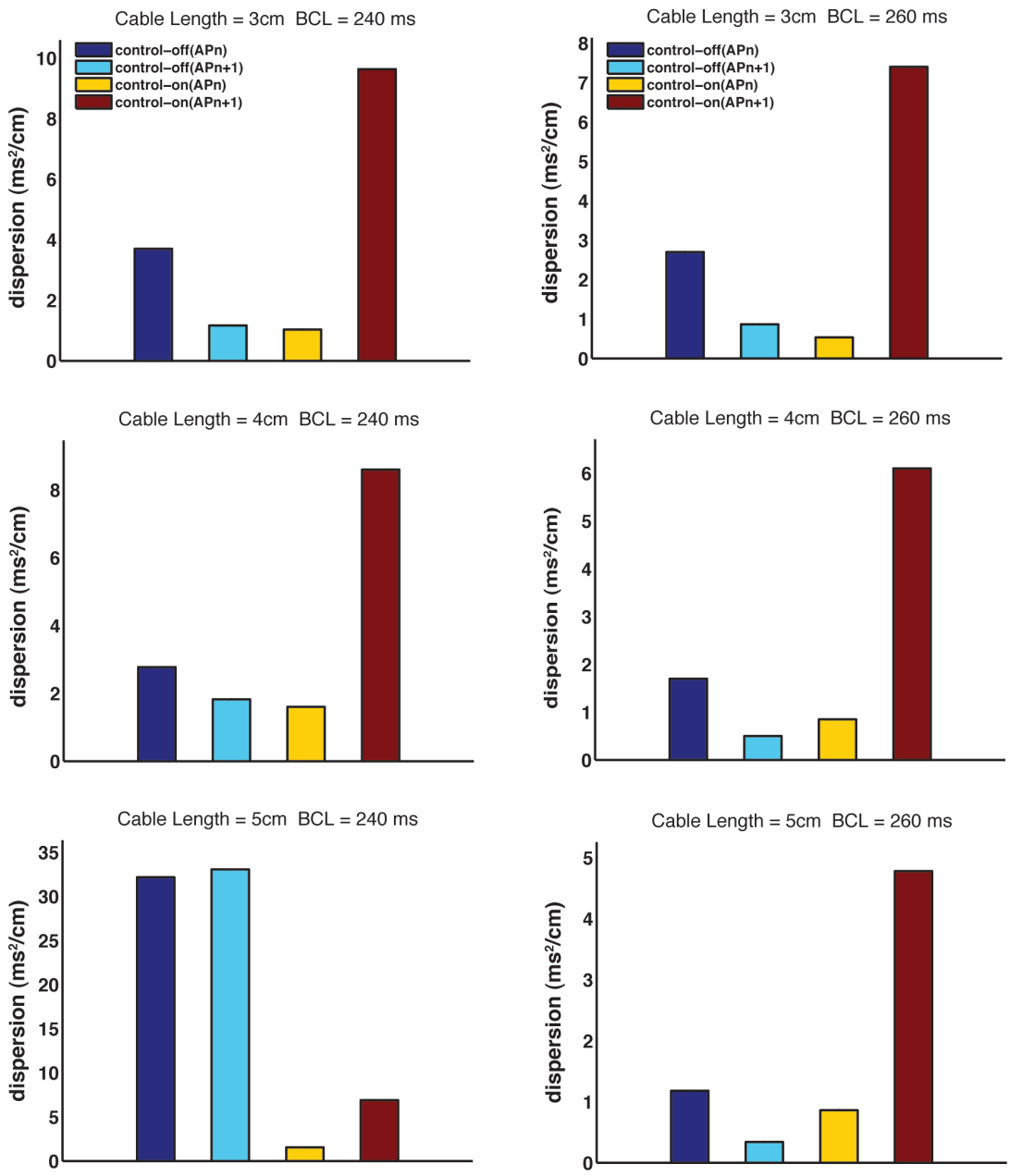


**Figure 2.6 Control-off:control-on APD spatial dispersion.** Control-off and control-on APD dispersion values ($\sigma^2$) at BCL = 240 and 260 ms (default setting). Dispersion for $AP_n$ and $AP_{n+1}$ at L = 3 cm, 4 cm, and 5 cm (A, B, and C, respectively).

alternans, calcium-driven alternans, and a hybrid (default) parameter setting. Compared with static pacing, at its best, control delayed the onset of alternans by only a short period (< 20 ms) in sufficiently long cable lengths (L > 3 cm). In most cases control-induced reduction in alternans magnitude was greatest for regions of tissue that were most proximal to the control site (primarily for default and voltage-driven scenarios) – in agreement with the previously published Purkinje fiber studies.

Comparing the control results across the different parameter regimes highlights the differences in the effect of control for each case. During the default parameter regime, alternans control was very good at reducing alternans in the proximal region of the tissue even at BCL values that were much beyond the bifurcation point. For L = 3, 4, and 5 cm, at BCL = 275 ms, $A_{M,S}$ > 10 ms for the proximal region of tissue during static pacing and the magnitude of alternans steadily increases as the cycle length decreases (Table 2.1.1, 2.1.4, 2.1.7). During the application of control, however, $A_{M,S}$ < 10 ms for all BCL ≥ 235 ms representing a range of 40 ms where alternans control was effective at eliminating alternans in the proximal region.

For the voltage-driven alternans parameter simulations, in analyzing the control results from the proximal region, one can see that alternans control is not nearly as good at eliminating alternans as it was during the default parameter simulations. When L = 3 cm, proximal region alternans delay is 25 ms (325 ms vs. 300 ms – Table 2.2.1, 2.2.2), but this number decreases to 10 ms when L = 5 cm (325 ms vs. 315 ms). The most remarkable observation during the voltage-driven alternans simulations was the abruptness in large-scale alternans onset. This result, however, is not surprising given the nature of voltage-driven alternans. The dynamics are such that even small changes in BCL can have large changes in the resulting action

potential characteristics. On the other side of the coin, when control is successful at the control point, spatial alternans elimination is often times quite good – the spatial attenuation of alternans control when control is successful tends to be small.

In terms of the calcium-driven alternans parameter simulations, focusing on the longer cable lengths (i.e., L = 4 cm and 5 cm), spatial alternans magnitude worsened in general as a result of control (see "difference" Tables 2.3.3, 2.3.6, and 2.3.9), in part due to the prevalence of discordant alternans. But overall, there was little effect of control on $A_{M,S}$ along the length of the cable, as reflected in the magnitudes of the difference Tables (for the majority of cells, difference < 10 ms). In order to induce large-scale alternans ($A_{M,S}$ > 20 ms) pacing at BCL ≤ 170 ms was needed, and control was effective at eliminating alternans in the proximal region at these pacing rates. However, the spatial results suggest that the elimination of alternans was minimally effective as a function of space.

For the three examples where spatial dispersion was calculated (Fig. 2.6), control reduced $\sigma^2$ as compared with control-off in the cases only where discordant alternans was transformed to concordant alternans (L = 5 cm, BCL = 240 ms). In all of the other examples, the maximum dispersion value increased during the application of control. One can argue that even in these particular cases of a control-induced increase in dispersion, the small-amplitude concordant alternans observed during control is better than the large-amplitude concordant alternans of static-pacing given the tendency for large-scale concordant alternans to transform into large-scale discordant alternans with either a slight decrease in pacing cycle length or a properly timed ectopic beat [24, 49]. More studies, both computational and experimental,

which aim to understand the effects of control on spatial dispersion are needed to further understand this issue.

Based on these results, it appears that the effect of control on the spatial dynamics of alternans is dependent on the underlying nature of the alternans instability. But regardless of the alternans dynamics, spatial efficacy of alternans control was observed to be limited and multiple controllers are likely needed if complete spatial elimination of alternans is to be achieved. The exact nature of multisite control (e.g., optimal spacing, proper feedback values, etc.) will likely depend on the specific type of alternans dynamics present. Future computational studies like the one presented in this Chapter will be needed in the context of multisite control in order to better understand how best to develop control systems capable of clinical application.

CHAPTER 3

# CONTROL OF ACTION POTENTIAL DURACTION ALTERNANS IN CANINE CARDIAC VENTRICULAR TISSUE

## 3.1 Abstract

Cardiac electrical alternans, characterized by a beat-to-beat alternation in action potential waveform, is a naturally occurring phenomenon, which can occur at sufficiently fast pacing rates. Its presence has been putatively linked to the onset of cardiac reentry, which is a precursor to ventricular fibrillation. Previous studies have shown that closed-loop alternans control techniques that apply a succession of externally-administered cycle perturbations at a single site provide limited spatially-extended alternans elimination in sufficiently large cardiac substrates. However, detailed experimental investigations into the spatial dynamics of alternans control have been restricted to Purkinje fiber studies. A complete understanding of alternans control in the more clinically relevant ventricular tissue is needed. In this Chapter, we study the spatial dynamics of alternans and alternans control in arterially perfused canine right ventricular preparations using an optical mapping system capable of high-resolution fluorescence imaging. Specifically, we quantify the spatial efficacy of alternans control along 2.5 cm of tissue, focusing on differences in spatial control between different subregions of tissue. We demonstrate effective control of spatially-extended alternans up to 2.0 cm, with control efficacy attenuating as a function of distance. Our results provide a basis for future investigations into electrode-based control interventions of alternans in cardiac tissue.

Chapter reproduced with permission from *Kanu, U.B., Iravanian, S., Gilmour, R.F. Jr, Christini, D.J. Control of action potential duration alternans in canine cardiac ventricular tissue. IEEE TBME 58(4):894-904*

## 3.2 Introduction

Cardiac repolarization alternans, sometimes referred to as action potential duration (APD) alternans, is an electrical phenomenon corresponding to alternating changes in action potential duration. Clinically, alternans has been closely associated with sudden cardiac death (SCD) and ventricular fibrillation (VF), in particular [4-8]. More importantly, mediated by the spatial dispersion of repolarization, alternans has been shown to be mechanistically linked to the pathogenesis of reentrant wave activity [13]. Spatial manifestations of alternans can be either concordant, during which the beat-to-beat alternations in APD are in-phase at all points in space, or discordant, during which two distinct regions exhibiting relative out-of-phase behavior are present. Spatial differences in APD phase can lead to gradients of repolarization (dispersion) within the myocardium, which if steep enough, can facilitate local conduction block of normal wave propagation [14, 15, 24, 48, 49]. Electrical disruptions of this kind can turn a normally planar wave into a spiral wave [50], and furthermore can break a single spiral wave into multiple wavelets of electrical activity [51], which are thought to underlie ventricular fibrillation.

Because of the putative link between APD alternans and the onset of ventricular fibrillation, it may be beneficial to develop means to terminate and/or prevent alternans in cardiac tissue. Closed-loop feedback mechanisms aimed at controlling a dynamically stable period-2 rhythm (alternans) to an unstable period-1 rhythm (no alternans) using single-site intervention from an external source may be one such option.

Previous studies demonstrating successful alternans control include the

elimination of atrio-ventricular alternans – a type of alternans that shares similar characteristics with APD alternans – in rabbit heart preparations [27, 28] the suppression of APD alternans in small isolated frog heart preparations [30], and control in single myocytes [33]. Despite these successes, however, complete alternans control has so far been limited to these small-scale systems (i.e., single-cell or sufficiently small tissue preparations) that do not allow for spatiotemporal variations in wave-propagation or repolarization dynamics – single-site control of physically larger systems has proven to be more difficult.

Investigations of alternans control in larger systems have been limited chiefly to cardiac Purkinje fibers. In all studies – including *in silico* modeling and analytical theory [34], and *in vitro* experimentation [36] – it was demonstrated that spatiotemporal control of alternans is limited to small distances (≈1 cm, depending on the pacing rate) from the site of electrode intervention. This failure of spatially-extended control stems from the complex spatial and temporal interactions that arise between APD and conduction-velocity restitution dynamics that occur during the rapid pacing of sufficiently large regions of tissue [34].

Still missing, however, is a better understanding of alternans and alternans control dynamics in the more clinically relevant ventricular tissue. In particular, the spatial extent of alternans control in ventricular tissue is needed if more complex methods of alternans suppression (e.g., multisite control) are to be developed for clinical use. Given the results yielded by linear stability analysis of general alternans behavior, which suggests that spatial controllability of alternans is dependent on conduction velocity (CV), one would expect that alternans control would behave differently in ventricular tissue (CV < 100 cm/s [37-39]) as compared with Purkinje

fibers (CV ≈200 cm/s [40]).

More generally, in order to fully characterize spatial controllability within real tissue, detailed quantification and analysis of electrophysiological and/or dynamically-induced properties – including conduction velocity restitution, repolarization heterogeneities, and spatial APD variations – are needed at very fine temporal and spatial resolutions.

Aiming to fill this knowledge void, in this study we investigated alternans and alternans control dynamics in arterially perfused canine right ventricular preparations using a previously developed optical mapping system capable of simultaneous real-time control application and high-resolution voltage data imaging [41].

Utilizing the high-resolution capability of the optical mapping system while subjecting the tissue sample to either static or control-perturbed pacing, we were able to observe and quantify the spatial efficacy of alternans control in our preparations. In addition, we were able to observe and analyze spatial changes in APD and repolarization dynamics resulting from the application of control, adding further insight to our understanding of this problem.

Our quantitative results, derived from six different preparations, paced at varying basic cycle length (BCL) values, show that single-site alternans control, although unable to completely eliminate alternans at each point in the field-of-view (2.5 cm), was able to substantially reduce the spatially averaged alternans magnitude ($A_{M,S}$) within the proximal (0–1 cm) and middle (1–2 cm) regions of tissue in 15/17 and 12/17 control trials, respectively. Although the relative success of control was greater at regions more proximal to the control site – in agreement with previous

alternans control experiments [34, 36] – the extent to which control reduced alternans at distances up to 2.0 cm from the control site warrants optimism in the development of more advanced electrode-based intervention techniques for the management of cardiac alternans.

## 3.3 Methodology

### *3.3.1 Isolated arterially perfused right ventricular preparation*

All experimental procedures were approved by the Institutional Animal Care and Use Committee (IACUC) of the Center for Animal Resources and Education of Cornell University. Hearts used in the experiments were extracted from adult beagle dogs of either sex weighing between 10–30 kg. The dogs were anesthetized using Fatal-Plus (Vortex Pharmaceuticals; 390 mg/mL pentobarbital sodium; 86 mg/kg IV), and their hearts were excised rapidly. The right coronary artery was cannulated using polyethylene tubing and the right atrial and ventricular myocardium were extracted and suspended, endocardial surface facing the camera, in a heated (@ 30°C, in order to more easily induce large-scale alternans) and transparent custom-built tissue chamber. The preparation was superfused and arterially perfused with normal Tyrode's solution for the duration of each experiment. After 15 to 30 minutes of equilibration, the preparation was stained with the voltage-sensitive fluorescent dye 4{β-[2-(di-*n*-butylamino)-6-napathy]vinyl}pyridinium, a.k.a. di-4-ANEPPS, (Molecular Probes; 10 μmol/L bolus; 10μM) and immediately following, blebbistatin [52] (Enzo Life Sciences; 10 μmol/L constant infusion over 20 to 30 minutes) was administered to prevent motion artifacts.

### *3.3.2 Imaging hardware*

In order to properly characterize alternans and alternans control behavior in our tissue preparations, high spatial resolution signals were needed. Commonly used microelectrode techniques, though capable of providing high quality temporal voltage measurements, are spatially limited due to the difficulty in placing multiple electrodes in close proximity with one another, and their inherent fragility further complicates usage in tissue preparations. In contrast, optical mapping systems used in conjunction with voltage-sensitive fluorescent dyes are capable of providing very high spatial resolution measurements while maintaining adequate temporal resolution at each spatial location. For this reason, we opted to use a previously developed optical mapping system [41] for our experiments.

Technical limitations arise when attempting to simultaneously record from many spatial locations and further consideration was needed because of the real-time requirements of alternans control. Because imaging from too large an area would have caused an insurmountable data transfer bottleneck, we opted to use a line scan CCD camera capable of detection along a single dimension only, which greatly reduced the size of each frame.

The main hardware components of the optical mapping system included a line scan CCD camera, a custom-developed tandem-lens assembly, and an LED-based light source [41]. The CCD camera consisted of a 1-D array of 2,048 pixels, each 14 $\mu m^2$ in dimension. Use of the tandem lens assembly enabled x0.47 magnification at a working distance of 40 mm, while six 5-W high-powered LEDs, positioned no more than 20 mm from the tissue, provided the dye excitation. The imaging array was situated transverse to the long axis of the endocardial muscle fibers for all

experiments.

Recordings were performed at a frame rate of 1–2 KHz. In general, alternans frequencies were 1–3 Hz. Spurious signals at frequencies needed to adversely affect alternans measurements (aliasing) given the typical CCD integration times were not detected. A National Instruments PCI-6254 analog-to-digital board provided the link between the controlling software (RTXI; described in the next section) and the electrode stimulator. The short working distance of the tandem lens (allowing for high fluorescence signal detection) posed strict physical constraints, which prevented easy microelectrode access to points along the imaging line (including the control site). Thus, no microelectrode recordings were obtained.

### *3.3.3 Signal processing and software*

Real-time signal processing was needed for signal-to-noise (S/N) improvement and the removal of signal base line drift (attributable to voltage dye photo-bleaching and light-source instability). Use of a mean spatial filter (16-pixel width) improved S/N while effectively reducing the spatial resolution to 480 μm (1 recording channel = 16 pixels = 480 μm) and a nonlinear recursive high-pass filter [41] acted to detrend the signal in an effective and robust manner. In this way, 2,048 pixels were spatially averaged into 128 channels, each corresponding to 480 μm in length, which were used for all subsequent analyses.

Real-time data acquisition and control functionality was managed by the Real-Time eXperiment Interface (RTXI; www.rtxi.org), a software system developed specifically for real-time closed-loop feedback tasks of this type and successfully employed in several previously performed cardiac tissue control studies [33, 41]. The

optical signal measured at the control site (see *Section 3.3.4* for details on control channel selection) was fed into RTXI, and the system calculated the APD and determined any pacing rate modifications (according to the prescribed alternans control algorithm – see *Section 3.3.4* for details).

During post-acquisition processing, a 2-D spatiotemporal boxcar filter (5 pixels$^2$) was used to further smooth the data for analysis. APD threshold values at 80% of repolarization ($APD_{80}$) were used for post-processing analysis of alternans magnitude and dynamical behavior.

### *3.3.4 Experimental protocol*

Tissue pacing was administered via a bipolar electrode in firm contact with the surface of the tissue preparation. Pacing occurred at cycle lengths sufficiently fast so as to induce steady-state alternans at the pacing site (BCL range: 290–500 ms) and at each BCL tested, a pair of optical mapping images was acquired for each trial, the first half during static pacing (no-control) and the second during the application of alternans control at the pacing site. Each "image" consisted of 10–20 seconds of exposure time along the field-of-view.

The alternans control algorithm implemented by the system was similar to those used in previous cardiac control experiments [33, 34, 36]. The basic principle of alternans control is to force the underlying dynamical system to its unstable period-1 fixed point – having been made unstable by the dynamically induced period-doubling bifurcation (i.e., parameter-sensitive change to initial condition instability behavior [53]) that naturally occurs at sufficiently fast pacing rates [31]. By exploiting the APD restitution relationship [17], whereby smaller diastolic intervals (the "rest" period

before an action potential) correspond to smaller subsequent APDs, alternans control uses the APD information from consecutive action potentials to calculate the necessary adjustment to the cycle length in a manner that will decrease the alternans magnitude over time. The cycle length interval adjustment ($\Delta T$) and the resulting control-perturbed cycle length ($T_n$) are determined by the following equations [36]:

$$T_n = \begin{cases} T^* + \Delta T_n & \text{if } \Delta T_n < 0, \\ T^* & \text{if } \Delta T_n \geq 0, \end{cases} \quad \textbf{(1)}$$

where

$$\Delta T_n = (\lambda/2)(APD_n - APD_{n-1}), \quad \textbf{(2)}$$

$T^*$ is the target BCL (i.e., cycle length applied when control is turned off), $\lambda$ is the feedback gain, and $n$ is the beat number. In other words, given a sequence of alternating APDs (*L*-*S*-*L*-*S*), instances of $APD_{n-1}>APD_n$, which immediately follow relatively "short" (*S*) APDs and precede "long" (*L*) APDs, elicits a premature pulse ($T^*+\Delta T_n$) that effectively reduces the diastolic interval (DI) of the would-be "long" APD. This reduction in DI temporarily disrupts the steady-state alternating pattern by shortening the "long" APD and lengthening the subsequent "short" APD according to electrophysiological properties reflected in the APD restitution relationship. These situations require the repeated application of control, however, to maintain a relatively constant beat-to-beat APD pattern because of the system's dynamically-induced tendency towards an alternans rhythm [25].

Within this manuscript, references to "BCL" in the context of static pacing imply stimulation at a steady pacing rate, whereas in the context of alternans control, "BCL" refers to the target BCL ($T^*$). Given the relatively poor S/N inherent to optical mapping techniques and the increased likelihood that an errant APD measurement

would disrupt the controlling process, a relatively high feedback gain of 2.0 was chosen to achieve control quickly. Included in (1) is a condition that allows for only premature stimulation. Allowing only cycle length shortening more accurately reflects what would happen in a clinical setting during which the native excitation of the heart, corresponding to cycle length = $T^*$, cannot be delayed. Interestingly, algorithms using only negative perturbations have been shown analytically to have a larger successful control regime than those that apply both positive and negative perturbations [32].

All stimuli, whether statically-timed or control-perturbed, were administered using the same bipolar stimulating electrode at twice diastolic threshold (obtained @ BCL = 500 ms). The APD values measured by RTXI, and thus those used in the control algorithm, were those measured at the recording channel closest to the stimulating electrode. This channel, herein referred to as the *control channel*, was ≤2 mm from the stimulating electrode for all experiment trials. The APD thresholds used during real-time acquisition were chosen manually; post-acquisition analysis revealed that all threshold values were within the $APD_{90}$ to $APD_{60}$ range.

### *3.3.5 Data selection*

Alternans and alternans-control dynamics obtained from long recording durations were difficult to analyze because even the relatively small (given the temporal quality expectations of optical mapping recordings) amounts of noise associated with our recordings resulted in occasional mis-estimates of the true underlying APD and ill-timed perturbations during the application of control. As a result, we used APD values derived from a single sequence of six successive action potentials (six-AP) to calculate the resulting alternans magnitudes, on a channel-by-channel basis (the same six for each channel), for each imaging record.

The APD alternans fluctuation coefficient, $F$ (computed in (3)], was used to identify regions of stable alternans during control-off conditions. For each post-processed control-off image, the six-AP sequence corresponding to the largest alternans magnitude, $A_M$ [computed in (4)], with $F < 0.5$ was selected for analysis. For each post-processed control-on image, the sequence with the smallest alternans magnitude ($A_M$) was used. The selection of all sequences was determined by the APD measurements derived from the control channel only.

Control pairs in which the control-off and control-on results at the control channel yielded sequences of robust, steady-state alternans ($A_M > 10$ ms; $F < 0.5$) and successful alternans control ($A_M \leq 10$ ms), respectively, were selected for final analysis. This resulted in 17 pairs of control-off/control-on images, derived from six preparations, being chosen. For each BCL that yielded multiple pairs of useable data for a particular preparation, the pair consisting of the best control-off results was selected. It should be noted that the trial selection criteria were constructed in an effort to analyze and quantify the spatial efficacy of control – analysis of the overall control success rate was not an objective of this study.

### *3.3.6 Equations*

*Alternans Fluctuation Coefficient*

The APD alternans fluctuation coefficient, $F$, was used as a measure of the variation in beat-to-beat alternans within a given series of action potentials. The fluctuation coefficient was calculated according to the following:

Given a sequence of APD Δ values, $D$:

$D = \left(\left|A_2 - A_1\right|, \left|A_3 - A_2\right|, \ \ldots \ , \left|A_n - A_{n-1}\right|\right),$

where $A$ is a sequence of $n$ positive real APD values:

$A = \left(A_1, A_2, \ \ldots, A_n\right),$

the alternans fluctuation coefficient, $F$, is defined as:

$$F = \left[\max(D) - \min(D)\right] / \text{mean}(D). \quad \textbf{(3)}$$

*Alternans Magnitude Calculation*

The APD alternans magnitude for a given series of action potentials was calculated according to the following:

Given a sequence of $n$ positive real APD values, $A$:

$A = (A_1, A_2, \ \ldots, A_n),$

alternans magnitude, $A_M$, is defined as:

$$A_M = \left( \sum_{i=1}^{n-1} \left| A_{i+1} - A_i \right| \right) / (n-1) \quad \textbf{(4)}$$

and phase-specific alternans magnitude, a.k.a. alternans difference, $A_D$, is defined as:

$$A_D = \left( \sum_{i=1}^{n-1} \left( A_{i+1} - A_i \right) (-1)^i \right) / (n-1). \quad \textbf{(5)}$$

The different alternans equations enabled the quantification of both alternans magnitude (4) – useful when analyzing spatially averaged alternans reduction – and phase-specific alternans magnitude (5) – necessary in the analysis of alternans spatial dynamics (i.e., concordance vs. discordance). Calculations of $|A_D|$, as opposed to $A_M$ (technically, a measurement of absolute variability), are sensitive to alternans phase reversals with respect to time, which often occurred during the application of control, resulting in misleadingly small alternans values. Thus, $A_M$ was used where appropriate.

(It should be noted that $|A_D|$ quantification led to almost identical hypothesis testing results).

### *3.3.7 Statistical analysis*

Statistical comparisons between control-off and control-on spatially averaged $A_M$ values ($A_{M,S}$ – Table I) were achieved using paired student t-tests. For each experiment trial, channel-indexed pairs resulted in comparisons between control-off and control-on $A_{M,S}$ values. Comparisons within specific regions of tissue (0.0–2.5 cm, 0.0–1.0 cm, 1.0–2.0 cm, and 2.0–2.5 cm) resulted in p-values associated for each (Table I).

Statistical comparisons of control efficacy between different regions of tissue were achieved using paired student t-tests. In this case, pairs indexed by individual trial, comparing $A_{M,S}$ reduction ($\Delta$) with respect to specific regions of tissue, resulted in spatial comparisons of control efficacy (Fig. 3.6).

Repolarization dispersion values ($\sigma^2$) were calculated, for each action potential in a given six-AP sequence, by computing the variance in repolarization times with respect to control channel activity. Grouping action potentials from every-other beat resulted in two sets ($AP_n$ and $AP_{n+1}$) of three action potentials [$AP_n = (AP_1, AP_3, AP_5)$; $AP_{n+1} = (AP_2, AP_4, AP_6)$]. Mean $\sigma^2$ values ($\overline{\sigma^2}$) were computed for each set and the greater of the two was used in the analysis of the three concordant/control-off : discordant/control-on cases [Fig. 3.4(e)] and that of the four discordant/control-off : discordant/control-on cases (see Discussion).

All error bars shown denote standard error.

## 3.4 Results

### *3.4.1 Control channel results (preparations #1)*

Examples of APD alternans behavior (and signal quality) induced at the control site under static and control-adjusted pacing are illustrated in Fig. 3.1. An optical mapping recording during static pacing is shown in Fig. 3.1(a), and the resulting APD values, as were measured by the system, are denoted by the gray X's superimposed on the trace. Beat-to-beat alternations were fairly constant for the duration of the recording, reflective of steady-state dynamical behavior.

Immediately following the acquisition of the control-off image, control was applied at the control site; the resulting optical signal is shown in Fig. 3.1(b). This panel demonstrates the system's ability to acquire optical data, calculate the necessary changes in cycle length, and deliver the controlling electrical stimulus (notice changes in cycle length as a function of preceding APD values) – all in real-time. Directly comparing the APD values from the control-off (gray X's) and control-on (red X's) halves of the trial illustrates more clearly the high degree of control the system was able to achieve. Reverting back to static pacing allowed for the return of large and stable alternans at the control site [Fig. 3.1(c)].

Comparing the post-processed six-AP sequences associated with this particular control-off/control-on trial (selected according to the methods explained in *Section 3.3.5*) exemplifies the effect that control had on the entire action potential waveform. Static pacing yielded clear alternations in the beat-to-beat waveform [Fig. 3.1(d)], whereas the application of control resulted in consistently similar waveforms and the near elimination of APD alternans [Fig. 3.1(e)].

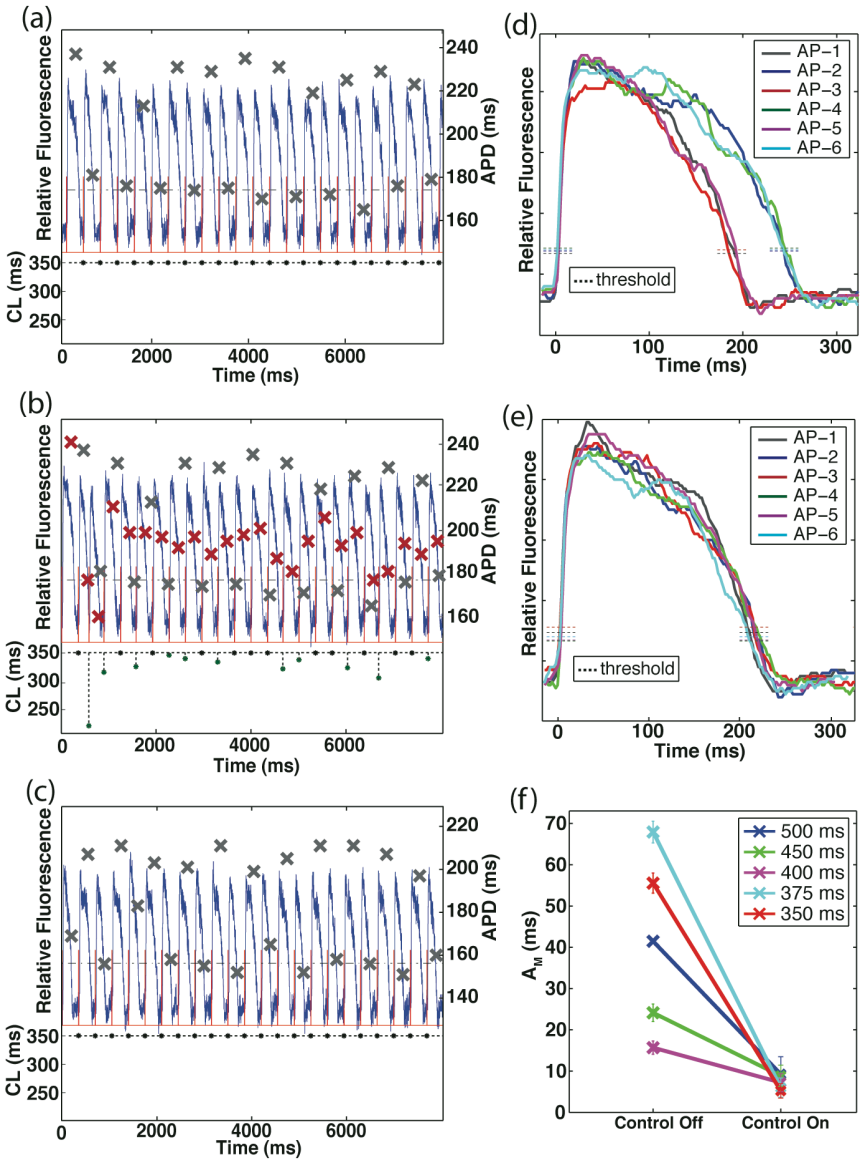


**Figure 3.1. Optical signal recording examples.** Optical signal recordings and APD alternans results derived from the control channel during statically-timed and control-perturbed pacing (preparation #1). (a) Pre-processed optical recording during static pacing (top – left axis; BCL = 350 ms); superimposed X's denote APD values (right axis). Bottom-axis shows the preceding pacing cycle length (CL) for the corresponding action potential. APD threshold values and stimuli are shown as the dashed black line and the red trace, respectively. (b) Pre-processed optical recording during the application of control (BCL = 350 ms); immediately followed that shown in (a). Superimposed red (gray) X's denote APD values for control-on (control-off). Note change in cycle lengths as a function of preceding APD values. (c) Subsequent control-off optical recording resulted in the re-emergence of robust alternans at the control site (post-processed six-AP $A_M$ = 55 +/- 1.8 ms). (d)-(e) Action potential waveforms of post-processed six-AP sequences during control-off (d; six-AP $A_M$ = 56 +/- 2.4 ms) and control-on (e; six-AP $A_M$ = 5 +/- 1.7 ms) conditions; sequence selected according to the methods described in *Section 3.3.5* (f) Control-off and control-on six-AP $A_M$ values calculated at the control channel derived from all experiment trials performed on preparation #1 (BCL = 500, 450, 400, 375, and 350 ms).

A total of five trials, each at a different BCL, were performed on this particular preparation. A summary of the control channel results is shown in Fig. 3.1(f). As shown in the figure, at each of the five BCLs tested, control greatly reduced $A_M$ at the control site.

### *3.4.2 Spatial results*

The optical mapping system enabled the observation and post-hoc analysis of action potential dynamics at points distal to the control site with high spatial and temporal resolution. Fig. 3.2(a) shows an example optical signal, as a function of distance and time, acquired during the application of control. The spatial location of the stimulating electrode and the timings of the applied stimulus current are denoted on the distance-time plot by the vertical-dashed red line and the horizontal-dashed white lines, respectively. Propagation of the wave front, which starts at the point of stimulation on the left-hand side, is smooth and linear, and from its inverse slope the CV of the wave front can be calculated. For any given experiment trial, the conduction velocity along the entire field-of-view was measured to be constant (CV range across trials: 84–115 cm/s).

Optical mapping signals from a continuous region of tissue consisting of 53 channels (≈2.5 cm; as described in *Section 3.3.3*, each channel was comprised of 16 pixels, each pixel corresponding to 30 μm) were used for the spatial analysis. Fig. 3.2(b) is a plot of the calculated $A_D$ values for each of the 53 channels, beginning with the control channel, during one alternans control trial (preparation #1 – BCL = 350 ms). As reflected in the control-off spatial profile, static pacing resulted in concordant alternans with large $A_D$ values along the entire field-of-view. The noted decrease in $A_D$ magnitude at points distal to the site of stimulation is similar in profile to that seen in

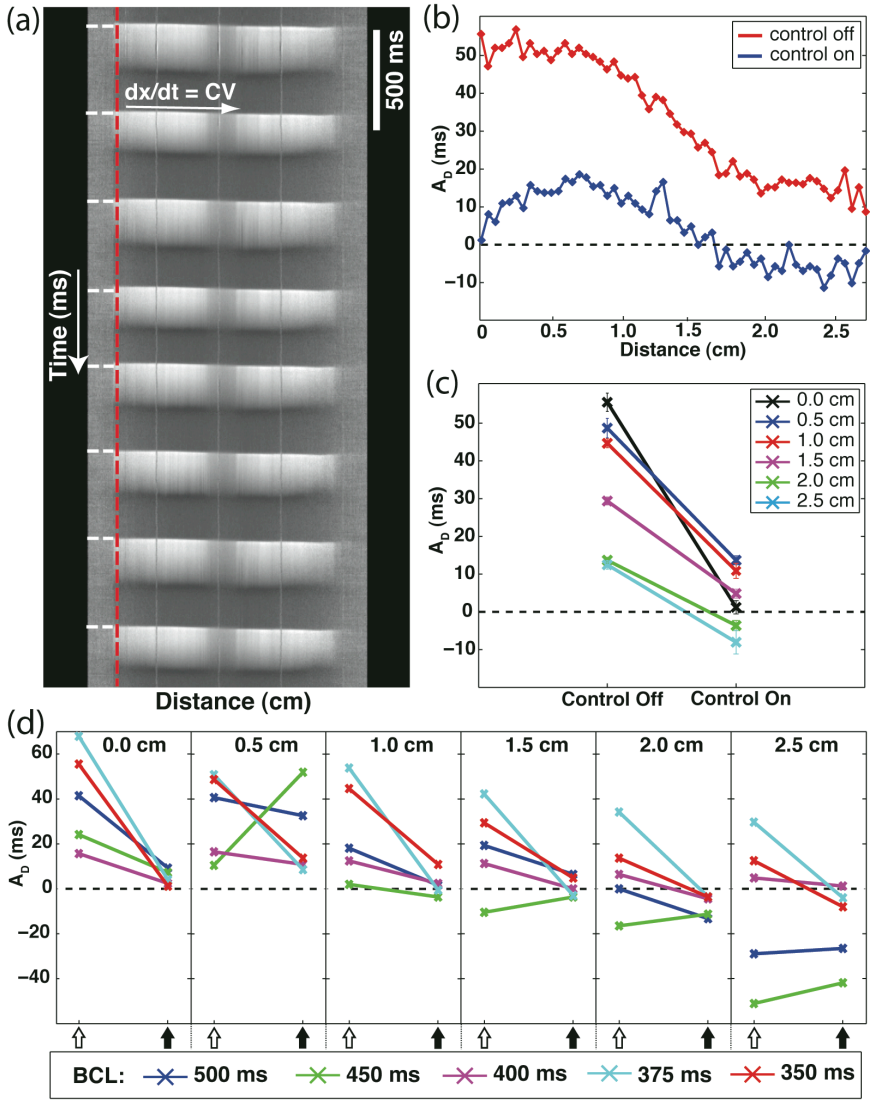


**Figure 3.2 Examples of spatial alternans dynamics.** (a) Example distance-time plot of relative fluorescence data. Shown is the propagation of eight action potentials along the length of the tissue (BCL = 420 ms; CV = 92 cm/s). Color-coding: white – depolarized fluorescence; gray – resting fluorescence. The vertical-dashed red line and the horizontal-dashed white lines on the left-hand side of the plot correspond to the spatial location of the stimulating electrode and the timings of the applied stimulus current, respectively. The three equally spaced wavy vertical lines are from the calibration coverslip, which was placed over the sample preparation (1 cm spacing). This signal was detrended and smoothed according to the methods described in *Section 3.3.3* (b)-(d): Phase-specific alternans magnitudes, $A_D$, measured during control-off and control-on conditions (preparation #1). (b) Measurements from each channel within the field-of-view (BCL = 350 ms). Control-off – red; Control-on – blue. (c) Measurements from equally spaced locations from the control channel (distances = 0.0, 0.5, 1.0, 1.5, 2.0, and 2.5 cm; BCL = 350 ms). (d) Spatial measurements derived from all experiment trials performed on preparation #1 (BCL = 500, 450, 400, 375, and 350 ms). Open-arrows: control-off; closed-arrows: control-on.

Purkinje fiber studies [36]. In contrast, the application of control resulted in spatially discordant alternans along the imaging line, characterized by the presence of two distinct regions of out-of-phase alternans behavior. Two nodes of no-alternans resulted – one separating the two out-of-phase regions and another, reflecting the successful application of control, at the control site. Along with a change in spatial dynamics, alternans control resulted in a marked decrease in $A_D$ magnitude across the entire length of the imaged tissue.

Selecting equally spaced locations (distances = 0.0, 0.5, 1.0, 1.5, 2.0, and 2.5 cm from the control channel) allowed for easier visualization of multiple data sets while still retaining pertinent spatial dynamical information. The control-off and control-on alternans values of Fig. 3.2(b) are displayed in this manner within Fig. 3.2(c). Comparing the before and after conditions, both the reduction in $A_D$ magnitude at points along the imaging line and the induction of discordant alternans during the application of control are evident.

The control-off and control-on spatial dynamics at each of the five BCLs tested on this particular preparation (#1) are shown in Fig. 3.2(d). In the absence of control, concordant alternans was observed at three of the five BCLs tested (400, 375, and 350 ms), whereas discordant alternans was clearly discernable during the other two (500 and 450 ms). Some of the results during control-on were ambiguous (likely due to the localized viewing region) but in each of the three cases exhibiting concordant control-off behavior, control reduced the $A_D$ at each representative spatial location to values below 10 ms in magnitude.

Experimental results compiled from all trials across all preparations are

summarized in Fig. 3.3. As determined by the selection criteria described in *Section 3.3.5*, robust steady-state alternans was observed at the control channel for each trial during static pacing ($A_D$ range: 14 –68 ms, mean: 35 ms) and control reduced the $A_D$ to values ≤10 ms (range: 2–10 ms, mean: 5 ms) in all cases [Fig. 3.3(a), first panel]. In addition, three different control-off:control-on pairings of spatial dynamics were observed – concordant:concordant, concordant:discordant, and discordant:discordant [Fig. 3.3(b)]. (The spatial dynamics were indeterminate for several of the trials).

Cases of concordant:discordant behavior [preparation #1: 350, 375 ms – Fig. 3.2(d); preparation #5: 400 ms – Fig. 3.3(b)] are of particular importance given the recent attention concerning the genesis, dynamics, and general characteristics of discordant alternans [13-15, 24, 48, 49]. Instances of discordant alternans are usually associated with an increase in repolarization gradients (dispersion), which can be quantified by calculating the variance in the times to repolarization ($\sigma^2$) within a chosen region of space. Fig. 3.4 shows the APD and repolarization time profiles for $AP_1$ and $AP_2$ (representative $AP_n/AP_{n+1}$ pair) during the absence [Fig. 3.4(a),(c)] and presence [Fig. 3.4(b),(d)] of control (preparation #1 – BCL = 350 ms). The observed differences in the APD profiles [Fig. 3.4(a),(b)] reflect the control-induced transition from concordance to discordance that occurred within the imaging region, whereas the differences in the relative repolarization time profiles [Fig. 3.4(c),(d)] simply reflect the dynamics associated with each representative action potential. $\overline{\sigma^2}$ values calculated from the repolarization times of the $AP_n$ and $AP_{n+1}$ action potential sets derived from this trial (see *Section 3.3.7* for selection specifics) show a decrease in repolarization dispersion after the application of control despite the transition from concordance to discordance [Fig. 3.4(e), first column pair]. This observation can be attributed to the overall reduction in alternans magnitude (quantified next) that accompanied the

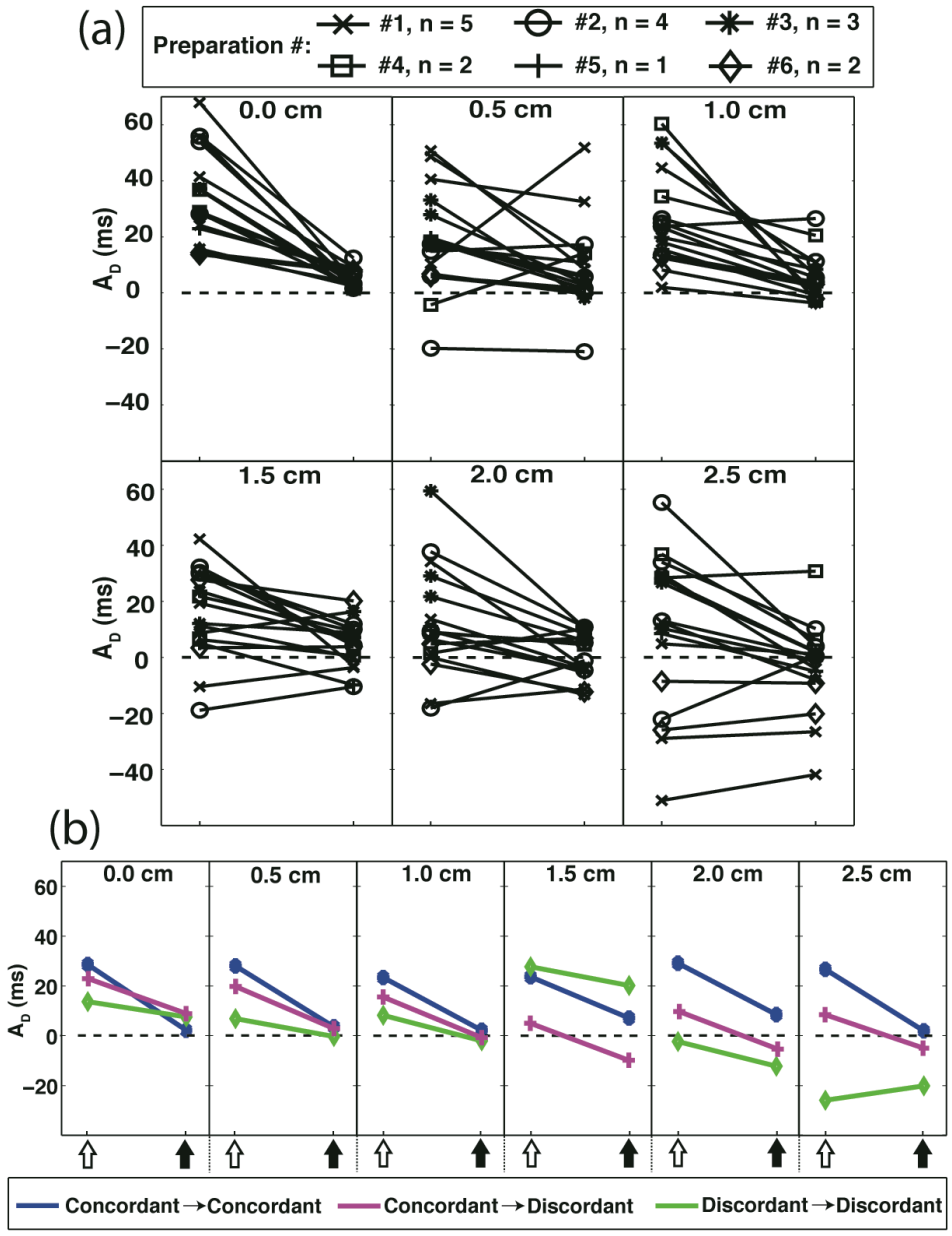


**Figure 3.3 Phase-specific alternans magnitudes results** $A_D$, measured during control-off and control-on conditions. Measurements are from equally spaced locations from the control channel (distances = 0.0, 0.5, 1.0, 1.5, 2.0, and 2.5 cm). (a) Results from all experiment trials (# of preparations = 6, n = 17 total trials). (b) Representative spatial dynamics results demonstrating effect of control. Control-off:control-on pairings – concordant:concordant (preparation #3: BCL = 420 ms); concordant:discordant (preparation #5: BCL = 400 ms); discordant:discordant (preparation #6: BCL = 390 ms). Open-arrows: control-off; closed-arrows: control-on.

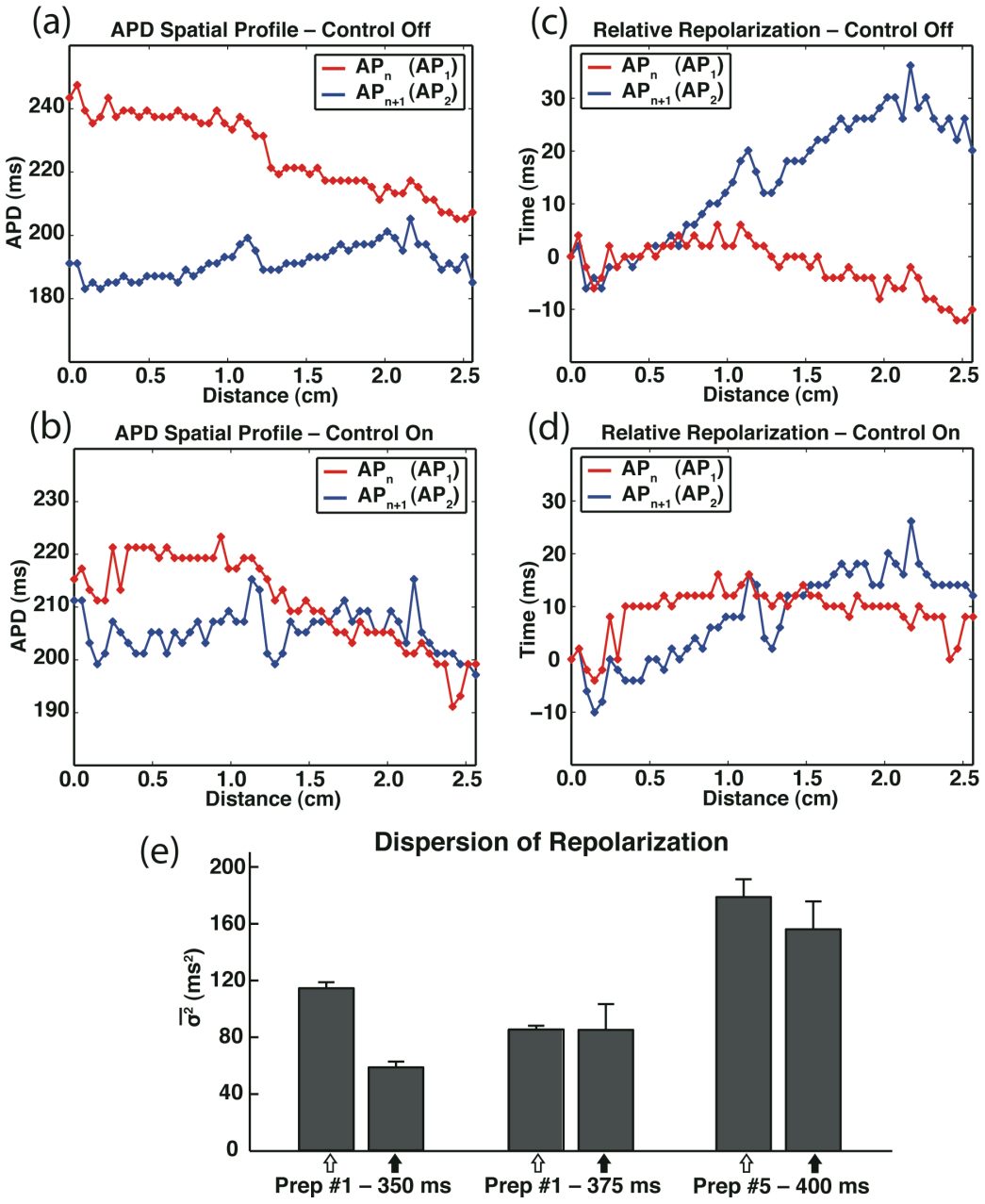


**Figure 3.4 Control-induced transition from concordance to discordance**. (a)-(b) Representative APD spatial profiles for $AP_n$ and $AP_{n+1}$ (first two action potentials of six-AP sequence) during control-off (a) and control-on (b). (c)-(d) Representative relative repolarization times for $AP_n$ and $AP_{n+1}$ during control-off (c; $AP_1$-$\sigma^2$: 22.4 $ms^2$, $AP_2$-$\sigma^2$: 122.2 $ms^2$) and control-on (d; $AP_1$-$\sigma^2$: 13.5 $ms^2$, $AP_2$-$\sigma^2$: 59.9 $ms^2$) conditions. (a-d: Preparation #1 – BCL = 350 ms.) (e) Control-off:control-on (open-arrows and closed-arrows, respectively) repolarization dispersion values ( $\overline{\sigma^2}$) derived from cases of concordant:discordant behavior (preparation #1 – BCL = 350, 375 ms; preparation #5 – BCL = 400 ms). Shown is the greater of the two $\sigma^2$-mean ($\overline{\sigma^2}$) values calculated for each six-AP sequence: $AP_n$-$\overline{\sigma^2}$ (n=3) or $AP_{n+1}$-$\overline{\sigma^2}$ (n=3).

successful application of control, which effectively outweighed the positive effect that a phase reversal has on dispersion. Fig. 3.4(e) also shows the effect that alternans control had on $\overline{\sigma^2}$ for the other two observed instances of clear concordant:discordant behavior. In all, the calculated dispersion ($\overline{\sigma^2}$) either decreased or remained constant with the application of control.

The spatial efficacy of alternans control was quantified by averaging the $A_M$ values across regions of space. Comparing the results from statically-paced and control-perturbed conditions, control reduced the spatially averaged alternans magnitude, $A_{M,S}$, as calculated for the entire 2.5 cm length for each trial [Fig. 3.5(a)]. Table I includes the before and after $A_{M,S}$ values and the control induced reduction ($\Delta$) for each trial. A channel-specific paired t-test calculated for channels spanning the entire 0.0–2.5 cm region of tissue reveals significant ($p < 0.05$) reductions in alternans for 15/17 of the trials.

To determine more precisely the spatial effect that control had on the tissue, we compared the extent to which control reduced $A_{M,S}$ at the proximal (0–1 cm), middle (1–2 cm), and distal (2–2.5 cm) regions of tissue. Focusing first on each individual subregion of tissue, Fig. 3.5(b)-(d) shows the $A_{M,S}$ values for each, calculated across all trials. Control reduced $A_{M,S}$ by a significant amount in 15/17, 12/17, and 8/17 cases with respect to the proximal (b), middle (c), and distal (d) regions of tissue ($p < 0.05$, Table I).

A trial-specific paired t-test, comparing the control-induced reductions ($\Delta$) of one tissue segment with that of another across all trials reveals that a significantly greater reduction in $A_{M,S}$ occurred at the proximal end of the tissue as compared with

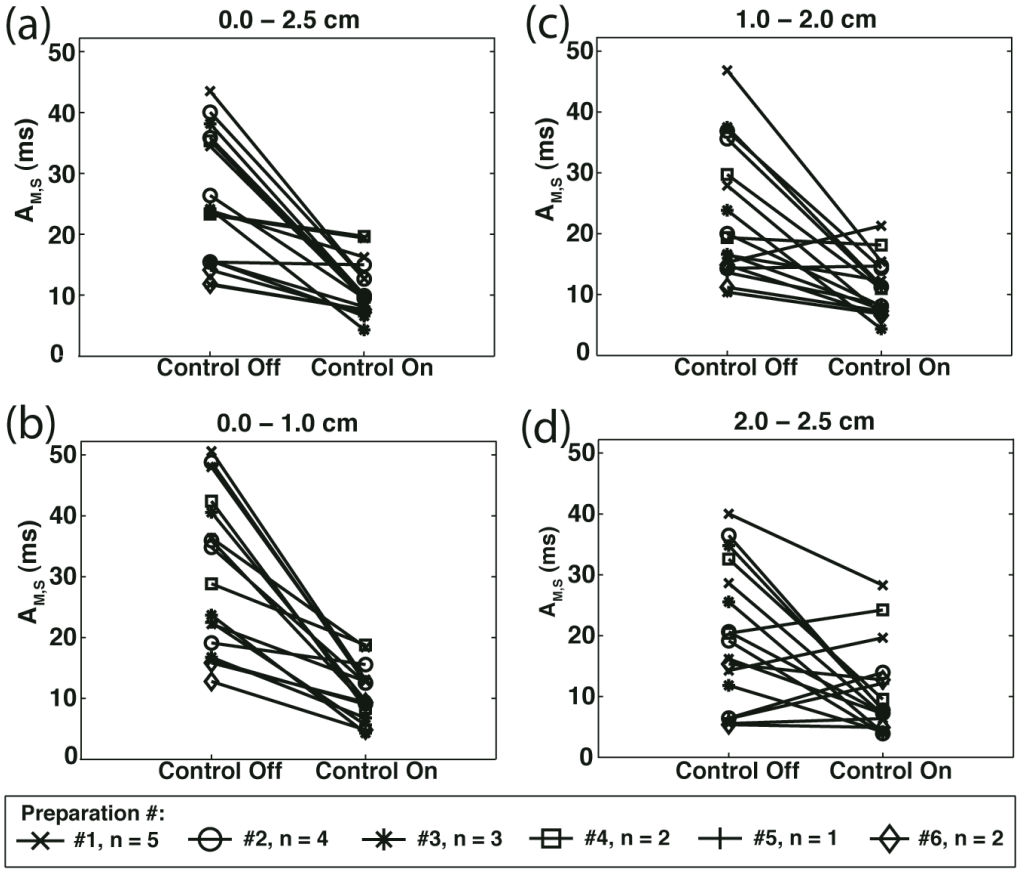


**Figure 3.5 Spatially averaged alternans magnitudes.** $A_{M,S}$ under control-off and control-on conditions; compiled from all trials (# of preparations = 6, n = 17 total trials). (a) 0.0–2.5 cm; (b) 0.0–1.0 cm; (c) 1.0–2.0 cm; (d) 2.0–2.5 cm.

| | | 0 – 2.5 cm | | | | 0 – 1 cm | | | | 1 – 2 cm | | | | 2 – 2.5 cm | | | |
|---|---|---|---|---|---|---|---|---|---|---|---|---|---|---|---|---|---|
| | | control-off | control-on | | | control-off | control-on | | | control-off | control-on | | | control-off | control-on | | |
| | BCL | $A_{M,S}$ | $A_{M,S}$ | Δ | p | $A_{M,S}$ | $A_{M,S}$ | Δ | p | $A_{M,S}$ | $A_{M,S}$ | Δ | p | $A_{M,S}$ | $A_{M,S}$ | Δ | p |
| **Preparation #1** | 500 | 23.9 | 16.2 | 7.7 | <0.01 | 36.4 | 18.4 | 18.0 | <0.01 | 16.5 | 12.3 | 4.2 | >0.05 | 14.3 | 19.6 | -5.4 | <0.05 |
| | 450 | 23.2 | 19.4 | 3.8 | >0.05 | 22.2 | 12.8 | 9.4 | >0.05 | 15.3 | 21.3 | -6.0 | >0.05 | 40.0 | 28.3 | 11.7 | <0.01 |
| | 400 | 11.7 | 7.6 | 4.1 | <0.01 | 16.2 | 9.0 | 7.2 | <0.01 | 10.4 | 6.8 | 3.6 | <0.01 | 5.6 | 6.4 | -0.8 | >0.05 |
| | 375 | 43.5 | 12.7 | 30.8 | <0.01 | 48.0 | 12.9 | 35.1 | <0.01 | 46.8 | 15.4 | 31.4 | <0.01 | 28.6 | 7.1 | 21.5 | <0.01 |
| | 350 | 34.5 | 9.4 | 25.1 | <0.01 | 50.6 | 13.1 | 37.5 | <0.01 | 27.9 | 6.8 | 21.1 | <0.01 | 16.2 | 7.2 | 9.0 | <0.01 |
| **Preparation #2** | 460 | 35.9 | 9.9 | 26.0 | <0.01 | 36.0 | 9.2 | 26.8 | <0.01 | 35.6 | 11.3 | 24.3 | <0.01 | 36.5 | 7.7 | 28.7 | <0.05 |
| | 420 | 40.1 | 12.7 | 27.4 | <0.01 | 48.8 | 12.5 | 36.3 | <0.01 | 36.9 | 14.3 | 22.5 | <0.01 | 20.6 | 7.3 | 13.3 | >0.05 |
| | 415 | 26.4 | 15.0 | 11.4 | <0.01 | 34.8 | 12.1 | 22.7 | <0.01 | 20.0 | 12.5 | 7.5 | >0.05 | 19.1 | 33.6 | -14.5 | <0.05 |
| | 400 | 15.4 | 15.0 | 0.5 | >0.05 | 19.1 | 15.6 | 3.6 | >0.05 | 14.3 | 14.7 | -0.4 | >0.05 | 6.4 | 13.9 | -7.5 | <0.05 |
| **Preparation #3** | 430 | 15.7 | 6.6 | 9.1 | <0.01 | 16.7 | 6.8 | 10.0 | <0.01 | 16.6 | 7.6 | 9.1 | <0.01 | 11.8 | 4.2 | 7.6 | <0.01 |
| | 420 | 24.1 | 4.3 | 19.9 | <0.01 | 23.7 | 4.3 | 19.4 | <0.01 | 23.8 | 4.4 | 19.5 | <0.01 | 25.5 | 4.1 | 21.5 | <0.01 |
| | 410 | 38.2 | 10.0 | 28.2 | <0.01 | 40.6 | 9.6 | 31.0 | <0.01 | 37.5 | 11.5 | 26.0 | <0.01 | 34.8 | 7.9 | 26.9 | <0.01 |
| **Preparation #4** | 300 | 23.3 | 19.7 | 3.7 | <0.05 | 28.8 | 18.8 | 10.1 | <0.01 | 19.4 | 18.1 | 1.2 | >0.05 | 20.4 | 24.2 | -3.8 | >0.05 |
| | 290 | 35.4 | 9.7 | 25.7 | <0.01 | 42.4 | 8.4 | 34.0 | <0.01 | 29.7 | 11.0 | 18.7 | <0.01 | 32.6 | 9.5 | 23.0 | <0.01 |
| **Preparation #5** | 400 | 15.6 | 8.1 | 7.6 | <0.01 | 22.5 | 5.6 | 16.9 | <0.01 | 13.6 | 8.4 | 5.2 | <0.01 | 6.3 | 12.2 | -5.8 | <0.05 |
| **Preparation #6** | 400 | 11.8 | 7.6 | 4.2 | <0.01 | 15.8 | 9.3 | 6.5 | <0.01 | 11.2 | 7.3 | 3.9 | <0.01 | 5.4 | 4.9 | 0.5 | >0.05 |
| | 390 | 14.1 | 7.16 | 7.0 | <0.01 | 12.8 | 4.8 | 8.0 | <0.01 | 14.9 | 6.6 | 8.3 | <0.01 | 15.3 | 12.7 | 2.6 | >0.05 |

**Table 3.1 Spatially averaged alternans results for all experimental trials.** Trial-by-trial comparisons of spatially averaged alternans magnitude ($A_{M,S}$) during control-off and control-on conditions for different subregions of tissue (0.0–2.5 cm; 0.0–1.0 cm; 1.0–2.0 cm; 2.0–2.5 cm). "Δ" denotes difference between control-off and control-on $A_{M,S}$ value; p-value indicates significance level of the paired student t-test result for the associated trial and tissue subregion. Pairing was according to spatial location (i.e., channel-specific paired t-test). Elements shaded denote a statistically significant decrease in $A_{M,S}$ was observed during the application of control.

both the middle and distal regions, both in absolute and proportional amounts, suggesting a decrease in control efficacy as a function of distance ($p < 0.05$; Fig. 3.6).

### 3.5 Discussion and Conclusion

Previous studies of alternans control have been limited to Purkinje fibers [34, 36], and though informative, a better understanding of alternans control dynamics in the more clinically relevant ventricular tissue is needed. In this study, we investigated the effects of static pacing and single-site control applied to arterially perfused canine right ventricular preparations using an optical mapping system capable of high-resolution transmembrane voltage imaging. We were able to demonstrate that compared with static pacing, the application of alternans control significantly reduced the spatially averaged alternans magnitude ($A_{M,S}$) across 2.5 cm of tissue [Fig. 3.5(a)] – a result which was observed across several different preparations and at varying BCLs. Furthermore, we showed that control-induced reduction was greatest for regions of the tissue that were most proximal to the control site, indicating an attenuation of control efficacy as a function of distance (Fig. 3.6) – in agreement with previous Purkinje fiber study results [34, 36].

In our experiments, we observed the two spatial manifestations of alternans – concordant and discordant – and though we were unable to draw any statistically significant results linking spatial efficacy of control with alternans type, important observations can still be made.

The likely mechanism by which alternans promotes conduction block and

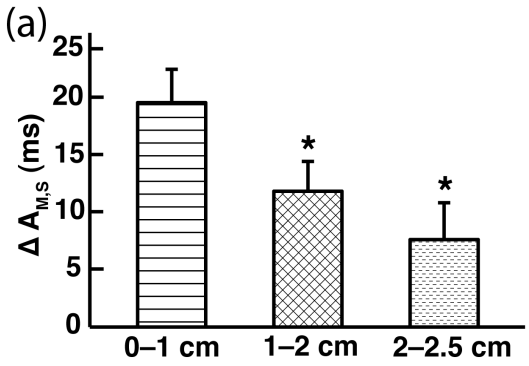


**Figure 3.6 Reduction in spatially averaged alternans magnitude.** $A_{M,S}$ across different subregions of tissue. Both absolute (Δ) and percentage [Δ (%)] reductions were computed [%Δ$A_{M,S}$: 0.0–1.0 cm (60%), 1.0–2.0 cm (40%), 2.0–2.5 cm (20%)]. "*" indicates a statistically significant difference ($p < 0.05$) in reduction was observed when comparing the reduction for the proximal (0.0–1.0 cm) region with that of either the middle (1.0–2.0 cm) or distal (2.0–2.5 cm) region of tissue. Similar statistical significance results for %Δ$A_{M,S}$ regional comparisons were observed (data not shown).

subsequent VF formation involves the creation of steep repolarization gradients within the tissue. Thus, substantial reductions in gradient magnitude are potentially anti-arrhythmic. Previous studies have quantified relative gradient steepness using dispersion calculations [13, 24, 54]. Examples illustrating the direct causal relationship between dispersion (both APD and repolarization specific) and wave-break abound [13-15, 24].

Given the successful application of control, a decrease in the overall alternans magnitude will tend to reduce the gradients of repolarization within regions sufficiently close to the control site. Successful control would likely reduce the gradients of repolarization when comparing discordant/control-off and discordant/control-on cases (discordant:discordant) and certainly when comparing discordant/control-off and concordant/control-on cases (no observations of the latter off/on pairing were made in our experiments). Analysis of the discordant:discordant cases observed in our experiments (preparation #1 – BCL = 500, 450 ms; preparation #6 – BCL = 400, 390 ms) suggest that this was the case ($\%\Delta\overline{\sigma^2}$, percentage reduction after control application = 30%, 11%, 27%, and 38%, respectively – data not shown). Even in cases when large-amplitude concordant alternans was transformed into small-amplitude discordant alternans (Fig. 3.4), one can argue that such a result would be desirable given the tendency for large-scale concordant alternans to transform into large-scale discordant alternans with either a slight decrease in pacing cycle length or a properly timed ectopic beat [24, 49]. Moreover, $\sigma^2$ calculations derived from our experiments suggest that the dispersion remained the same or decreased during the control portion of these concordant:discordant trials [Fig. 3.4(e)]. That a concordant:discordant reduction in dispersion is possible implies a positive $\sigma^2$ (relative to the natural dispersion resulting from forward AP propagation) existed

during control-off concordant alternans behavior. This could result from spatial heterogeneities that naturally exist in cardiac physiology [54-56]. Reducing alternans magnitude in such systems could be of particular benefit. More precise repolarization measurements made possible by better imaging techniques will further address these issues, while allowing for generally better analysis and understanding of action potential propagation dynamics in cardiac tissue.

Although recent studies have proposed several possible mechanisms for discordant alternans initiation, this process is still not completely understood. Sudden changes in pacing cycle length [24], ectopic beat activity [49], and CV/APD restitution interactions [48] may all play a role. A significant limitation in our experiments was the inability to capture long duration (>1 min) noise-free action potential sequences. To fully understand the time-dependent phenomena associated with discordant alternans dynamics (e.g., initiation, node movement, etc.), both with and without respect to alternans control, an imaging system capable of longer acquisition times is necessary.

The whole tissue dynamics of wave propagation and alternans across the surface of any particular preparation were missed by our imaging system, which was capable of imaging from a 1-D line segment only. However, in all cases there was close proximity between the control channel and the stimulating electrode (≤2 mm), and forward wave propagation originating from the control channel was observed along the imaging line in all of the analyzed trials. Because of this, both the dynamical manifestations of alternans and the induced changes as observed within the field-of-view were likely the direct result of pacing by the stimulating electrode. That being said, cases of ambiguity would be expected given the noise inherent to the system.

This also does not preclude the existence of other dynamics along other propagation axes and at distances beyond the scope of the 2.5 cm viewing region. Qualitative differences in the observed alternans control behavior with respect to viewing orientation would certainly be expected, in part due to the differences in propagation velocity parallel and transverse to fiber orientation [37-39]. Doubtless, high-fidelity observations of whole tissue dynamics are a next step that would yield useful information.

The benefits of using fluorescent dyes like di-4-ANEPPS for cardiac electrodynamical experiments (linearly changing fluorescence behavior in response to changes in transmembrane potential, the ability to track voltage changes on a time scale of microseconds [57], etc.) are tempered by the S/N issues that are commonly associated [57, 58]. The largest source of noise in our optical mapping system was due to the light detection limits of the CCD camera, and given the operational range of our experiments, shot noise represented the predominant CCD-related noise present [41]. Noise level increases over the time-course of 1/2 hour could be expected [41], but limiting analysis to six-AP sequences largely controlled for this.

In choosing to use the optical mapping system, a trade-off between spatial and temporal resolution was implicitly made. On the one hand, by using the optical system we were able to clearly observe both concordant and discordant alternans dynamics, and our ability to quantify the spatial effects of alternans control was enhanced. On the other, the inherently more noisy system (as compared with microelectrode recordings) made experiment execution and downstream analysis more difficult. To compensate for these limitations, we aimed to uncover the true behavior of alternans behavior during static pacing and control intervention by selecting a six action potential

sequence according to the methods described in *Section3.3.5.* Whereas the use of the fluctuation coefficient selected for stable alternans dynamics during control-off conditions, selection for representative "successful control" sequences was based only on the control site alternans magnitude. This type of selection would bias our results if we were interested in the overall success rate of alternans control, but our primary concern was the spatial efficacy of control given effective control at the control site. In choosing the six-AP sequence, only the alternans magnitude at the control channel was used and the aim was to focus on periods during which control was successful; subsequent spatial analysis followed accordingly.

The inability to completely eliminate alternans at the site of intervention is not at all surprising given the noise inherent to the system. Additionally, despite placing the stimulating electrode at distances $\leq$2 mm from the control channel, small location disparities could have further destabilized the control mechanism – the straightforward result of wave propagation and the time delays associated. But even in the absence of noise and location disparities, the failure of complete control would be expected, nonetheless, because of the effects of electrical coupling between neighboring cells, as predicted by previously published analytical work [34].

In order to promote large-scale alternans, our experiments were conducted at a reduced temperature [13, 59] rather than body temperature. Changes to cell function kinetics, specifically $Ca^{2+}$ handling dynamics, at lower temperatures have been well documented [60]. That notwithstanding, the same underlying mechanisms for concordant and discordant alternans should apply at slightly reduced temperatures as it does for physiological temperatures and any differences in control would likely be quantitative but not qualitative. Precise measurements of physiological controllable

distances, however, will necessitate further experiments conducted at near-physiological conditions.

The spatial reduction in alternans magnitude is an average across regions of tissue, and as such, a reduction across 2.5 cm of tissue does not necessarily constitute equal control efficacy as a function of space. The comparisons of alternans control between the proximal, middle, and distal regions were intended to uncover these differences. Spatially averaging across regions spanning less than 1.0 cm were avoided when possible due to the loss in statistical power associated with quantifying alternans dynamics across too few channels (unfortunately, the image quality was inadequate beyond 2.5 cm for many of the trials, hence the inclusion and analysis of the 2.0–2.5 cm region). Given that previous control experiments have suggested ≈1 cm as the controllable "unit" for single-site control [34, 36], use of this sub-division length-scale seemed both adequate and appropriate. Ideally, statistical analysis of control efficacy would have been done on a preparation-by-preparation basis, but the individual sample sizes were not large enough. More rigorous statistical testing will accompany larger data sets in the future.

Although control decreased alternans to a greater extent in the regions more proximal to the control site, it should be noted that even in the middle (1–2 cm) tissue region, control reduced $A_{M,S}$ by a statistically significant amount in 12/17 experiment trials. As well as decreasing the magnitude (mean reduction across all trials = 12 ms), the resulting $A_{M,S}$ after the application of control was ≤ 10 ms in 7/17 cases (mean control-on $A_{M,S}$ = 11 ms – Table I). Fully understanding the reasons for failed spatially-extended alternans control (including the role of CV, APD, and repolarization dynamics interactions) in real tissue will require more advanced

imaging techniques.

Nonetheless, more complex methods of alternans suppression that rely on multiple electrodes are likely needed if electrode-based alternans therapy is to succeed at the whole-heart level. Though demonstrating reasonable control success at distances up to 2.0 cm represents only a slight increase in effective controllability as compared with previous Purkinje fiber results, an increase in the minimum spacing required would lessen the technical challenges associated with the clinical implementation of multisite control. Studies such as this, which help to illuminate the degree to which single-site control can reduce spatial alternans, will aid in the development of such therapies.

Currently, the predominant ventricular fibrillation therapy consists of applying large voltages across the heart using internally implanted electrical leads [2, 3, 61]. The implantable cardioverter defibrillator (ICD) is the primary delivery mechanism for treatments of this type, and though reasonably effective in the termination of VF [62], repeated use can cause physical damage to the cardiac tissue, which can act as an arrhythmogenic substrate for future VF initiation [63, 64]. Also, psychological factors that are often times associated with ICD use, such as persistent stress and anxiety, are not to be dismissed [65, 66]. Thus, there is a real need to develop improved strategies that can terminate and/or prevent VF.

Given the supporting evidence suggesting that alternans may be a precursor to VF initiation, alternans management warrants further investigation. Because of the relatively straightforward implementation requirements, model-independent alternans control mechanisms like the one used in this study represent a potentially viable

option. Alternans control capability could be added to current ICD modalities, and technologies such as multipole leads or the CorCap cardiac support device [67, 68] could provide a means for the clinical realization of multisite control.

CHAPTER 4

# CONTROL OF ACTION POTENTIAL DURATION ALTERNANS – THE EFFECTS OF NOISE

## 4.1 Outline

In Chapter 3 we presented results from optical mapping experiments, which used voltage-sensitive fluorescent dyes and CCD camera technology to probe the spatial dynamics of alternans and alternans control in ventricular tissue preparations. The issue of noise in the context of alternans control was briefly mentioned, but a rigorous analysis of the topic was not presented. In this chapter, the dynamics of noise and alternans in the context of control are investigated using computer simulations. Specifically, the Shiferaw-Sato-Karma (SSK) cardiac cell model [18] is used to simulate alternans and alternans control under varying degrees of added Gaussian noise both in single-cell and 1-D cable settings. The results obtained suggest that the effect of noise is largely determined by the instability characteristics of the cardiac cell via the slope of the APD restitution curve. These results further highlight the potential challenges of controlling alternans, especially in experimental settings where sampling noise is difficult to eliminate.

## 4.2 Introduction

Pioneered by researchers in the 1970's [69], optical mapping techniques have proven particularly useful in elucidating important dynamical features of cardiac

electrophysiology with high spatiotemporal resolution through the use of fluorescent probes designed to measure transmembrane potential and intracellular free calcium [70]. Transmembrane potential recordings are most commonly obtained using membrane-bound dyes that exhibit distinct fluorescence characteristics in response to excitation by an exogenous light source [71]. The key feature enabling the use of membrane-bound fluorescent probes is the voltage-dependent changes in fluorescence that naturally occur. So-called "fast" voltage-sensitive dyes can track changes in voltage on the time scale of microseconds [72]. (It should be noted that voltage-sensitive dyes do not provide an absolute measurement of transmembrane potential but merely track the changes in membrane potential with high temporal fidelity [57]. The precise mechanism by which changes in transmembrane voltage result in proportional changes in fluorescence remains unknown [57].)

Of the many different types of compounds that are known to exhibit voltage-dependent fluorescence characteristics, styryl dyes represent the most popular for cardiovascular use [57]. Of the styryl family of dyes, di-4-ANEPPS has been widely used by experimenters studying cardiac function. The spectroscopic properties of di-4-ANEPPS (and other related dyes) have been shown to linearly change with membrane potential changes in the normal physiological range of transmembrane voltages [57].

Reductions in phototoxicity and increases in the sensitivity to transmembrane potential changes have made fluorescent dyes ever more useful in cardiovascular research [57]. However, despite all of the benefits of using fluorescent dyes like di-4-ANEPPS for cardiac electrophysiological experiments, the low signal-to-noise (SNR) characteristics often times associated can be a significant challenge to overcome.

Much of the signal-to-noise characteristics are determined by the imaging technology chosen to detect the fluorescence. For cardiac imaging, the two most commonly used detector technologies are CCD cameras and photodiode array (PDA) detectors [58]. Whereas PDA detectors operate by continuously generating current in response to light flux, the mechanism of CCD cameras is analogous to the conventional photographic process: each frame is the result of integrated light collection over a discrete time interval. Comparing CCD and PDA technology, PDA detectors posses better SNR characteristics; however, a typical CCD camera possesses many more recording elements, and for that reason CCD cameras often times provide the best option for taking high-resolution optical movies of cardiac activity over relatively large regions of tissue [70].

The fundamental CCD detection element is a pixel, and at each pixel charge is generated as light is collected over a given time interval. The accumulated charge is translated from the CCD chip to a voltage read-out on a pixel-by-pixel basis. A "frame" is comprised of the resulting voltages that were simultaneously obtained from each pixel. To initiate a new frame, the charge for each pixel is zeroed and the process is repeated.

For CCD camera technology, detection sensitivity is predominantly determined by three classes of noise: dark current noise, readout noise, and shot noise [58]. Dark current and readout noise comprise what is referred to as the "floor noise" of the system – noise that is independent of the signal intensity. Shot noise, on the other hand, reflects the random variations in the signal due to the quantum nature of light and scales with the square root of the signal intensity. Shot noise is a fundamental trait of light, and can be reduced only by collecting more photons. (Technically, shot

noise exhibits a Poisson distribution, and so for large numbers it can be modeled as a normal distribution).

The goal of this work is to probe the relationship between noise and alternans in the context of single-site control. Because we want to provide insight that could be useful in future optical mapping experiments, this study aimed to mimic the experimental settings of the preceding chapter. The imaging hardware used in Chapter 3 consisted of a line scan CCD camera, a custom-developed tandem-lens assembly, and an LED-based light source. Performance measurements for the system showed that the predominant noise in the operational range of the experiments (i.e., sampling rate and dynamic range) was shot noise, with dark noise and readout noise contributing to <20% of the total noise level [41]. Therefore, in simulating optical mapping noise, a normal distribution was used to capture the majority effect of shot noise in the system.

## 4.3 Methodology

### *4.3.1 Simulations*

Single-cell and 1-D cable simulations were performed using the SSK cell model [18] under the default alternans parameter regime ($u = 9.0$, $\tau_f = 30.0$) and voltage-driven alternans parameter regime ($u = 9.0$, $\tau_f = 30.0$) (see *Chapter 2* for parameter explanations). Implementation occurred in custom C code using the following equations for single cell and 1-D cable representations, respectively:

$$\frac{\partial V(t)}{\partial t} = -\frac{I_{ion} + I_{stim}}{C_m} \quad \textbf{(1)}$$

$$\frac{\partial V(x,t)}{\partial t} = D\frac{\partial^2 V(x,t)}{\partial x^2} - \frac{I_{ion} + I_{stim}}{C_m} \quad \textbf{(2)}$$

where $V$ is the membrane potential, $t$ is the time, $I_{ion}$ is the sum of the transmembrane ionic currents (Hodgkin and Huxley formulations, Ref. [46]), $I_{stim}$ is the externally applied stimulus current (for this model we used 150 μA/cm$^2$ square-wave pulses, 1 ms duration), and $C_m$ is the membrane capacitance (1 μF/cm2 for this model). Numerical integration was done using the forward-Euler scheme, utilizing operator splitting and adaptive time stepping [47] (0.001 ms ≤ dt ≤ 0.025) techniques to minimize computational time. A diffusion constant of 0.001 cm$^2$/ms (integrated with a spatial step size of 0.01 cm) was used. The γ term in the model was set at 0.2, which promoted positive voltage-calcium coupling [18].

The effect of noise was simulated by first generating a pseudorandom number derived from a Gaussian distribution with mean 0 and a predetermined standard deviation. (The Box-Muller random number method was used to generate the noise values). In the context of control, noise affects its functionality by contaminating the process of APD measurements, which is performed using simple threshold crossings. During each time step, a random number was added to the voltage value normally computed by the gating functions, which resulted in a *noise-added* voltage value. In order to simulate the effect of imaging noise, the noise-added voltage value was used only to determine the voltage "observed" by the APD threshold algorithm (noise-free voltage values were used to calculate subsequent state parameters). In order to deal with multiple threshold crossings over a brief period of time as a result of the added noise, a "hysteresis" condition was implemented which effectively set the minimum

APD and DI at 50 ms and 20 ms, respectively (i.e., negative threshold crossings were only identified as the end of an APD if 50 ms had lapsed since the beginning of the APD, and positive threshold crossings were only identified as the end of a DI if at least 20 ms had lapsed since the end of the last action potential).

Pacing occurred at a range of cycle lengths sufficiently fast so as to induce steady-state alternans. At each BCL, 1000 stimuli of static pacing were followed by 1000 stimuli of control-perturbed pacing for single-cell simulations, and 600 of each pacing type were given during the 1-D cable simulations. APD values were calculated at each spatial location using V = -60 ms as the threshold. The alternans control algorithm was implemented according to the following equations:

$$T_n = \begin{cases} T^* + \Delta T_n & \text{if } \Delta T_n < 0, \\ T^* & \text{if } \Delta T_n \geq 0, \end{cases} \quad \textbf{(3)}$$

where

$$\Delta T_n = (\lambda/2)(APD_n - APD_{n-1}), \quad \textbf{(4)}$$

($\Delta T$ – cycle length interval adjustment; $T_n$ – resulting control-perturbed cycle length), $T^*$ is the target BCL (i.e., cycle length applied when control is turned off), $\lambda$ is the feedback gain, and $n$ is the beat number. The feedback gain was chosen to be 1.6.

### *4.3.2 Equations*

*Alternans Magnitude Calculation*

The APD alternans magnitude for a given series of action potentials was calculated according to the following:

Given a sequence of $n$ positive real APD values, $A$:
$A = (A_1, A_2, \ ..., \ A_n)$,
alternans magnitude, $A_M$, is defined as:

$$A_M = \left( \sum_{i=1}^{n-1} \left| A_{i+1} - A_i \right| \right) / (n-1) \quad \textbf{(5)}$$

In the case of control-on pacing, $A_M$ is referred to as *residual alternans* within this chapter.

In order to obtain results from steady-state behavior, $A_M$ and $A_{M,S}$ (spatially averaged alternans) were calculated from the last 50 action potentials during both control-off and control-on conditions. Also, an integration time of 1 ms was simulated in order to more closely match optical mapping experiment settings.

### *4.3.3 Signal-to-noise calculation*

In general, SNR can be quantified as the signal amplitude maximum minus the signal amplitude minimum, divided by the standard deviation of the added noise. For simplicity and consistency, all SNR values were calculated using 100 ms for the numerator (estimated from single cell simulations under default parameter settings @ BCL = 500 ms).

## 4.4 Results

### *4.4.1 Single Cell*

Example action potentials and APD values derived from single-cell simulations of the default alternans parameter settings are shown in Fig. 4.1. Pacing at BCL = 170 ms in the absence of noise produced action potentials exhibiting constant-

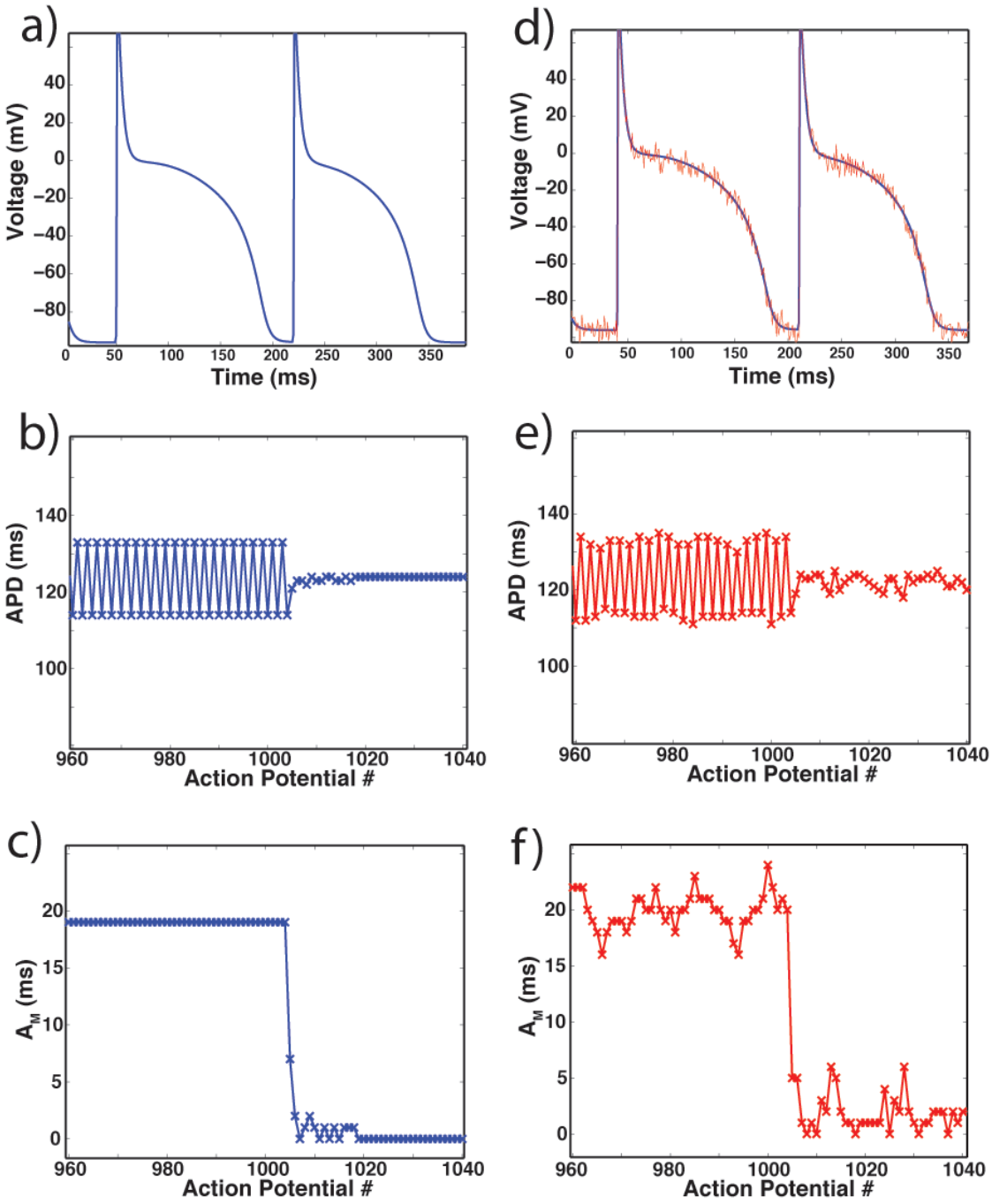


**Figure 4.1 Effect of noise on action potential morphology and beat-to-beat alternans.** Example action potentials and alternans behavior during static and control-perturbed pacing (BCL = 170 ms). (a) Successive noise-free action potentials plotted as a function of time demonstrating alternating behavior. (b-c) Beat-to-beat APD measurements (b) and $A_M$ measurements (c) during the transition from static pacing to control-perturbed pacing (control is turned on at action potential # 1000). (d) Noise-added action potentials used for APD measurements (red) and underlying noise-free action potentials (blue) demonstrating alternans behavior. (e-f) Beat-to-beat APD measurements (e) and $A_M$ measurements (f) derived from the noise-added voltage values during the transition from static pacing to control-perturbed pacing.

amplitude alternans during control-off conditions ($A_M \approx 19$ ms) and the elimination of alternans during control-on conditions (Fig. 4.1 a-c). Alternans of the same average amplitude is noticeable with the addition of noise (std = 4; SNR = 25) during static pacing, however, $A_M$ calculations tend to fluctuate on a beat-to-beat basis (Fig. 4.1 f). Furthermore, the ability of control to eliminate alternans is compromised with the addition of noise as reflected by the $A_M$ measurements (alternans residual) made during the application of control (Fig. 4.1 F).

Fig 4.2 displays the steady-state $A_M$ calculations derived from static pacing (top half) and control-perturbed pacing (bottom half) for different levels of noise and different BCL values under default alternans parameter settings. Not surprisingly, during static pacing the calculated alternans magnitude increases as BCL decreases regardless of the noise level. Furthermore, for each BCL, $A_M$ calculations remain constant within the range of noise levels simulated. During the application of control, alternans residual is observed to be linearly dependent on the amount of noise added to the system (breakdown in linearity occurs at noise std > 9). Conversely, the ability of the control algorithm to eliminate alternans at a particular noise level is largely independent of the BCL (except for noise std > 9).

Fig 4.3 displays the steady-state $A_M$ calculations derived from voltage-driven alternans parameter settings. Like in the default simulations, during static pacing the level of alternans increases as a function of decreasing BCL. Under control-perturbed pacing, however, differences in the steepness of the linear dependence between residual alternans and noise magnitude are apparent – shorter BCLs are associated with a steeper dependence of residual alternans on noise.

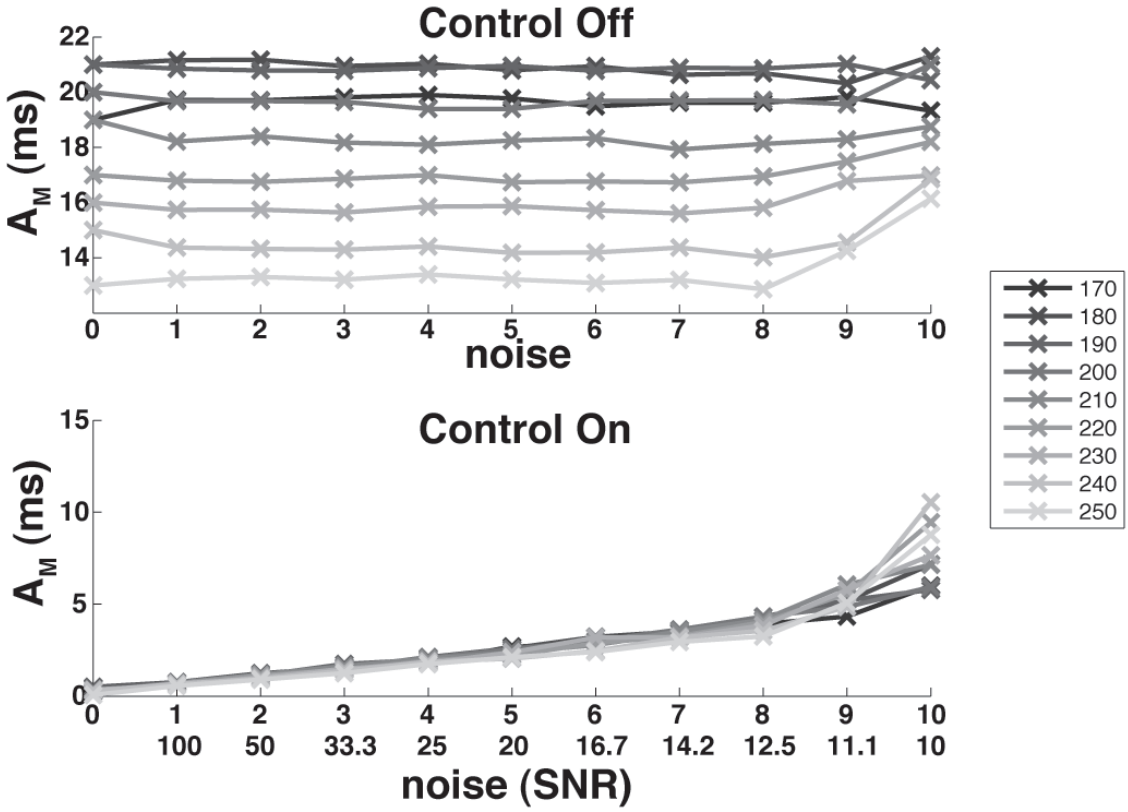


**Figure 4.2 Steady state $A_M$ calculations during static and control-perturbed pacing for different noise and BCL combinations during default alternans.** Top half – control-off $A_M$ results from single-cell simulations at a range of BCLs (170-250 ms) and noise std levels (0-10). Bottom-half – control-on $A_M$ results from single-cell simulations at a range of BCLs (170-250 ms) and noise std levels (0-10). SNR x-axis values calculated according to the methods described in *Sec. 4.3.4*

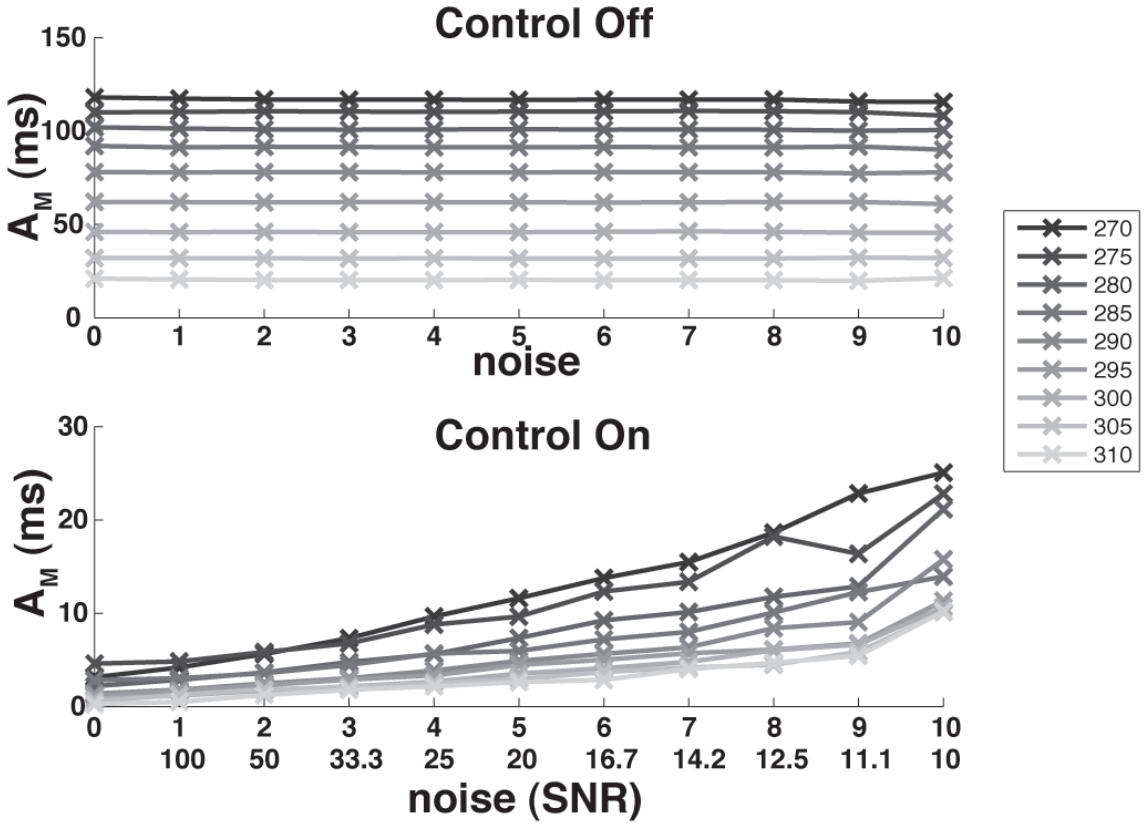


**Figure 4.3 Steady state $A_M$ calculations during static and control-perturbed pacing for different noise and BCL combinations during voltage driven alternans.** Top half – control-off $A_M$ results from single-cell simulations at a range of BCLs (270-310 ms) and noise std levels (0-10). Bottom-half – control-on $A_M$ results from single-cell simulations at a range of BCLs (270-310 ms) and noise std levels (0-10). SNR x-axis values calculated according to the methods described in *Sec. 4.3.4*

### *4.4.2 1-D Cable*

Fig. 4.4 displays the 1-D cable alternans results derived from default parameter simulations with noise std = 0. Steady-state $A_M$ calculations are shown for each computational cell as a function of space. For this and all 1-D simulations of control and noise a cable length of 3 cm was used. During static pacing, concordant alternans is observed with slight attenuation as a function of distance for all BCLs (similar to the results shown in Table 2.1), and during the application of control, $A_M$ at the proximal location is <10 ms at all BCLs. However, control fails spatially in each by an amount that increases as a function of decreasing BCL. In order to investigate the effects of noise on spatial controllability, 1-D simulations were performed at varying noise levels and the resulting alternans spatial profiles were compared to the baseline conditions (i.e., noise std = 0).

Table 4.1 includes the spatially averaged control-on $A_M$ results ($A_{M,S}$) derived from 1-D simulations of varying amounts of noise under default parameter settings. Spatial averages of steady-state $A_M$ values were computed over subregions of L = 0.5 cm, resulting in six separate spatial averages for each simulation. Observing the control-on results for noise std = 0, comparing across the eight different BCL values simulated (4.1.1-4.1.8) reflects the spatial profiles of Fig. 4.4. In each case, control was able to eliminate alternans at the proximal end (0-0.5 cm; $A_{M,S}$ < 10 ms), but fails as a function of distance. When comparing $A_{M,S}$ across the different levels of noise on a BCL-by-BCL basis, the differences in results are minimal. This suggests that in this particular case noise has a limited effect on the spatial extent of single site alternans control. Tables 4.1.9-4.1.16 highlight this result by presenting the absolute differences in $A_{M,S}$ relative to the noise std = 0 case for each BCL. In the majority of the cases, relative to the baseline setting $A_{M,S}$ difference <5 ms.

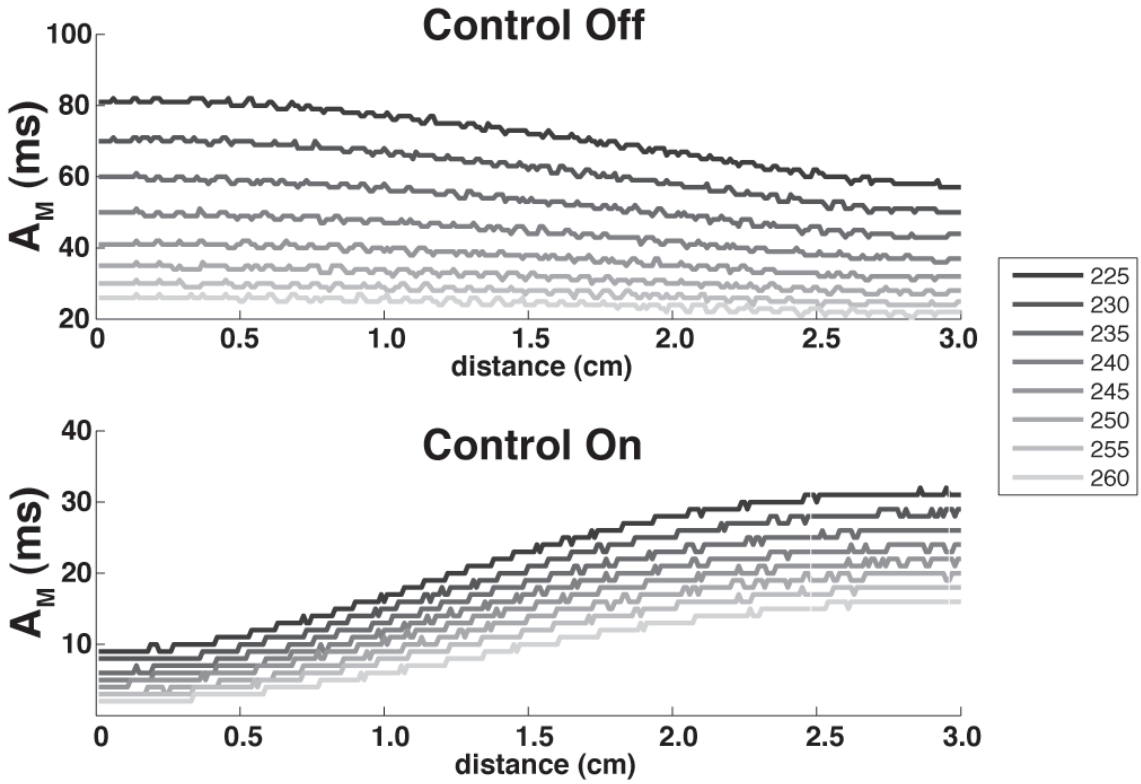


**Figure 4.4 1-D cable steady-state $A_M$ calculations during static and control-perturbed pacing under default parameter settings for different BCL values without the addition of noise.** Top half – point-by-point control-off $A_M$ results (L = 3.0 cm) from cable simulations at a range of BCLs (225-260 ms). Bottom half – point-by-point control-off $A_M$ results (L = 3.0 cm) from cable simulations at a range of BCLs (225-260 ms).

| Color Bar | |
|---|---|
| (0-10) | |
| (10-20) | |
| (20-30) | |
| (30-40) | |
| (40-50) | |
| (50-60) | |
| (60-70) | |
| (70-80) | |
| (80+) | |

| Color Bar | |
|---|---|
| (0-5) | |
| (5-10) | |
| (10-15) | |
| (15-20) | |
| (20-25) | |
| (25-30) | |
| (30-35) | |
| (35-40) | |
| (40+) | |

**BCL = 225 ms**

**4.1.1**

| | $A_{M,S}$ | | | | | |
|---|---|---|---|---|---|---|
| noise | 0-0.5 | 0.5-1.0 | 1.0-1.5 | 1.5-2.0 | 2.9-2.5 | 2.5-3.0 |
| 0 | 9.72 | 13.84 | 20.02 | 25.76 | 29.48 | 31.04 |
| 2 | 9.64 | 13.78 | 20.08 | 25.94 | 29.90 | 31.52 |
| 4 | 9.22 | 13.14 | 19.04 | 24.88 | 28.64 | 30.26 |
| 6 | 9.56 | 13.40 | 19.90 | 25.80 | 29.66 | 31.22 |
| 8 | 13.04 | 15.02 | 19.94 | 24.92 | 28.12 | 29.58 |
| 10 | 19.06 | 19.56 | 20.24 | 21.50 | 22.98 | 23.60 |

**4.1.9**

| | $A_{M,S}$ | | | | | |
|---|---|---|---|---|---|---|
| noise | 0-0.5 | 0.5-1.0 | 1.0-1.5 | 1.5-2.0 | 2.9-2.5 | 2.5-3.0 |
| 0 | 0 | 0 | 0 | 0 | 0 | 0 |
| 2 | 0.08 | 0.06 | 0.06 | 0.18 | 0.42 | 0.48 |
| 4 | 0.50 | 0.70 | 0.98 | 0.88 | 0.84 | 0.78 |
| 6 | 0.16 | 0.44 | 0.12 | 0.04 | 0.18 | 0.18 |
| 8 | 3.32 | 1.18 | 0.08 | 0.84 | 1.36 | 1.46 |
| 10 | 9.34 | 5.72 | 0.22 | 4.26 | 6.50 | 7.44 |

**BCL = 230 ms**

**4.1.2**

| | $A_{M,S}$ | | | | | |
|---|---|---|---|---|---|---|
| noise | 0-0.5 | 0.5-1.0 | 1.0-1.5 | 1.5-2.0 | 2.9-2.5 | 2.5-3.0 |
| 0 | 8.30 | 12.12 | 17.84 | 23.38 | 26.88 | 28.30 |
| 2 | 8.68 | 12.46 | 18.20 | 23.46 | 26.80 | 28.34 |
| 4 | 8.06 | 12.08 | 17.98 | 23.40 | 26.98 | 28.48 |
| 6 | 8.74 | 12.50 | 17.72 | 22.90 | 26.08 | 27.50 |
| 8 | 7.56 | 10.64 | 16.56 | 22.58 | 26.88 | 28.46 |
| 10 | 12.90 | 14.08 | 17.20 | 20.18 | 22.96 | 23.16 |

**4.1.10**

| | $A_{M,S}$ | | | | | |
|---|---|---|---|---|---|---|
| noise | 0-0.5 | 0.5-1.0 | 1.0-1.5 | 1.5-2.0 | 2.9-2.5 | 2.5-3.0 |
| 0 | 0 | 0 | 0 | 0 | 0 | 0 |
| 2 | 0.38 | 0.34 | 0.36 | 0.08 | 0.08 | 0.04 |
| 4 | 0.24 | 0.04 | 0.14 | 0.02 | 0.10 | 0.18 |
| 6 | 0.44 | 0.38 | 0.12 | 0.48 | 0.80 | 0.80 |
| 8 | 0.74 | 1.48 | 1.28 | 0.80 | 0.00 | 0.16 |
| 10 | 4.60 | 1.96 | 0.64 | 3.20 | 3.92 | 5.14 |

**BCL = 235 ms**

**4.1.3**

| | $A_{M,S}$ | | | | | |
|---|---|---|---|---|---|---|
| noise | 0-0.5 | 0.5-1.0 | 1.0-1.5 | 1.5-2.0 | 2.9-2.5 | 2.5-3.0 |
| 0 | 6.82 | 10.58 | 16.06 | 21.10 | 24.32 | 25.84 |
| 2 | 7.00 | 10.62 | 16.16 | 21.08 | 24.30 | 25.88 |
| 4 | 6.48 | 10.18 | 15.58 | 20.76 | 24.20 | 25.70 |
| 6 | 7.70 | 11.24 | 16.38 | 21.16 | 24.08 | 25.44 |
| 8 | 7.22 | 9.82 | 14.62 | 20.02 | 23.20 | 24.54 |
| 10 | 25.56 | 27.00 | 27.50 | 29.56 | 30.90 | 31.24 |

**4.1.11**

| | $A_{M,S}$ | | | | | |
|---|---|---|---|---|---|---|
| noise | 0-0.5 | 0.5-1.0 | 1.0-1.5 | 1.5-2.0 | 2.9-2.5 | 2.5-3.0 |
| 0 | 0 | 0 | 0 | 0 | 0 | 0 |
| 2 | 0.18 | 0.04 | 0.10 | 0.02 | 0.02 | 0.04 |
| 4 | 0.34 | 0.40 | 0.48 | 0.34 | 0.12 | 0.14 |
| 6 | 0.88 | 0.66 | 0.32 | 0.06 | 0.24 | 0.40 |
| 8 | 0.40 | 0.76 | 1.44 | 1.08 | 1.12 | 1.30 |
| 10 | 18.74 | 16.42 | 11.44 | 8.46 | 6.58 | 5.40 |

**BCL = 240 ms**

**4.1.4**

| | $A_{M,S}$ | | | | | |
|---|---|---|---|---|---|---|
| noise | 0-0.5 | 0.5-1.0 | 1.0-1.5 | 1.5-2.0 | 2.9-2.5 | 2.5-3.0 |
| 0 | 5.80 | 9.20 | 14.42 | 19.14 | 22.12 | 23.46 |
| 2 | 5.56 | 8.92 | 13.96 | 18.80 | 21.80 | 23.20 |
| 4 | 5.92 | 9.20 | 14.40 | 18.80 | 22.06 | 23.22 |
| 6 | 5.80 | 9.04 | 14.12 | 19.10 | 22.24 | 23.34 |
| 8 | 11.28 | 12.74 | 16.56 | 20.52 | 23.36 | 24.36 |
| 10 | 10.64 | 12.02 | 15.50 | 20.34 | 23.04 | 24.98 |

**4.1.12**

| | $A_{M,S}$ | | | | | |
|---|---|---|---|---|---|---|
| noise | 0-0.5 | 0.5-1.0 | 1.0-1.5 | 1.5-2.0 | 2.9-2.5 | 2.5-3.0 |
| 0 | 0 | 0 | 0 | 0 | 0 | 0 |
| 2 | 0.24 | 0.28 | 0.46 | 0.34 | 0.32 | 0.26 |
| 4 | 0.12 | 0.00 | 0.02 | 0.34 | 0.06 | 0.24 |
| 6 | 0.00 | 0.16 | 0.30 | 0.04 | 0.12 | 0.12 |
| 8 | 5.48 | 3.54 | 2.14 | 1.38 | 1.24 | 0.90 |
| 10 | 4.84 | 2.82 | 1.08 | 1.20 | 0.92 | 1.52 |

**BCL = 245 ms**

**4.1.5**

| | $A_{M,S}$ | | | | | |
|---|---|---|---|---|---|---|
| noise | 0-0.5 | 0.5-1.0 | 1.0-1.5 | 1.5-2.0 | 2.9-2.5 | 2.5-3.0 |
| 0 | 5.04 | 8.20 | 12.98 | 17.42 | 20.20 | 21.50 |
| 2 | 4.82 | 8.10 | 12.82 | 17.26 | 20.22 | 21.58 |
| 4 | 5.22 | 7.96 | 12.30 | 16.50 | 19.50 | 20.66 |
| 6 | 5.84 | 8.58 | 13.00 | 17.22 | 20.04 | 21.06 |
| 8 | 5.68 | 7.62 | 11.94 | 16.44 | 19.66 | 21.24 |
| 10 | 8.80 | 8.42 | 10.32 | 12.52 | 13.76 | 14.70 |

**4.1.13**

| | $A_{M,S}$ | | | | | |
|---|---|---|---|---|---|---|
| noise | 0-0.5 | 0.5-1.0 | 1.0-1.5 | 1.5-2.0 | 2.9-2.5 | 2.5-3.0 |
| 0 | 0 | 0 | 0 | 0 | 0 | 0 |
| 2 | 0.22 | 0.10 | 0.16 | 0.16 | 0.02 | 0.08 |
| 4 | 0.18 | 0.24 | 0.68 | 0.92 | 0.70 | 0.84 |
| 6 | 0.80 | 0.38 | 0.02 | 0.20 | 0.16 | 0.44 |
| 8 | 0.64 | 0.58 | 1.04 | 0.98 | 0.54 | 0.26 |
| 10 | 3.76 | 0.22 | 2.66 | 4.90 | 6.44 | 6.80 |

**BCL = 250 ms**

**4.1.6**

| | $A_{M,S}$ | | | | | |
|---|---|---|---|---|---|---|
| noise | 0-0.5 | 0.5-1.0 | 1.0-1.5 | 1.5-2.0 | 2.9-2.5 | 2.5-3.0 |
| 0 | 3.78 | 6.78 | 11.32 | 15.62 | 18.42 | 19.76 |
| 2 | 3.38 | 6.46 | 11.12 | 15.50 | 18.40 | 19.88 |
| 4 | 3.60 | 6.26 | 10.84 | 15.16 | 18.10 | 19.62 |
| 6 | 4.76 | 7.26 | 11.74 | 15.90 | 18.40 | 19.56 |
| 8 | 6.88 | 8.42 | 11.70 | 14.92 | 17.50 | 18.58 |
| 10 | 11.10 | 10.64 | 12.76 | 14.82 | 16.76 | 17.48 |

**4.1.14**

| | $A_{M,S}$ | | | | | |
|---|---|---|---|---|---|---|
| noise | 0-0.5 | 0.5-1.0 | 1.0-1.5 | 1.5-2.0 | 2.9-2.5 | 2.5-3.0 |
| 0 | 0 | 0 | 0 | 0 | 0 | 0 |
| 2 | 0.40 | 0.32 | 0.20 | 0.12 | 0.02 | 0.12 |
| 4 | 0.18 | 0.52 | 0.48 | 0.46 | 0.32 | 0.14 |
| 6 | 0.98 | 0.48 | 0.42 | 0.28 | 0.02 | 0.20 |
| 8 | 3.10 | 1.64 | 0.38 | 0.70 | 0.92 | 1.18 |
| 10 | 7.32 | 3.86 | 1.44 | 0.80 | 1.66 | 2.28 |

**BCL = 255 ms**

**4.1.7**

| | $A_{M,S}$ | | | | | |
|---|---|---|---|---|---|---|
| noise | 0-0.5 | 0.5-1.0 | 1.0-1.5 | 1.5-2.0 | 2.9-2.5 | 2.5-3.0 |
| 0 | 3.34 | 5.84 | 9.80 | 13.68 | 16.48 | 17.88 |
| 2 | 3.38 | 5.72 | 9.74 | 13.66 | 16.46 | 17.82 |
| 4 | 3.52 | 5.86 | 10.10 | 14.02 | 16.80 | 18.20 |
| 6 | 3.12 | 4.64 | 8.56 | 12.86 | 16.04 | 17.42 |
| 8 | 5.86 | 7.64 | 10.70 | 14.16 | 16.20 | 17.30 |
| 10 | 10.16 | 10.88 | 11.68 | 14.50 | 16.86 | 17.74 |

**4.1.15**

| | $A_{M,S}$ | | | | | |
|---|---|---|---|---|---|---|
| noise | 0-0.5 | 0.5-1.0 | 1.0-1.5 | 1.5-2.0 | 2.9-2.5 | 2.5-3.0 |
| 0 | 0 | 0 | 0 | 0 | 0 | 0 |
| 2 | 0.04 | 0.12 | 0.06 | 0.02 | 0.02 | 0.06 |
| 4 | 0.18 | 0.02 | 0.30 | 0.34 | 0.32 | 0.32 |
| 6 | 0.22 | 1.20 | 1.24 | 0.82 | 0.44 | 0.46 |
| 8 | 2.52 | 1.80 | 0.90 | 0.48 | 0.28 | 0.58 |
| 10 | 6.82 | 5.04 | 1.88 | 0.82 | 0.38 | 0.14 |

**BCL = 260 ms**

**4.1.8**

| | $A_{M,S}$ | | | | | |
|---|---|---|---|---|---|---|
| noise | 0-0.5 | 0.5-1.0 | 1.0-1.5 | 1.5-2.0 | 2.9-2.5 | 2.5-3.0 |
| 0 | 2.34 | 4.46 | 7.88 | 11.54 | 14.28 | 15.92 |
| 2 | 2.40 | 4.50 | 7.82 | 11.38 | 14.12 | 15.62 |
| 4 | 3.08 | 4.92 | 8.46 | 11.96 | 14.68 | 16.12 |
| 6 | 3.60 | 4.72 | 7.32 | 10.84 | 13.54 | 15.12 |
| 8 | 5.30 | 6.20 | 8.86 | 12.22 | 14.90 | 16.06 |
| 10 | 12.28 | 11.80 | 12.26 | 14.94 | 17.74 | 18.80 |

**4.1.16**

| | $A_{M,S}$ | | | | | |
|---|---|---|---|---|---|---|
| noise | 0-0.5 | 0.5-1.0 | 1.0-1.5 | 1.5-2.0 | 2.9-2.5 | 2.5-3.0 |
| 0 | 0 | 0 | 0 | 0 | 0 | 0 |
| 2 | 0.06 | 0.04 | 0.06 | 0.16 | 0.16 | 0.30 |
| 4 | 0.74 | 0.46 | 0.58 | 0.42 | 0.40 | 0.20 |
| 6 | 1.26 | 0.26 | 0.56 | 0.70 | 0.74 | 0.80 |
| 8 | 2.96 | 1.74 | 0.98 | 0.68 | 0.62 | 0.14 |
| 10 | 9.94 | 7.34 | 4.38 | 3.40 | 3.46 | 2.88 |

**Table 4.1 Spatially averaged alternans magnitude ($A_{M,S}$) results under default parameter settings for varying amounts of added noise.** 4.1.1-4.1.8 – $A_{M,S}$ values from subregions of L = 3 cm 1-D cable (in increments of 0.5 cm) during control-on. 4.1.9-4.1.16 – absolute $A_{M,S}$ difference relative to noise std = 0 (baseline) for each subregion during control-on.

Fig. 4.5 includes the 1-D cable $A_M$ results derived from voltage-driven alternans parameter simulations with noise std = 0. Similar to Fig. 4.4, during static pacing, concordant alternans is observed with slight attenuation as a function of distance. However in this case, control was able to eliminate spatial alternans at each BCL (similar to the results shown in Table 2.2).

Table 4.2 is the same as Table 4.1 except that the results are derived from the voltage-driven alternans parameter setting. The $A_{M,S}$ results as a function of noise are largely the same for all BCL > 310 ms – only when noise std = 10, is there a large deviation away from the baseline setting. At BCL = 310 ms, however, noticeable differences in $A_{M,S}$ are observed as a function of noise level. Fig. 4.6 shows the 1-D cable $A_M$ results derived from BCL = 310 ms at each of the noise levels simulated. One can see in this figure how spatial controllability is adversely affected with increasing levels of noise in this particular case.

## 4.5 Discussion

Optical mapping techniques that use CCD camera technology have become the method of choice for many cardiac function studies, but low SNR due to various types of noise can be an issue. Depending on the nature of the application, the presence of noise can have a significant effect on the end result. The goal of this chapter was to probe the relationship between noise and alternans in the context of single-site control application. This study was inspired by the results presented in Chapter 3, in which transmembrane voltage data was obtained using CCD camera imaging of fluorescence in canine ventricular preparations. A critical component of the study included a

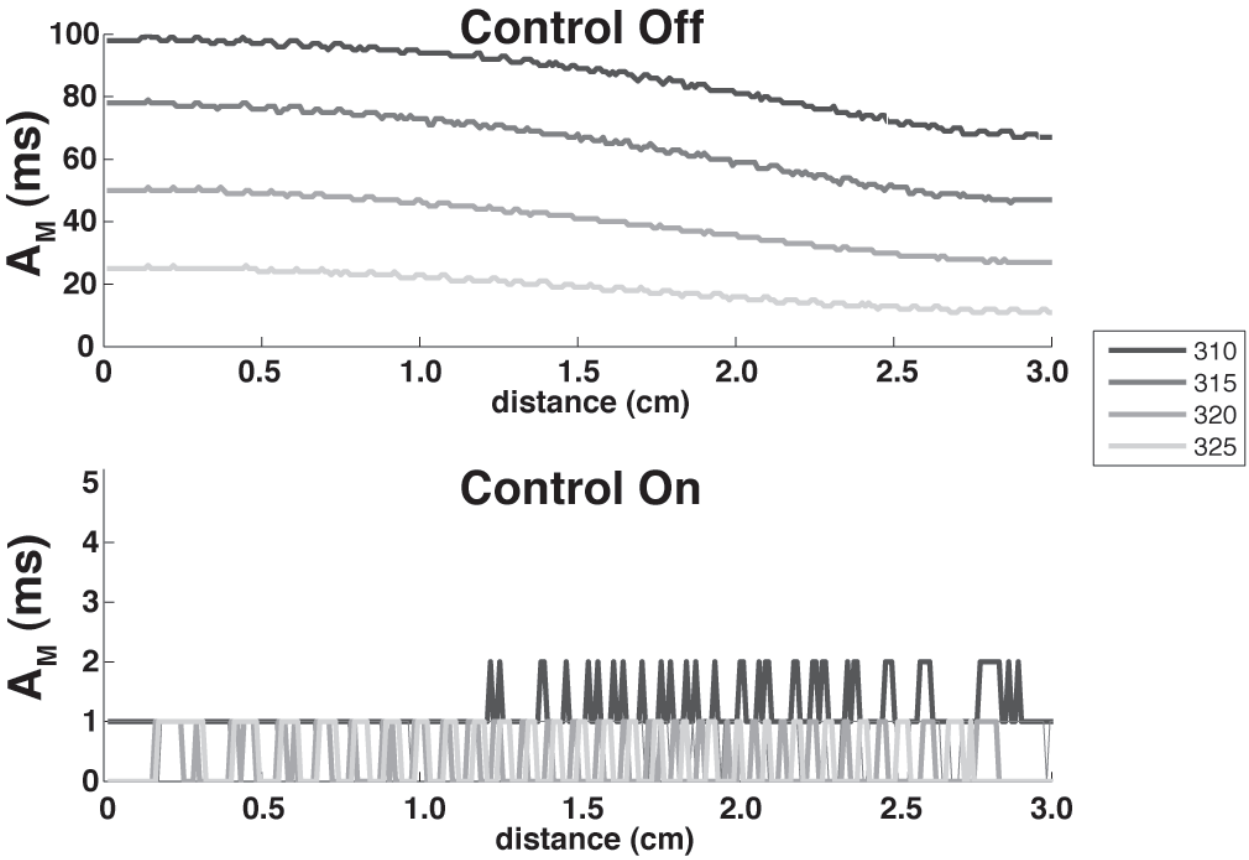


**Figure 4.5 1-D cable steady-state $A_M$ calculations during static and control-perturbed pacing under voltage driven parameter settings for different BCL values without the addition of noise.** Top half – point-by-point control-off $A_M$ results (L = 3.0 cm) from cable simulations at a range of BCLs (310-325 ms). Bottom half – point-by-point control-on $A_M$ results (L = 3.0 cm) from cable simulations at a range of BCLs (310-325 ms).

| Color Bar | |
|---|---|
| (0-10) | |
| (10-20) | |
| (20-30) | |
| (30-40) | |
| (40-50) | |
| (50-60) | |
| (60-70) | |
| (70-80) | |
| (80+) | |

| Color Bar | |
|---|---|
| (0-5) | |
| (5-10) | |
| (10-15) | |
| (15-20) | |
| (20-25) | |
| (25-30) | |
| (30-35) | |
| (35-40) | |
| (40+) | |

**BCL = 310 ms**

**4.2.1**

| | $A_{M,S}$ | | | | | |
|---|---|---|---|---|---|---|
| noise | 0-0.5 | 0.5-1.0 | 1.0-1.5 | 1.5-2.0 | 2.9-2.5 | 2.5-3.0 |
| 0 | 1.00 | 1.00 | 1.10 | 1.20 | 1.34 | 1.26 |
| 2 | 3.94 | 4.42 | 5.32 | 6.12 | 6.70 | 6.86 |
| 4 | 13.74 | 15.52 | 18.04 | 20.28 | 21.02 | 20.88 |
| 6 | 24.90 | 26.82 | 30.02 | 32.80 | 34.34 | 34.26 |
| 8 | 20.74 | 22.70 | 26.24 | 30.36 | 32.30 | 33.48 |
| 10 | 37.28 | 37.62 | 39.10 | 39.04 | 41.26 | 44.94 |

**4.2.5**

| | $A_{M,S}$ | | | | | |
|---|---|---|---|---|---|---|
| noise | 0-0.5 | 0.5-1.0 | 1.0-1.5 | 1.5-2.0 | 2.9-2.5 | 2.5-3.0 |
| 0 | 0 | 0 | 0 | 0 | 0 | 0 |
| 2 | 2.94 | 3.42 | 4.22 | 4.92 | 5.36 | 5.60 |
| 4 | 12.74 | 14.52 | 16.94 | 19.08 | 19.68 | 19.62 |
| 6 | 23.90 | 25.82 | 28.92 | 31.60 | 33.00 | 33.00 |
| 8 | 19.74 | 21.70 | 25.14 | 28.16 | 30.96 | 32.22 |
| 10 | 36.28 | 36.62 | 38.00 | 37.84 | 39.92 | 43.68 |

**BCL = 315 ms**

**4.2.2**

| | $A_{M,S}$ | | | | | |
|---|---|---|---|---|---|---|
| noise | 0-0.5 | 0.5-1.0 | 1.0-1.5 | 1.5-2.0 | 2.9-2.5 | 2.5-3.0 |
| 0 | 0.96 | 0.90 | 1.00 | 0.88 | 0.68 | 0.80 |
| 2 | 2.88 | 2.86 | 2.90 | 2.76 | 2.52 | 2.46 |
| 4 | 4.28 | 4.12 | 4.12 | 4.06 | 3.72 | 3.54 |
| 6 | 6.18 | 6.06 | 6.18 | 6.18 | 6.28 | 6.14 |
| 8 | 10.20 | 10.48 | 11.20 | 12.36 | 12.90 | 13.40 |
| 10 | 25.96 | 27.38 | 29.08 | 31.40 | 33.14 | 34.86 |

**4.2.6**

| | $A_{M,S}$ | | | | | |
|---|---|---|---|---|---|---|
| noise | 0-0.5 | 0.5-1.0 | 1.0-1.5 | 1.5-2.0 | 2.9-2.5 | 2.5-3.0 |
| 0 | 0 | 0 | 0 | 0 | 0 | 0 |
| 2 | 1.92 | 1.96 | 1.90 | 1.88 | 1.84 | 1.66 |
| 4 | 3.32 | 3.22 | 3.12 | 3.18 | 3.04 | 2.74 |
| 6 | 5.22 | 5.16 | 5.18 | 5.30 | 5.60 | 5.34 |
| 8 | 9.24 | 9.58 | 10.20 | 11.48 | 12.22 | 12.60 |
| 10 | 25.00 | 26.48 | 28.08 | 30.52 | 32.46 | 34.06 |

**BCL = 320 ms**

**4.2.3**

| | $A_{M,S}$ | | | | | |
|---|---|---|---|---|---|---|
| noise | 0-0.5 | 0.5-1.0 | 1.0-1.5 | 1.5-2.0 | 2.9-2.5 | 2.5-3.0 |
| 0 | 0.34 | 0.34 | 0.34 | 0.24 | 0.26 | 0.22 |
| 2 | 1.94 | 1.96 | 1.84 | 1.78 | 1.54 | 1.38 |
| 4 | 2.68 | 2.64 | 2.40 | 2.30 | 2.18 | 2.08 |
| 6 | 3.20 | 3.16 | 3.26 | 3.08 | 3.06 | 2.82 |
| 8 | 6.52 | 6.72 | 6.42 | 6.38 | 6.32 | 6.08 |
| 10 | 21.44 | 21.58 | 22.78 | 24.60 | 26.16 | 27.24 |

**4.2.7**

| | $A_{M,S}$ | | | | | |
|---|---|---|---|---|---|---|
| noise | 0-0.5 | 0.5-1.0 | 1.0-1.5 | 1.5-2.0 | 2.9-2.5 | 2.5-3.0 |
| 0 | 0 | 0 | 0 | 0 | 0 | 0 |
| 2 | 1.60 | 1.62 | 1.50 | 1.54 | 1.28 | 1.16 |
| 4 | 2.34 | 2.30 | 2.06 | 2.06 | 1.92 | 1.86 |
| 6 | 2.86 | 2.82 | 2.92 | 2.84 | 2.80 | 2.60 |
| 8 | 6.18 | 6.38 | 6.08 | 6.14 | 6.06 | 5.86 |
| 10 | 21.10 | 21.24 | 22.44 | 24.36 | 25.90 | 27.02 |

**BCL = 325 ms**

**4.2.4**

| | $A_{M,S}$ | | | | | |
|---|---|---|---|---|---|---|
| noise | 0-0.5 | 0.5-1.0 | 1.0-1.5 | 1.5-2.0 | 2.9-2.5 | 2.5-3.0 |
| 0 | 0.46 | 0.48 | 0.42 | 0.34 | 0.24 | 0.20 |
| 2 | 1.62 | 1.52 | 1.28 | 1.24 | 1.08 | 1.04 |
| 4 | 2.20 | 2.16 | 2.02 | 2.08 | 1.98 | 1.90 |
| 6 | 3.02 | 3.02 | 2.80 | 2.84 | 2.68 | 2.66 |
| 8 | 4.98 | 4.90 | 4.68 | 4.30 | 4.26 | 3.96 |
| 10 | 37.50 | 37.12 | 38.76 | 41.28 | 44.16 | 46.32 |

**4.2.8**

| | $A_{M,S}$ | | | | | |
|---|---|---|---|---|---|---|
| noise | 0-0.5 | 0.5-1.0 | 1.0-1.5 | 1.5-2.0 | 2.9-2.5 | 2.5-3.0 |
| 0 | 0 | 0 | 0 | 0 | 0 | 0 |
| 2 | 1.16 | 1.04 | 0.86 | 0.90 | 0.84 | 0.84 |
| 4 | 1.74 | 1.68 | 1.60 | 1.74 | 1.74 | 1.70 |
| 6 | 2.56 | 2.54 | 2.38 | 2.50 | 2.44 | 2.46 |
| 8 | 4.52 | 4.42 | 4.26 | 3.96 | 4.02 | 3.76 |
| 10 | 37.04 | 36.64 | 38.34 | 40.94 | 43.92 | 46.12 |

**Table 4.2 Spatially averaged alternans magnitude ($A_{M,S}$) results under voltage driven parameter settings for varying amounts of added noise.** 4.2.1-4.2.4 – $A_{M,S}$ values from subregions of L = 3 cm 1-D cable (in increments of 0.5 cm) during control-on. 4.2.5-4.2.8 – absolute $A_{M,S}$ difference relative to noise std = 0 (baseline) for each subregion during control-on.

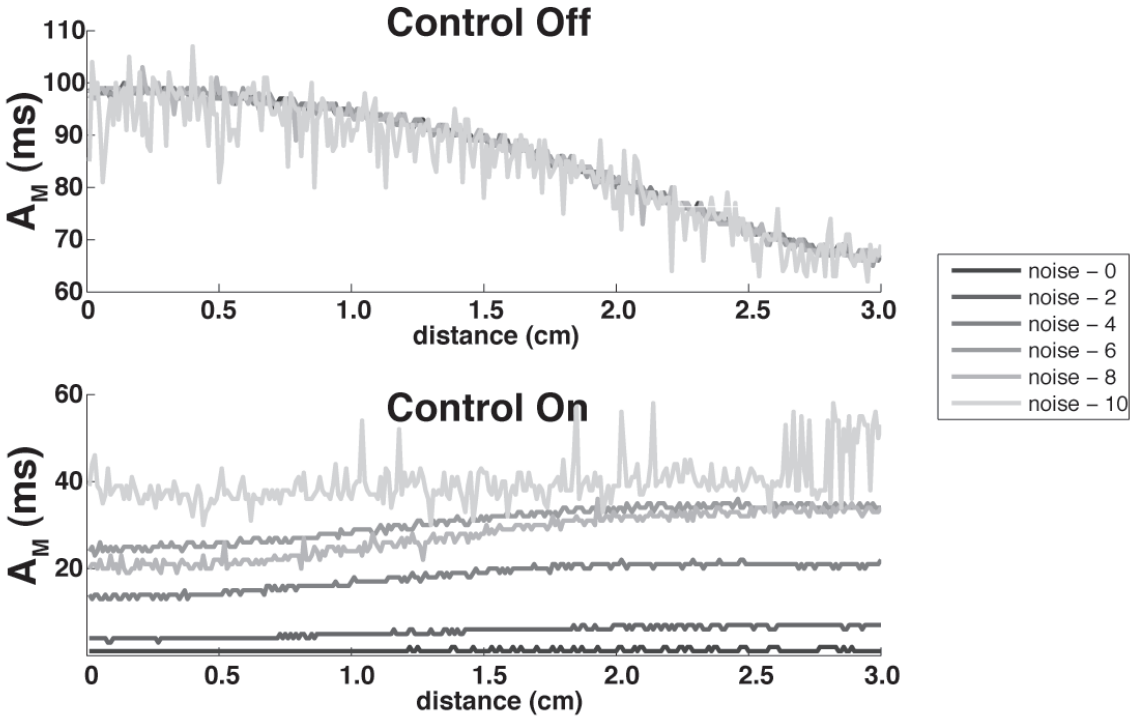


**Figure 4.6 1-D cable steady-state $A_M$ calculations during static and control-perturbed pacing under voltage driven parameter settings for different noise values at BCL = 310 ms.** Top half – point-by-point control-off $A_M$ results (L = 3.0 cm) from cable simulations at a range of noise levels (0-10). Bottom half – point-by-point control-on $A_M$ results (L = 3.0 cm) from cable simulations at a range of noise levels (0-10).

feedback control loop, which used real-time optical recording data to dictate changes in stimulation period. Understanding better how sampling noise affects the controllability of alternans will better aid in future experiments that utilize optical mapping systems.

The effect of noise was investigated using single cell and 1-D cable simulations of the SSK model. Comparing the single-cell results of the default and voltage-driven settings, differences in the dependence of controllability on noise are apparent. For the range of BCLs chosen, the linear relationship between noise and residual alternans was constant for the default parameter settings. Conversely, a steeper relationship between noise and residual alternans was observed during the application of control for the voltage parameter settings, and this steepness increased as a function of decreasing BCL. The reason for this observation most likely has to do with the coupling between noise and alternans. When noise is zero, alternans control works to keep the system in a metastable state with residual alternans $\approx 0$. Increasing levels of noise introduces errors into the APD measurements of Eq. 4, which consequently affects the calculations of Eq. 3. The absolute affect on $T_n$ is determined by the slope ($s$) of the APD restitution curve at the particular BCL. The end result is that the effect of noise on alternans is proportional to $\gamma s$ (where $\gamma$ is the feedback gain). For the default parameter settings, the maximum slope of the APD restitution curve is less than three (Figure 2.2), whereas for the voltage-driven parameter settings the maximum APD restitution slope is more than 2x larger. As a result, the general effect of noise on control is likely to be less under default parameter settings as compared with voltage-driven alternans settings. Furthermore, for each incremental reduction in BCL, one would expect that increasing levels of noise would create

relatively larger errors in APD-derived stimuli adjustments under voltage-driven settings because of the greater APD restitution slope associated.

The effect of noise in the context of single site control in 1-D cables reflects similar characteristics to the single-cell results. In the default settings case, the effect of noise had little effect on the spatial dynamics of alternans regardless of the BCL chosen. $A_{M,S}$ increased, especially in the distal portions of the cable, as pacing cycle length decreased, but the differences in $A_{M,S}$ calculated for the range of noise values tested were small. In the voltage driven alternans parameter settings case, for BCL > 310 ms, there was little change in the spatial dynamics as a function of BCL or noise level as well. Only when BCL = 310 ms, were there observed differences in the spatial controllability as a function of noise level. For BCL > 310 ms, the effects of noise were not enough to disrupt the control process, and given the large effect that electrical coupling has in voltage driven alternans, control was successful spatially (noise std < 10). The underlying dynamics were such that when BCL = 310 ms, an increase in noise from 0 to 2, or from 2 to 4, were enough to fundamentally alter controllability.

The results of this study demonstrate how the effect of noise can disrupt feedback control functionality. Specifically, the effect of noise in the context of alternans control using optical mapping techniques was investigated. Sample data from the optical mapping experiments of Chapter 3 confirmed the normality (via QQ plot inspection) and the whiteness (via autocorrelation analysis) of the noise. Typical SNR measurements for the optical signal obtained from the control point were ≈5. The extent to which noise affected spatial controllability depends on the underlying

nature of alternans and understanding these dynamics will hopefully inform investigators in the structuring of future experiments.

CHAPTER 5

# CONCLUSION AND FUTURE DIRECTIONS

## 5.1 Research Summary

Cardiac electrical alternans is a rhythm disturbance of the heart whereby beat-to-beat alternations in action potential waveform occur. The presence of alternans has been associated with sudden cardiac death and ventricular fibrillation, and there is increasing evidence suggesting a direct mechanistic link between alternans, unidirectional conduction block, and the onset of debilitating arrhythmias. Feedback control schemes, emanating from the field of nonlinear dynamics, have provided a potential means by which to control alternans, and there have been several successful demonstrations of alternans control in experimental conditions. The research presented in this study represents the first comprehensive attempt to investigate alternans and alternans control in ventricular tissue via *in situ* simulations as well as *in vitro* experiments. In terms of clinical relevance, understanding the nature and dynamics of alternans control within the ventricular tissue medium is paramount if external feedback control mechanisms are to be developed for therapeutic use. Given this fact, we believe that this work provides an important advancement toward the realization of a clinically viable means to prevent and/or terminate VF-inducing alternans.

The simulation-based study of Chapter 2 was inspired by a 2002 paper by Echebarria and Karma [34], in which they presented simulation-derived data and analytical analysis regarding the dynamics of alternans and alternans control in Purkinje fiber tissue. The stated aim of the paper was to determine “the maximum

volume of tissue within which alternans can be suppressed by a single electrode, and over what range of period." Though the results *therein* only included data derived from the Noble model of the Purkinje-cell type, the authors claimed that they had performed the same simulation protocol using several other ionic models, and that for these they obtained "qualitatively similar results." The main result of the paper was an equation that related the maximum cable length (where alternans is suppressed by control), $L_{max}$, to several tissue-specific parameters, one of which that depends on conduction velocity. The predictions of this equation were shown to closely match the results of the Noble model simulations, lending credence to the validity of their analytical results. However, that the authors suggested that the unpublished results of the other ionic models were merely qualitatively similar to that of the Noble model leaves questions unanswered as to the exact nature of controllability within ventricular tissue. Their analysis, while providing important insights into alternans control in general, yields only the $L_{max}$ equation as a possible means to predict the dynamical behavior possibilities of alternans control in ventricular tissue. In this way, the equation suggests that there are cardiac tissue properties which could play an important role in controllability, while at the same time providing what is likely an over simplistic characterization dependent on likely too restrictive of an assumption base.

Of the several known differences between Purkinje fiber and ventricular tissue electrical propagation, conduction velocity is one of the more prominent. Tissue experiments suggest that normal conduction in the ventricles is <100 cm/s [37-39], whereas conduction speeds in Purkinje fibers are ≈200 cm/s [40]. As it turns out, the mathematical relationships embedded in the aforementioned $L_{max}$ equation suggest that as CV decreases, controllability decreases as well. This result, if true, could have

important implications in the development of more advanced electrode-based control techniques. But as it stands, the only way to more fully understand the dynamics of alternans control within the ventricular medium is to investigate its behavior directly, either through the use of ventricular-specific simulations (Chapter 2) and/or through experimental studies in ventricular tissue (Chapter 3).

The results of Chapter 2 were derived from computational simulations, which aimed to probe the dynamics of alternans control amidst varying dynamical-yet-physiological settings of ventricular tissue. In the three parameter regimes studied, it was observed that control dissipated sharply as a function of distance at pacing cycle lengths slightly beyond the onset of alternans, similar to the results of the Echebarria and Karma study. However, in focusing on ventricular tissue dynamics, we were able to investigate the behavioral differences across different types of clinically relevant dynamical settings, and in doing so, we highlighted the potential subtleties of alternans control. We showed that the effect of control on the spatial dynamics of alternans is dependent on the underlying nature of the alternans instability, in ways that the $L_{max}$ equation does not fully reflect. Future simulations are no doubt needed (see next Section), but the results of Chapter 2 provide important insights that help in furthering our understanding of alternans control in cardiac tissue.

The experimental study of Chapter 3 combined the innovations of optical mapping technology with the feedback control paradigm to study the effects of alternans control in real ventricular tissue. The many drawbacks and limitations of the design and implementation were discussed in detail previously (see *Section 3.5*). The results of that study produced two main outcomes, the first of which was in providing suggestive evidence that single-site control could have a substantial minimizing effect

on the magnitude of alternans up to 2 cm from the location of intervention. The second function that our experimental studies accomplished was a demonstration of the unique capabilities that optical mapping techniques can provide investigators studying the electrical dynamics of cardiac tissue. Given the innate difficulty in performing these experiments, large data sample sizes were not attainable, and thus strong statistical inferences were not possible. But with advances in imaging and experimental techniques (coupled with additional simulations which use more physiological ionic models), future studies will undoubtedly progress further in understanding the fundamental characteristics of control in ventricular tissue.

Chapter 4 provided a closer look at the specific effects of sampling noise in the context of alternans control. One important factor that affected the results of the optical mapping tissue experiments was that of sampling noise. Future experiments that hope to build on the work of Chapter 3 will likely have to contend with the presence of noise and its direct and indirect effects on the single-site controllability of alternans. Understanding these limitations, and more important, how these limitations affect the spatial dynamics of alternans, will likely be necessary for successful experimentation. That the effect of noise on control depends on the underlying dynamics of alternans instability, as was shown in the corresponding chapter, will likely be of material importance for future investigators.

## 5.2 Future Directions

The results of Chapter 2 included the global results of computational simulations that modeled single-site alternans control applied to the proximal end of a

1-D cable. These simulations were implemented using the Shiferaw-Sato-Karma ventricular cell model [18] under varying cable lengths and pacing cycle length values. The parameters of the ionic model were set so as to mimic endocardial cell type physiology ($G_{Kr}$:$G_{Ks}$ ≈ 11; [44, 45]) and only structurally homogeneous conditions were modeled. Though specific ionic parameters (*tf* and *u*) were systematically varied to reflect different alternans instability mechanisms, further variations could be made to better reflect the full dynamical terrain possible within clinical situations. Simulations which implement changes to the $G_{Ks}$ and $G_{Kr}$ parameters in ways that reflect other cardiac cell types (i.e., mid-myocardial and epicardial tissue) [44, 45] could provide useful information. (This could be of particular importance in the case of the epicardial medium, as it may become possible to apply externally administered electrical perturbations on the outside of the heart via the CorCap cardiac support device [67, 68] or other related technologies, as mentioned in *Section 3.5*).

Furthermore, in order to move closer to realistic situations, investigation within two and three dimensions will be needed. Additionally, simulations of heterogeneous tissue structures more reflective of the physical and conduction pathway architecture of real cardiac tissue would be a natural next step.

It is likely that single-site control is fundamentally inadequate for controlling alternans across large enough regions of tissue necessary for clinical application. One possible advancement that may be capable of providing the level of spatial control needed would be the implementation of a multi-site control system, whereby multiple strategically placed controllers work cooperatively, perhaps synergistically, in preventing/eliminating alternans. Such a system could be similar to that of previously documented techniques used for the spatiotemporal control of physical systems [73-

75], or one could be developed purely from the principles of control theory. A possible system could be based on the straightforward idea that a given controller work in essentially the same way as described in this work, with a few modifications that factor in action potential conduction velocities. In this way, each individual controller would eliminate alternans at all points locally, but by virtue of having many sites of control, relatively macro spatiotemporal alternations could be suppressed, even amidst settings of heterogeneity. A systematic investigation could reveal the optimal electrode spacing and feedback gain values necessary for adequate control.

In order for multi-site control systems like the one previously discussed to be clinically viable, significant advancements in other technologies would be needed. For one, accurate and consistent measurement of transmembrane electrical activity without the benefit of cell-membrane penetrating microelectrodes – an approach not possible for use in the real heart – is still needed (research into this type of problem has already been addressed [76]). In addition, the technology of the CorCap cardiac support device or others related still needs to be fully developed and approved before the idea of a mesh of electrodes can become reality.

Perhaps the primary goal of external electrode control should be shifted from the minimization of alternans magnitude to the reduction in overall dispersion, given that steep repolarization gradients is the proximal link to the onset of unidirectional block and VF initiation. During alternans, the system is most unstable at the period-1 fixed point, making attempts to control using the standard alternans control approach an uphill battle. In the context of single-cell control, this inherent difficulty is easy to overcome; however, when attempting to control an entire electrically coupled spatially-extended system to the period-1 fixed point, in which all points are exhibiting

alternans, this prospect becomes much more difficult, as was demonstrated in this and other studies. The current form of the alternans control algorithm allows for easy adjustment to the feedback parameter, λ. Feedback is typically chosen such that the complete elimination of alternans at the control point is most likely to occur and it has been shown, both using linear stability analysis and in practice, that local control can be achieved over a relatively wide range of λ values (the feedback values of 1.6 and 2.0, which were used in these studies, are within this range). In accepting the futility of complete spatial control, it may be that a smaller feedback value would allow the system to exist in a much *less* unstable state, in which gradients of repolarization are minimized and arrhythmogenicity greatly reduced. And given the small spatial extent to which single-site control is achieved, sacrificing control efficacy at one point may be a net benefit. This sort of approach may be of particular relevance in the context of multi-site control, given that both alternans and dispersion could be reduced across large regions of tissue in a way that yields a less unstable and therefore more dynamically robust state. Recasting the alternans/dispersion problem in this way would require that control experiments be designed to probe VF initiation propensity and overall arrhythmogenicity properties.

Many of the future directions relating to the optical mapping experiments were discussed previously (*Section 3.5*). Our hope is that future investigators can further the progress made and in doing so create a clearer and more accurate view of what occurs in real hearts under physiological conditions, because ultimately, this is the type of work that will need to be done before significant strides can be made toward developing a clinically viable alternans therapy.

The results of Chapter 4 should provide future investigators with a better understanding about the realities of conducting these types of experiments in real animal hearts. The nature and importance of noise will depend on the context of the experiment, and as such, future investigators may need to conduct sensitivity analyses of their own in a way that is most relevant to their needs.

To conclude, our hope is that the research of this dissertation has succeeded in providing the cardiac electrodynamics community with results and insights that are both relevant and important to the field as a whole, and in doing so, managed to advance the science toward the ultimate goal of greatly diminishing the prevalence and adverse effects of abnormal cardiac electrical rhythms.

## BIBLIOGRAPHY


[1] A. A. Armoundas, G. F. Tomaselli, and H. D. Esperer, "Pathophysiological basis and clinical application of T-wave alternans," *Journal of the American College of Cardiology,* vol. 40, no. 2, pp. 207-17, Jul 17, 2002.

[2] D. T. Connelly, "Implantable cardioverter-defibrillators," *Heart,* vol. 86, no. 2, pp. 221-6, Aug 1, 2001.

[3] J. J. Goldberger, "Treatment and prevention of sudden cardiac death: effect of recent clinical trials," *Arch Intern Med,* vol. 159, no. 12, pp. 1281-7, Jun 28, 1999.

[4] A. Armoundas, M. Osaka, T. Mela *et al*., "T-wave alternans and dispersion of the QT interval as risk stratification markers in patients susceptible to sustained ventricular arrhythmias," *The American Journal of Cardiology,* vol. 82, no. 9, pp. 1127-1129, 1998.

[5] M. Gold, D. Bloomfield, K. Anderson *et al*., "A comparison of T-wave alternans, signal averaged electrocardiography and programmed ventricular stimulation for arrhythmia risk stratification," *Journal of the American College of Cardiology,* vol. 36, no. 7, pp. 2247-2253, 2000.

[6] S. Hohnloser, T. Klingenheben, Y. Li *et al*., "T wave alternans as a predictor of recurrent ventricular tachyarrhythmias in ICD recipients: prospective comparison with conventional risk markers," *Journal of Cardiovascular Electrophysiology,* vol. 9, pp. 1258-1268, 1998.

[7] T. Klingenheben, M. Zabel, R. D'Agostino *et al*., "Predictive value of T-wave alternans for arrhythmic events in patients with congestive heart failure," *The Lancet,* vol. 356, no. 9230, pp. 651-652, 2000.

[8] D. Rosenbaum, L. Jackson, J. Smith *et al*., "Electrical alternans and vulnerability to ventricular arrhythmias," *New England Journal of Medicine,* vol. 330, no. 4, pp. 235, 1994.

[9] M. Chinushi, D. Kozhevnikov, E. B. Caref *et al*., "Mechanism of discordant T wave alternans in the in vivo heart," *Journal of Cardiovascular Electrophysiology,* vol. 14, no. 6, pp. 632-8, Jun 1, 2003.

[10] M. Chinushi, M. Restivo, E. B. Caref *et al*., "Electrophysiological basis of arrhythmogenicity of QT/T alternans in the long-QT syndrome: tridimensional analysis of the kinetics of cardiac repolarization," *Circulation Research,* vol. 83, no. 6, pp. 614-28, Sep 21, 1998.

[11] W. Shimizu, and C. Antzelevitch, "Cellular and ionic basis for T-wave alternans under long-QT conditions," *Circulation,* vol. 99, no. 11, pp. 1499, 1999.

[12] S. M. Narayan, "T-wave alternans and the susceptibility to ventricular arrhythmias," *Journal of the American College of Cardiology,* vol. 47, no. 2, pp. 269-81, Jan 17, 2006.

[13] J. Pastore, S. Girouard, K. Laurita *et al.*, "Mechanism linking T-wave alternans to the genesis of cardiac fibrillation," *Circulation,* vol. 99, no. 10, pp. 1385, 1999.

[14] J. Fox, M. Riccio, F. Hua *et al.*, "Spatiotemporal transition to conduction block in canine ventricle," *Circulation Research,* vol. 90, no. 3, pp. 289, 2002.

[15] J. Pastore, and D. Rosenbaum, "Role of structural barriers in the mechanism of alternans-induced reentry," *Circulation Research,* vol. 87, no. 12, pp. 1157, 2000.

[16] D. Zipes, and J. Jalife, "Cardiac Electrophysiology: From Cell to Bedside."

[17] B. F. HOFFMAN, and E. E. SUCKLING, "Effect of heart rate on cardiac membrane potentials and the unipolar electrogram," *American Journal of Physiology,* vol. 179, no. 1, pp. 123-30, Oct 1, 1954.

[18] Y. Shiferaw, D. Sato, and A. Karma, "Coupled dynamics of voltage and calcium in paced cardiac cells," *Physical Review E,* vol. 71, no. 2, pp. 21903, 2005.

[19] J. I. Goldhaber, L.-H. Xie, T. Duong *et al.*, "Action potential duration restitution and alternans in rabbit ventricular myocytes: the key role of intracellular calcium cycling," *Circulation Research,* vol. 96, no. 4, pp. 459-66, Mar 4, 2005.

[20] E. Chudin, J. Goldhaber, A. Garfinkel *et al.*, "Intracellular Ca(2+) dynamics and the stability of ventricular tachycardia," *Biophysical Journal,* vol. 77, no. 6, pp. 2930-41, Dec 1, 1999.

[21] M. E. Díaz, S. C. O'Neill, and D. A. Eisner, "Sarcoplasmic reticulum calcium content fluctuation is the key to cardiac alternans," *Circulation Research,* vol. 94, no. 5, pp. 650-6, Mar 19, 2004.

[22] Y. Shiferaw, M. A. Watanabe, A. Garfinkel *et al.*, "Model of intracellular calcium cycling in ventricular myocytes," *Biophysical Journal,* vol. 85, no. 6, pp. 3666-86, Dec 1, 2003.

[23] J. Weiss, A. Karma, Y. Shiferaw *et al*., "From pulsus to pulseless: the saga of cardiac alternans," *Circulation Research,* vol. 98, no. 10, pp. 1244, 2006.

[24] Z. Qu, A. Garfinkel, P. S. Chen *et al*., "Mechanisms of discordant alternans and induction of reentry in simulated cardiac tissue," *Circulation,* vol. 102, no. 14, pp. 1664-70, Oct 3, 2000.

[25] E. Ott, C. Grebogi, and J. Yorke, "Controlling chaos," *Physical Review Letters,* vol. 64, no. 11, pp. 1196-1199, 1990.

[26] D. Christini, and J. Collins, "Using chaos control and tracking to suppress a pathological nonchaotic rhythm in a cardiac model," *Physical Review E, Statistical physics, plasmas, fluids, and related interdisciplinary topics,* vol. 53, no. 1, pp. R49-R52, Jan 1, 1996.

[27] D. Gauthier, and J. Socolar, "Comment on "Dynamic Control of Cardiac Alternans"," *Physical Review Letters,* vol. 79, no. 24, pp. 4938-4938, 1997.

[28] K. Hall, D. Christini, M. Tremblay *et al*., "Dynamic control of cardiac alternans," *Physical Review Letters,* vol. 78, no. 23, pp. 4518-4521, 1997.

[29] D. Christini, K. Stein, S. Markowitz *et al*., "Nonlinear-dynamical arrhythmia control in humans," *Proceedings of the National Academy of Sciences,* vol. 98, no. 10, pp. 5827, 2001.

[30] G. Hall, and D. Gauthier, "Experimental control of cardiac muscle alternans," *Physical Review Letters,* vol. 88, no. 19, pp. 198102, 2002.

[31] J. Nolasco, and R. Dahlen, "A graphic method for the study of alternation in cardiac action potentials," *Journal of Applied Physiology,* vol. 25, no. 2, pp. 191-6, 1968.

[32] K. Hall, and D. Christini, "Restricted feedback control of one-dimensional maps," *Physical Review E,* vol. 63, no. 4, pp. 46204, 2001.

[33] S. Gaeta, G. Bub, G. Abbott *et al*., "Dynamical Mechanism for Subcellular Alternans in Cardiac Myocytes," *Circulation Research*, 2009.

[34] B. Echebarria, and A. Karma, "Spatiotemporal control of cardiac alternans," *Chaos: An Interdisciplinary Journal of Nonlinear Science,* vol. 12, pp. 923, 2002.

[35] D. Noble, "A modification of the Hodgkin--Huxley equations applicable to Purkinje fibre action and pace-maker potentials," *Journal of Physiology (Lond),* vol. 160, pp. 317-52, Feb 1, 1962.

[36] D. Christini, M. Riccio, C. Culianu *et al*., "Control of electrical alternans in canine cardiac purkinje fibers," *Physical Review Letters,* vol. 96, no. 10, pp. 104101, 2006.

[37] D. Roberts, L. Hersh, and A. Scher, "Influence of cardiac fiber orientation on wavefront voltage, conduction velocity, and tissue resistivity in the dog," *Circulation Research,* vol. 44, no. 5, pp. 701, 1979.

[38] D. Roberts, and A. Scher, "Effect of tissue anisotropy on extracellular potential fields in canine myocardium in situ," *Circulation Research,* vol. 50, no. 3, pp. 342, 1982.

[39] J. P. Wikswo, T. A. Wisialowski, W. A. Altemeier *et al*., "Virtual cathode effects during stimulation of cardiac muscle. Two-dimensional in vivo experiments," *Circulation Research,* vol. 68, no. 2, pp. 513-30, Feb 1, 1991.

[40] M. L. Pressler, "Membrane properties of the cardiac conduction system: comparative aspects," *Proc Kon Ned Akad v Wetensch,* vol. 93, no. 4, pp. 477-487, Dec 17, 1990.

[41] S. Iravanian, and D. Christini, "Optical mapping system with real-time control capability," *American Journal of Physiology - Heart and Circulatory Physiology,* vol. 293, no. 4, pp. H2605, 2007.

[42] J. Fox, J. McHarg, and R. Gilmour Jr, "Ionic mechanism of electrical alternans," *American Journal of Physiology - Heart and Circulatory Physiology,* vol. 282, no. 2, pp. H516, 2002.

[43] P. Jordan, and D. Christini, "Characterizing the contribution of voltage-and calcium-dependent coupling to action potential stability: implications for repolarization alternans," *American Journal of Physiology - Heart and Circulatory Physiology,* vol. 293, no. 4, pp. H2109, 2007.

[44] P. C. Viswanathan, and Y. Rudy, "Cellular arrhythmogenic effects of congenital and acquired long-QT syndrome in the heterogeneous myocardium," *Circulation,* vol. 101, no. 10, pp. 1192-8, Mar 14, 2000.

[45] P. C. Viswanathan, R. M. Shaw, and Y. Rudy, "Effects of IKr and IKs heterogeneity on action potential duration and its rate dependence: a simulation study," *Circulation,* vol. 99, no. 18, pp. 2466-74, May 11, 1999.

[46] A. L. Hodgkin, and A. F. Huxley, "A quantitative description of membrane current and its application to conduction and excitation in nerve," *Journal of Physiology (Lond),* vol. 117, no. 4, pp. 500-44, Aug 1, 1952.

[47] A. Zhilin Qu Garfinkel, "An advanced algorithm for solving partial differential equation in cardiac conduction," *IEEE Transactions on Biomedical Engineering*, Jan 1, 1999.

[48] H. Hayashi, Y. Shiferaw, D. Sato *et al*., "Dynamic origin of spatially discordant alternans in cardiac tissue," *Biophysical Journal,* vol. 92, no. 2, pp. 448-60, Jan 15, 2007.

[49] M. A. Watanabe, F. H. Fenton, S. J. Evans *et al*., "Mechanisms for discordant alternans," *Journal of Cardiovascular Electrophysiology,* vol. 12, no. 2, pp. 196-206, Feb 1, 2001.

[50] F. X. Witkowski, L. J. Leon, P. A. Penkoske *et al*., "Spatiotemporal evolution of ventricular fibrillation," *Nature,* vol. 392, no. 6671, pp. 78-82, Mar 5, 1998.

[51] A. Karma, "Electrical alternans and spiral wave breakup in cardiac tissue," *Chaos: An Interdisciplinary Journal of Nonlinear Science,* vol. 4, pp. 461, 1994.

[52] V. Fedorov, I. Lozinsky, E. Sosunov *et al*., "Application of blebbistatin as an excitation–contraction uncoupler for electrophysiologic study of rat and rabbit hearts," *Heart Rhythm,* vol. 4, no. 5, pp. 619-626, 2007.

[53] S. H. Strogatz, *Nonlinear Dynamics and Chaos: With Applications to Physics, Biology, Chemistry and Engineering*. Boulder, CO: Westview, 1998, pp. 44

[54] K. Laurita, S. Girouard, and D. Rosenbaum, "Modulation of ventricular repolarization by a premature stimulus: role of epicardial dispersion of repolarization kinetics demonstrated by optical mapping of the intact guinea pig heart," *Circulation Research,* vol. 79, no. 3, pp. 493, 1996.

[55] T. Watanabe, P. M. Rautaharju, and T. F. McDonald, "Ventricular action potentials, ventricular extracellular potentials, and the ECG of guinea pig," *Circulation Research,* vol. 57, no. 3, pp. 362-73, Sep 1, 1985.

[56] D. S. Rosenbaum, D. T. Kaplan, A. Kanai *et al*., "Repolarization inhomogeneities in ventricular myocardium change dynamically with abrupt cycle length shortening," *Circulation,* vol. 84, no. 3, pp. 1333-45, Sep 1, 1991.

[57] I. R. Efimov, V. P. Nikolski, and G. Salama, "Optical imaging of the heart," *Circulation Research,* vol. 95, no. 1, pp. 21-33, Jul 9, 2004.

[58] E. Entcheva, and H. Bien, "Macroscopic optical mapping of excitation in cardiac cell networks with ultra-high spatiotemporal resolution," *Progress in Biophysics and Molecular Biology,* vol. 92, no. 2, pp. 232-257, 2006.

[59] J. M. Smith, E. A. Clancy, C. R. Valeri *et al*., "Electrical alternans and cardiac electrical instability," *Circulation,* vol. 77, no. 1, pp. 110-21, Jan 1, 1988.

[60] J. L. Puglisi, R. A. Bassani, J. W. Bassani *et al*., "Temperature and relative contributions of Ca transport systems in cardiac myocyte relaxation," *American Journal of Physiology,* vol. 270, no. 5 Pt 2, pp. H1772-8, May 1, 1996.

[61] M. Glikson, and P. A. Friedman, "The implantable cardioverter defibrillator," *Lancet,* vol. 357, no. 9262, pp. 1107-17, Apr 7, 2001.

[62] J. Parkes, J. Bryant, and R. Milne, "Implantable cardioverter-defibrillators in arrhythmias: a rapid and systematic review of effectiveness," *Heart,* vol. 87, no. 5, pp. 438-42, May 1, 2002.

[63] C. F. Babbs, W. A. Tacker, J. F. VanVleet *et al*., "Therapeutic indices for transchest defibrillator shocks: effective, damaging, and lethal electrical doses," *American Heart Journal,* vol. 99, no. 6, pp. 734-8, Jun 1, 1980.

[64] G. P. Walcott, C. R. Killingsworth, and R. E. Ideker, "Do clinically relevant transthoracic defibrillation energies cause myocardial damage and dysfunction?," *Resuscitation,* vol. 59, no. 1, pp. 59-70, Oct 1, 2003.

[65] S. B. Dunbar, "Psychosocial issues of patients with implantable cardioverter defibrillators," *American Journal of Critical Care,* vol. 14, no. 4, pp. 294-303, Jul 1, 2005.

[66] P. L. Morris, J. Badger, C. Chmielewski *et al*., "Psychiatric morbidity following implantation of the automatic implantable cardioverter defibrillator," *Psychosomatics,* vol. 32, no. 1, pp. 58-64, Jan 1, 1991.

[67] J. Power, J. Raman, A. Dornom *et al*., "Passive ventricular constraint amends the course of heart failure: a study in an ovine model of dilated cardiomyopathy," *Cardiovascular Research,* vol. 44, no. 3, pp. 549, 1999.

[68] M. Oz, W. Konertz, F. Kleber *et al*., "Global surgical experience with the Acorn cardiac support device," *The Journal of Thoracic and Cardiovascular Surgery,* vol. 126, no. 4, pp. 983-991, 2003.

[69] L. B. Cohen, B. M. Salzberg, H. V. Davila *et al*., "Changes in axon fluorescence during activity: molecular probes of membrane potential," *Journal of Membrane Biology,* vol. 19, no. 1, pp. 1-36, Jan 1, 1974.

[70] W. T. Baxter, J. M. Davidenko, L. M. Loew *et al*., "Technical features of a CCD video camera system to record cardiac fluorescence data," *Annals of Biomedical Engineering,* vol. 25, no. 4, pp. 713-25, Jan 1, 1997.

[71] M. Morad, and G. Salama, "Optical probes of membrane potential in heart muscle," The *Journal of Physiology (Lond),* vol. 292, pp. 267-95, Jul 1, 1979.

[72] V. Lev-Ram, and A. Grinvald, "Ca2+- and K+-dependent communication between central nervous system myelinated axons and oligodendrocytes revealed by voltage-sensitive dyes," *Proceedings of the National Academy of Sciences of the United States of America,* vol. 83, no. 17, pp. 6651-5, Sep 1, 1986.

[73] D. Auerbach, "Controlling extended systems of chaotic elements," *Physical Review Letters,* vol. 72, no. 8, pp. 1184-1187, 1994.

[74] H. Gang, and Q. Zhilin, "Controlling spatiotemporal chaos in coupled map lattice systems," *Physical Review Letters,* vol. 72, no. 1, pp. 68-71, 1994.

[75] R. Grigoriev, M. Cross, and H. Schuster, "Pinning control of spatiotemporal chaos," *Physical Review Letters,* vol. 79, no. 15, pp. 2795-2798, 1997.

[76] D. J. Christini, K. M. Stein, S. C. Hao *et al*., "Endocardial detection of repolarization alternans," *IEEE Transactions on Biomedical Engineering,* vol. 50, no. 7, pp. 855-62, Jul 1, 2003.